

**UCLA**

**UCLA Electronic Theses and Dissertations**

**Title**

Characterizing Debris Disks With Multi-Wavelength High-Contrast Imaging

**Permalink**

<https://escholarship.org/uc/item/55n3q3qv>

**Author**

Hung, Li-Wei

**Publication Date**

2016

Peer reviewed|Thesis/dissertation

UNIVERSITY OF CALIFORNIA  
Los Angeles

**Characterizing Debris Disks With Multi-Wavelength  
High-Contrast Imaging**

A dissertation submitted in partial satisfaction  
of the requirements for the degree  
Doctor of Philosophy in Astronomy

by

**Li-Wei Hung**

2016

© Copyright by

Li-Wei Hung

2016

ABSTRACT OF THE DISSERTATION

# Characterizing Debris Disks With Multi-Wavelength High-Contrast Imaging

by

**Li-Wei Hung**

Doctor of Philosophy in Astronomy

University of California, Los Angeles, 2016

Professor Michael P. Fitzgerald, Chair

Thousands of extrasolar planets (exoplanets) have been discovered so far, indicating the ubiquity of planetary systems in our galaxy. These exoplanets have an enormous range of characteristics. While the formation mechanism for small planets is well-accepted and mostly understood, how giant planets form and evolve is still under debate. One approach towards understanding giant planet formation and evolution process is to study the associated debris disks. Debris disks are composed of dust produced by planetesimals that are in orbit around main sequence stars. The grain composition, dust distribution, and disk morphology can be used to infer the system's dynamical history and even predict the possible existence of unseen exoplanets.

My thesis focuses on studying the debris disk around HD 131835 with multi-wavelength high-contrast imaging. Multi-wavelength imaging allows us to characterize the distribution of grains of various sizes since an observation is most sensitive to grains with the size similar to the probing wavelength. The target, HD 131835, is a  $\sim 15$  Myr A2 star in the Scorpius-Centaurus OB association at a distance of  $\sim 120$  parsec. I first report the discovery of the resolved disk around HD 131835 in mid-infrared at  $11.7 \mu\text{m}$  and  $18.3 \mu\text{m}$  with T-ReCS on Gemini South. Next, I present the first scattered-light image of the debris disk around HD 131835 using the Gemini Planet Imager (GPI). The disk is detected in  $H$ -band polarized light. Compared to its mid-infrared thermal emission, the disk in scattered light shows

similar orientation but different morphology. Unlike the continuous and extended feature in thermal emission, the disk in scattered light has a cleared region inward of  $\sim 75$  AU. In addition, I discover a weak brightness asymmetry along the major axis that is only present in the scattered-light image. The results of my thesis work imply that the system has multiple grain populations, and those grains could be composed of a mixture of silicates and amorphous carbon. The brightness asymmetry and the richness in the morphological features indicate that the system is dynamic, possibly with strong interactions between dust and gas and perturbations from unseen objects. In the final chapters, I present my instrumentation work including developing the photometric calibration method in the polarimetry mode for the GPI coronagraphic observations and creating a more automatic process for aligning the focal plane mask to the star while observing.

The dissertation of Li-Wei Hung is approved.

Jonathan Lloyd Mitchell

Bradley M. Hansen

Michael P. Fitzgerald, Committee Chair

University of California, Los Angeles

2016

*To Mom, Dad, and Sister*  
*To Adam Reed*  
*And*  
*To the memory of my grandma*

# TABLE OF CONTENTS

<b>1</b>	<b>Introduction</b>	<b>1</b>
<b>2</b>	<b>Discovery of Resolved Debris Disk Around HD 131835</b>	<b>8</b>
2.1	INTRODUCTION	8
2.2	OBSERVATIONS	11
2.3	DATA PROCESSING	12
2.3.1	Image Reduction	12
2.3.2	Photometry	15
2.3.3	PSF Subtraction	18
2.4	MODELING AND ANALYSIS	18
2.4.1	Stellar Properties	20
2.4.2	Model	20
2.5	DISCUSSION	30
2.6	SUMMARY	35
2.7	ACKNOWLEDGEMENTS	35
<b>3</b>	<b>First Scattered-light Image of the Debris Disk around HD 131835 with the Gemini Planet Imager</b>	<b>36</b>
3.1	INTRODUCTION	36
3.2	OBSERVATIONS AND DATA REDUCTION	37
3.2.1	Observations	37
3.2.2	Data Reduction	38
3.2.3	Photometric Calibration	38
3.3	MORPHOLOGY OF THE SCATTERED-LIGHT DISK	39

3.4	LIMITS ON DISK TOTAL INTENSITY . . . . .	41
3.5	LIMITS ON POINT SOURCES . . . . .	42
3.6	MODELING THE SCATTERED-LIGHT DISK . . . . .	42
3.7	DISCUSSION AND SUMMARY . . . . .	49
<b>4</b>	<b>Gemini Planet Imager Observational Calibration XII: Photometric Calibration in the Polarimetry Mode . . . . .</b>	<b>51</b>
4.1	INTRODUCTION . . . . .	51
4.2	MEASURING SATELLITE SPOT FLUX IN POLARIMETRY MODE . . . . .	53
4.3	CALIBRATION USING SATELLITE SPOTS DIRECTLY . . . . .	55
4.3.1	Calibration Method . . . . .	55
4.3.2	Calibration Uncertainty . . . . .	55
4.3.3	GPI Data Reduction Pipeline Implementations . . . . .	59
4.3.4	Photometry of HD 19467 B . . . . .	59
4.3.5	Photometry of Beta Pictoris b . . . . .	60
4.3.6	Detection Throughput Correction . . . . .	62
4.4	CALIBRATION USING SPECTROSCOPY MODE OBSERVATIONS . . . . .	65
4.4.1	Calibration Method . . . . .	65
4.4.2	Scaling Factor . . . . .	66
4.5	SUMMARY AND FUTURE WORK . . . . .	68
<b>5</b>	<b>Conclusions . . . . .</b>	<b>71</b>
<b>6</b>	<b>Appendix: GPI FPM Alignment Pipeline Work . . . . .</b>	<b>75</b>
6.1	INTRODUCTION . . . . .	75
6.2	GPI INSTRUMENTAL POLARIZATION . . . . .	75
6.3	MEASURING THE FPM POSITION . . . . .	79

## LIST OF FIGURES

2.1	The first resolved images of the debris disk around HD 131835 . . . . .	14
2.2	The spectral energy distribution (SED) of the HD 131835 system . . . . .	17
2.3	SED of the debris disk with the best-fit three-population model . . . . .	27
2.4	The disk images and the best-fit three-component model . . . . .	28
2.5	Equilibrium temperatures of the disk model components and various grains .	32
3.1	The resolved debris disk around HD 131835 in polarized scattered light . . .	40
3.2	Limits on point-source detection from the GPI observations . . . . .	43
3.3	Comparison of the best-fit MCFOST image model to the observations . . . .	45
3.4	Comparison of the best-fit MCFOST SED model to the observations . . . .	46
4.1	HD 118666 observed with the coronagraph in polarimetry mode with the labeled apertures for measuring satellite spot fluxes . . . . .	53
4.2	Companion-to-satellite spot flux ratio . . . . .	58
4.3	GPI photometric measurements of HD 19467 B in <i>H</i> band polarimetry mode	61
4.4	<i>H</i> -band photometry of $\beta$ Pictoris b . . . . .	63
5.1	Debris disk around HD 131835 in scattered light and thermal emission . . .	72
6.1	Instrumental polarization of GPI estimated with unpolarized stars . . . . .	78
6.2	Features of the instrumental polarization . . . . .	80
6.3	Misalignment between the star and the FPM viewed using GPI-tv . . . . .	82

## ACKNOWLEDGMENTS

First and foremost, I thank my parents, my sister, and my boyfriend. Their unconditional love and support have inspired me to get where I am today. I thank my mom, Shih-Hwa Shiao, and my dad, Tsung-Min Hung, for introducing me to the wonders of science through teaching me scientific reasoning from even before I can remember. I thank my sister, Li-Chi Hung, for being my best mentor and consultant in all aspects, in school and in life. I thank my boyfriend, Adam Reed, for always being there for me, in good times and in bad times, despite the fact that we are separated by a thousand miles. They always support my important life decisions, from pursuing an astronomy PhD to my career choice. I thank them and love them all from the bottom of my heart.

I am also thankful to my research advisor, mentors, and collaborators. I thank my graduate advisor, Mike Fitzgerald, for his support and mentorship over these five years. I am particularly grateful for him being always available whenever I needed it, helping me win the National Science Foundation (NSF) Graduate Research Opportunities Worldwide (GROW) funding, and establishing and securing my niche within the larger research collaboration. I thank the GPI team leaders, especially Bruce Macintosh, James Graham, and Paul Kalas, for creating a friendly research environment that fosters the success of the juniors in the team. I thank Marshall Perrin for being a great leader of the GPI Data Reduction Pipeline (DRP) work and hosting the data telecom meetings. I am proud of being a member of the GPI DRP software and documentation team! I thank Gaspard Duchêne for treating me as a real scientist in our collaborations. Also, I feel very lucky and am very thankful to have the following mentors who introduced me to physics and astronomy research during my undergraduate study, teaching me numerous research skills from ground zero: Thomas Lemberger, Saeqa Vrtilek, Ryan Hickox, Roberto De Propriis, Andy Gould, and Jennifer Yee.

I would also like to thank my friends, colleagues, the UCLA astronomy graduate community, and our computer experts. I thank Sarah Logsdon for being my awesome classmate, roommate, and friend who I can share my life with. I thank Xinnan Du for supporting me through her authentic cooking. I thank Laura Haney and Nathan Tung for influencing me

through their enthusiasm for teaching. I thank Anna Boehle for the friendship and companionship. I thank my officemate Sean Lake for offering helpful research discussions and programing advice. I would like to thank the entire UCLA astronomy graduate community for making the culture here supportive, diverse, and fun. During these five years of my PhD study, there were multiple times where my “lab equipment” did not want to cooperate. Special thanks to Chris Johnson, Nick Robertson, and Debra MacLaughlan-Dumes who not only helped me solve problems but also taught me useful knowledge in hardware, software, and website design.

Finally, I would like to thank many UCLA alumni for sharing their tips for excelling in graduate school, helping me at various stages through my graduate study, and offering honest advice about different career paths: Tom Esposito, Shane Frewen, Robin Rehagen, Thomas Rehagen, Nate Ross, Jeff Chilcote, Greg Mace, Siyi Xu, Kim Phifer, Betsy Mills, Julia Fang, Kathy Kornei, Sylvana Yelda, Ian Crossfield, David Rodriguez, Sarah Lipscy, and Christine Chen.

Chapter 2 is a version of Hung et al. (2015a). Chapter 3 is a version of Hung et al. (2015b). Both Chapter 2 and 3 are reproduced by permission of the AAS. Chapter 4 is a version of Hung et al. (2016) and is reproduced by permission of the SPIE. I would like to thank my collaborators on these works: Michael Fitzgerald, Christine Chen, Tushar Mittal, Paul Kalas, James Graham, Gaspard Duchêne, Pauline Arriaga, Jérôme Maire, Christian Marois, Maxwell Millar-Blanchaer, Sebastian Bruzzone, Abhijith Rajan, Laurent Pueyo, Robert De Rosa, Quinn Konopacky, Schuyler Wolff, Stanimir Metchev, Anand Sivaramakrishnan, and the GPIES team.

I thank National Science Foundation for supporting my research through the Graduate Research Fellowship and GROW.

## VITA

- 2011            B.S. (Physics, Astronomy), The Ohio State University, Ohio, USA.  
*Summa Cum Laude,*  
*with Research Distinction in Astronomy*
- 2013            M.S. (Astronomy), UCLA, California, USA.

## PUBLICATIONS

Hung, L.-W., Bruzzone, S., Millar-Blanchaer, M. A., Wang, J. J., Metchev, S., Fitzgerald, M. P., Sivaramakrishnan, A., and GPIES. “Gemini Planet Imager Observational Calibration XII: Photometric Calibration in the Polarimetry Mode.” 2016, *Society of Photo-Optical Instrumentation Engineers (SPIE) Conference Series*, submitted

Hung, L.-W., Duchêne, G., Arriaga, P., Fitzgerald, M. P., and 33 coauthors. “First Scattered-light Image of the Debris Disk around HD 131835 with the Gemini Planet Imager.” 2015, *The Astrophysical Journal Letters*, 815, L14

Hung, L.-W., Fitzgerald, M. P., Chen, C. H., Mittal, T., Kalas, P. G., and Graham, J. R. “Discovery of Resolved Debris Disk around HD 131835.” 2015, *The Astrophysical Journal*, 802, 138

Hung, L.-W., Bañados, E., De Propriis, R., West, M. J. “The Galaxy Alignment Effect in Abell 1689: Evolution, Radial, and Luminosity Dependence.” 2010, *The Astrophysical Journal*, 720, 1483

Hung, L.-W., Hickox, R. C., Boroson, B. S., Vrtillek, S. D. “Suzaku X-ray Spectra and Pulse Profile Variations During the Superorbital Cycle of LMC X-4.” 2010, *The Astrophysical Journal*, 720, 1202

Yee, J. C., Hung, L.-W., Bond, I. A., Allen, W., and 128 coauthors. “MOA-2010-BLG-311: A Planetary Candidate below the Threshold of Reliable Detection.” 2013, *The Astrophysical Journal*, 769, 77

Bañados, E., Hung, L.-W., De Propriis, R., West, M. J. “The Faint End of the Galaxy Luminosity Function in A1689: A Steep Red Faint End Upturn at  $z = 0.18$ .” 2010, *The Astrophysical Journal Letters*, 721, L14

Macintosh, B., Graham, J. R., Barman, T., De Rosa, R. J., and 84 coauthors. “Discovery and spectroscopy of the young Jovian planet 51 Eri b with the Gemini Planet Imager.” 2015, *Science*, 350, 64

# CHAPTER 1

## Introduction

Over 5000 astonishingly diverse extrasolar planets (exoplanets) have been discovered in the last two decades, indicating that the planets in our solar system are not unique. These exoplanets and planetary systems have an enormous range of properties. For example, there is a group of high-temperature giant planets, named “hot Jupiters”, orbiting very close to their host stars. While Jupiter takes more than ten years to orbit around the Sun, it only takes a couple days for a typical hot Jupiter to complete its orbit. In contrast, there are other systems that are more similar to our solar system. HR 8799, for example, hosts four giant planets that are distributed like a scaled-up version of our outer solar system (Marois et al., 2010). The enormous range of exoplanets with varied characteristics demands understanding of how these planets form and evolve. While the formation mechanism for small planets is well-accepted, the formation mechanism for giant planets is still under debate. Outstanding questions include: Do giant planets form through core accretion like the mechanism for forming small planets (Marcy et al., 2000) or through a collapsing phase more similar to the star formation process (Boss, 1997)? Also, where is the birthplace of giant planets and how do they migrate as they evolve? One approach towards understanding giant planet formation and evolution process and their demographics is to study the associated debris disks.

Debris disks are composed of dust produced by planetesimals that are in orbit around main sequence stars; the planetesimals in these systems are early analogs to the bodies in the asteroid and Kuiper belts in our solar system. The materials in debris disks around main-sequence stars are thought to be the second generation since the primordial disks dissipate in the time scale of only a few million years (Haisch et al., 2001). The presence of the secondary disks indicates that the dust is constantly being replenished (Backman & Paresce,

1993), possibly due to collisions between planetesimals and sublimation of comets (Harper et al., 1984). The properties of a given debris disk are tightly linked to the interactions between different bodies in the system. As a result, knowing the debris disk environments around planet-hosting stars can constrain giant planet formation and evolution models.

Most of the debris disks are discovered through detecting their infrared (IR) excess and characterized by their spectral energy distributions (SEDs). However, studying their SEDs alone provides only limited information. While the disk temperature and the total IR flux can be well determined from the SEDs, the spatial information of the systems is inaccessible. There is a possibility that the excess actually originates from an unrelated foreground or background source contaminating the beam. Even if the IR excess truly originates from the disk, the location of the grains will be degenerate with the grain properties. For example, small grains further away from the star might output the same amount of flux as large grains that are closer in. Furthermore, due to this degeneracy, the SED alone for a multiple temperature debris disk is insufficient in confirming whether it is a single belt or multiple belts system.

By spatially resolving a debris disk, we can acquire critical information necessary for modeling planet formation and migration processes. With resolved images of a disk, we can determine the morphology of the disk and its grain-size distribution. For example, we can see if dust is distributed more like in a thin ring or more like in a continuous disk. We can also characterize the abundance of small dust particle in comparison to larger ones. Most planet formation and evolution models require knowing how the grains are distributed in order to accurately propagate the evolution of the system through time. The disk morphology and the grain-size distribution will inform us about the underlying physics responsible for dust distribution and constrain the locations and nature of the larger parent bodies.

In addition, a debris disk can also provide a glimpse of dynamical interactions between objects in the system. For example, if two 100 – 1000 km objects catastrophically collide at distances of 3 – 5 au or less from the parent star, clumps or rings of dust are expected to form (Kenyon & Bromley, 2005). However, if no violent collisions are involved but instead the planetesimals were disturbed through a more gentle process while a giant planet migrates

through the disk, the planetesimals are expected to be excited into higher eccentricities (Edgar & Artymowicz, 2004). Therefore, understanding the structure of the disk, inferred from spatially resolved images, may reveal the current dominant physical processes in the system and the traces left from its dynamical history.

More directly connected to spatially resolved images of the distribution of small grains, the morphology of the planetesimal belts might be closely related to the presence of unseen planets dynamically sculpting the disk. HR 4796A, for example, has an inclined ring with one lobe being  $\sim 5\%$  brighter than the other (Telesco et al., 2000). Wyatt et al. (1999) argued that long term perturbations from a planet with mass  $> 0.1$  mass of Jupiter located close to the inner edge of the disk could introduce this brightness asymmetry. The planet would impose the forced eccentricity on the ring, causing one side of the ring being closer to the star and thus showing the “pericenter glow.” Such incidence demonstrates the level of information that can be provided from direct imaging disks.

Finally, if a planet is detected along with the disk, we can potentially constrain the planet’s orbit in a single epoch of imaging when using the disk morphology. In order to determine a planet’s orbit around the star, the system typically needs to be observed several years apart for the displacement to be identifiable. If a planet is in a very wide orbit, the orbit characterization can be even more challenging due to the slow orbital speed of the planet. Fortunately, if a disk is present in the system, we can use the disk morphology to constrain the planet’s orbital properties such as its eccentricity, orbital period, and semi-major axis. This method is based on the fact that the planet’s orbital motion is likely to affect the property of the disk. Therefore, with direct images of the disk, we do not rely on detecting planet’s movement so only a single epoch of observation is required.

Complete characterization of debris disks demands multi-wavelength observations. Different wavelengths probe grains of different sizes since dust grains are not perfect blackbodies. When the wavelength is much longer than the grain size, dust grains do not couple efficiently to radiation. In other words, only grains larger than the observing wavelengths are detectable. However, there are more small grains than large grains. The size distribution of debris is commonly approximated by a power law with the index  $\sim -3.5$  (e.g., Dohnanyi

1969, Wyatt et al. 2011), indicating small dust grains outnumber large ones. Together, when considering the radiation coupling efficiency with the size distribution, an observation is most sensitive to grains with the size similar to the probing wavelength. For this reason, resolving debris disks at multiple wavelength provide invaluable information on characterizing the distribution of grains of various sizes.

My thesis focuses on the multi-wavelength study of the resolved debris disk around HD 131835. Imaging debris disks is extremely difficult because disks are so faint compared to their host stars. Techniques and instruments for imaging debris disks have just started to mature in the recent decades. I use these state-of-the-art high-contrast debris disk images in mid- and near-IR to characterize the spatial distribution, size distribution, chemical composition, and optical properties of dust in the planetary system.

Wavelengths in mid-IR are the best for studying the thermal emission from the debris disks. In mid-IR, the emission from a disk originates from the dust and planetesimals that are being heated by the parent star. In other words, mid-IR shows the thermal emission from the debris disks. Mid-IR observations are most sensitive to grains with size of  $\sim$  tens of micron. While emission from the stars usually peaks in the visible, the thermal emission from the disks peaks in the mid-IR. The mid-IR emission from the disks can be orders of magnitude more than the contribution from the stellar atmospheres. Observing in mid-IR wavelengths therefore provides us an optimal observational advantage in the sense that the flux ratio of the disk to the star is maximized.

In Chapter 2, I report the discovery of the resolved disk around HD 131835 and present the analysis and modeling of its thermal emission. HD 131835 is a  $\sim$ 15 Myr A2 star in the Scorpius-Centaurus OB association at a distance of  $122.7^{+16.2}_{-12.8}$  parsec. The extended disk has been detected to  $\sim 1.5''$  (200 au) at  $11.7 \mu\text{m}$  and  $18.3 \mu\text{m}$  with T-ReCS on Gemini South. The disk is inclined at an angle of  $\sim 75^\circ$  with the position angle of  $\sim 61^\circ$ . The flux of HD 131835 system is  $49.3 \pm 7.6$  mJy and  $84 \pm 45$  mJy at  $11.7 \mu\text{m}$  and  $18.3 \mu\text{m}$  respectively. A model with three grain populations gives a satisfactory fit to both the spectral energy distribution and the images simultaneously. This best-fit model is composed of a hot continuous power-law disk and two rings. We characterized the grain temperature profile and found that the

grains in all three populations have temperatures higher than the equilibrium temperature of a blackbody. In particular, the grains in the continuous disk are unusually warm; even when considering small graphite particles as the composition.

Wavelengths in near-IR, on the other hand, show the scattered light and trace smaller particles comparing to the mid-IR observations. Resolving the disk in more than one wavelengths can provide us powerful leverages on constraining the grain properties. However, it is extremely difficult to image an exoplanet or a debris disk in scattered light directly because they are so faint compared to the host star. For example, the exoplanets' fluxes from HR 8799 b, c, and d are only one one hundred thousandth of the flux from the star (Marois et al., 2008), equivalent of having the contrast ratio of  $10^{-5}$ ! For comparison, a typical digital camera only has the contrast ratio on the order of  $10^{-2}$ . To put these numbers in perspective, imaging an exoplanet in scattered light requires more extreme contrast than detecting the emission from a LED bulb in front of an industrial construction light from a distance of 200 miles. Additionally, diffraction and scattering also limit the imaging resolution. Such challenges kept the astronomers from directly imaging the first exoplanet until 2004 (Chauvin et al., 2004). Even though there are more than a thousand exoplanets and debris disks discovered so far, only a few percent are detected through direct imaging.

In order to directly image exoplanets and debris disks with greater efficiency and better sensitivity, our major collaboration built the world class instrument Gemini Planet Imager (GPI). GPI is the world's first high-contrast instrument equipped with the extreme adaptive optics (AO) specially designed for direct imaging and spectroscopy of exoplanets and debris disks. The extreme AO increases imaging quality by canceling the atmospheric distortions through a microelectromechanical system (MEMS) deformable mirror. The MEMS is controlled by one thousand five hundred actuators on the back and will configure to counteract on the wavefront distortions detected by the wavefront sensor. To achieve high contrast, GPI uses a high performance coronagraph to suppress the starlight and control diffraction and speckles. GPI's operating goal is to achieve a contrast of  $10^{-7}$  (Macintosh et al., 2008). GPI can obtain higher contrast images than the current Keck AO system.

GPI can perform imaging, spectroscopy, and polarized light observations. For the science

instrument, GPI is equipped with a near-IR integral field spectrograph (IFS). IFS has the capability for both imaging and spectroscopy; the light in each pixel of the image can be dispersed into a spectrum. This IFS capability enables us to study the composition of exoplanets' atmosphere through the spectra. GPI can also operate as a dual-channel integral field polarimeter. Observing in the polarimetry mode can significantly enhance disk structures by suppressing unpolarized starlight. With all these novel features, GPI is a leading instrument to push imaging exoplanets and debris disk study into a new era.

GPI is currently operating on the 8-meter Gemini South telescope located in Cerro Pachón, Chile, approximately nine thousand feet above sea level. The construction of the instrument started in 2007. In November 2013, the GPI Exoplanet Survey (GPIES) team released first-light images that include the image of HR 4796A and its debris disk. GPI shows promising early performance where these images are almost ten times better than images from the previous generation of instruments. In 2014, the GPIES team started carrying out an 890-hour survey to search for and characterize exoplanets and debris disks around 600 stars. The entire project will span three years total.

As a GPIES team member, I am actively involved in the data collection, pipeline development, and image analysis and modeling. From January to April 2015, I was awarded with the National Science Foundation Graduate Research Opportunities Worldwide grant to assist the data collection process and image analysis. During this program, I spent more than ten days total at the observatory on the summit helping with the data collection process of the campaign observing runs. I also contribute in developing the GPI Data Reduction Pipeline<sup>1</sup> to process and analyze the images taken with GPI. The second half of my thesis focuses on the work I have done as a member in the GPIES team.

In Chapter 3, I present the first scattered-light image of the debris disk around HD 131835 in the  $H$  band using the Gemini Planet Imager. HD 131835 is a  $\sim 15$  Myr old A2IV star at a distance of  $\sim 120$  pc in the Sco-Cen OB association. We detect the disk only in polarized light and place an upper limit on the peak total intensity. No point sources resembling exoplanets were identified. Compared to its mid-infrared thermal emission, the

---

<sup>1</sup><http://docs.planetimager.org/pipeline/index.html>

disk in scattered light shows similar orientation but different morphology. The scattered-light disk extends from  $\sim 75$  to  $\sim 210$  au in the disk plane with roughly flat surface density. Our Monte Carlo radiative transfer model can well describe the observations with a model disk composed of a mixture of silicates and amorphous carbon. In addition to the obvious brightness asymmetry due to stronger forward scattering, we discover a weak brightness asymmetry along the major axis, with the northeast side being 1.3 times brighter than the southwest side at a  $3\sigma$  level.

Finally, in Chapter 4 and the appendix, I present some instrumental calibration and characterization work associated with GPI. Since GPI is a relatively new and complex instrument, many calibration processes and characterization work are actively being developed. In chapter 4, I describe the photometric calibration method that we developed to convert the images from raw units to physical units in polarimetry mode. In the appendix, I present the effort we made in making the process for aligning the focal plane mask to the star more automatic with the goal to better characterize the instrumental polarization.

## CHAPTER 2

### Discovery of Resolved Debris Disk Around HD 131835

Reproduced by permission of American Astronomical Society journals  
(Hung, L.-W., Fitzgerald, M. P., Chen, C. H., et al. 2015, ApJ, 802, 138)

#### 2.1 INTRODUCTION

Planet formation and evolutionary history is imprinted on the nature and distribution of circumstellar debris. Circumstellar debris disks are composed of dust and planetesimals that are in orbit around main sequence stars, analogous to the asteroid belt and Kuiper belt in our solar system. The materials in the disks are thought to be the second generation where the dust is constantly being replenished (Backman & Paresce, 1993) from collisions between planetesimals and sublimation of comets (Harper et al., 1984). Most of the debris disks are discovered through detecting their infrared excess and characterized by their spectral energy distributions (SEDs). However, studying their SEDs alone provides only limited information. While the disk temperature and the total infrared (IR) flux can be well determined from the SEDs, the spatial information of the systems is inaccessible. In addition, there is a possibility that the excess actually originates from an unrelated foreground or background source contaminating the beam.

In addition, with the SED information only, the location of the grains will be degenerate with the grain properties. For example, small grains further away from the star might be heated to the same temperature as large grains that are closer toward the center. Thus, a single-temperature debris disk does not necessarily indicate all the grains are located in a thin ring. A similar argument applies to the opposite scenario where small grains might be

heated to a higher temperature compared to large grains at the same location. Therefore, for a multiple-temperature debris disk, the SED information alone is typically insufficient to distinguish between the cases where grains are located at the same spatial location (i.e., a ring) versus at multiple spatially distinct locations (i.e., belts or extended disks). Kennedy & Wyatt (2014) argued that this degeneracy is small for A-type stars, due to the truncation on the small end of the grain size distribution by radiation pressure. They proposed that most two-temperature disks around A-type stars probably arise from multiple spatial components. To confirm that the disk indeed has multiple spatial components, resolved images are required.

If the disks can be spatially resolved, we will be able to characterize the spatial distribution of the grains and the geometry of the disks. We can use distribution of grains to probe the underlying physics responsible for dust distribution, and constrain the locations and nature of the grain parent bodies. In addition, the morphology of the planetesimal belts might be closely related to the presence of unseen planets dynamically sculpting the disk. For example, as seen in mid-IR thermal emission, HR 4796A has an inclined ring with one lobe being  $\sim 5\%$  brighter than the other (Telesco et al., 2000). Wyatt et al. (1999) argued that the secular perturbations from a planet of mass  $> 0.1M_J$  located close to the inner edge of the disk could introduce this brightness asymmetry. The planet would impose the forced eccentricity on the ring, causing one side of the ring being closer to the star and thus showing the "pericenter glow." Such incidence demonstrates the level of information provided from the direct imaging far surpasses from the SED alone.

Here we have attempted to spatially resolve the disk around HD 131835, a system characterized solely by its SED prior to this work. Rizzuto et al. (2011a) assign a 91% membership probability to the Upper Centaurus Lupus (UCL) moving group (a subgroup of the Sco-Cen association) based on its Galactic location and velocity. HD 131835 is a young star ( $\sim 15$  Myr, based on the age of the UCL estimated by Mamajek et al. 2002a;  $\sim 16$  Myr, based on an analysis of F-type pre-main-sequence members of the group by Pecaute et al. 2012a) with a spectral type of A2IV (Houk, 1982) at the distance of  $d = 122.7^{+16.2}_{-12.8}$  pc (van Leeuwen, 2007a). The infrared excess emission of HD 131835 was first reported by Moór et al. (2006a)

through searching the *Infrared Astronomical Satellite (IRAS)* and *Infrared Space Observatory (ISO)* databases for the stars in the vicinity of the Sun. The MIPS data for this source were first published in Chen et al. (2012a) which shows the MIPS 24 and 70  $\mu\text{m}$  data for all of the de Zeeuw et al. (1999) ScoCen A-type stars and helps to put the excess emission for this star into context (e.g. it is one of only 4 UCL/Lower Centaurus Crux A-type stars with  $L_{\text{IR}}/L_*$  commensurate to beta Pic,  $> 10^{-3}$ ). Chen et al. (2014) found that the SED for HD 131835 can be described using a two-temperature model.

In contradiction to the traditional disk evolution scheme, CO gas in debris disks around A-type stars may be fairly common. Typically, the primordial gas dissipates in a few million year time scale during the protoplanetary phase. By the time it transforms into a debris system, the CO gas level will be undetectable. However, there are several exceptional cases. For example, 49 Cet and HD 21997 are 40 (Zuckerman & Song, 2012) and 30 (Torres et al., 2008) Myr old A-type stars hosting gas-rich disks (Zuckerman et al. 1995; Moór et al. 2011). The gas is believed to be the second generation, possibly due to violent comet collisions (Zuckerman & Song, 2012). In the case of HD 21997, there is an alternative explanation based on a recent ALMA observation which indicates that the gas may be of primordial origin in this system (Kóspál et al., 2013). Another possible production mechanism involves constant resurfacing of the parent bodies and sublimation or photodesorption of the CO ice. For the  $\beta$  Pic system, its CO distribution is particularly interesting because it is not the same as the dust, even more highly asymmetric and may imply the presence of a second undetected planet (Dent et al., 2014). Not only has CO been detected and characterized for  $\beta$  Pic, 49 Cet, and HD 21997 but it has also been detected around 5 A-type stars in Upper Sco (Hughes 2014, private communication).

Besides having the IR excess from the dusty debris, HD 131835 hosts a detectable amount of carbon monoxide gas (Moór et al. 2013, Moór et al. in prep). For HD 131835, Kastner et al. (2010) first reported the nondetection of CO emission with the 30-m Institut de Radio Astronomie Millimetrique telescope. However, Zuckerman & Song (2012) argued that if the comet collision model is correct, then the  $\text{H}_2/\text{CO}$  ratio is unconstrained and thus the upper mass limit of the CO gas for HD 131835 is  $4.06 \times 10^{-3} M_E$ . Later, Moór et al.

(2013) announced the discovery of detected submillimeter CO emission with the Atacama Pathfinder EXperiment (APEX) radio telescope through a survey. Once the CO gas is well characterized, it can provide us valuable information on the disk environment and the dust-gas associations of such system with the coexistence of gas and debris at an age  $\gtrsim 10$  Myr.

Here we report the discovery of the spatially resolved debris disk around HD 131835 at mid IR wavelengths, tracing the thermal emission from the grains. Currently, these images are the only resolved images of the system. In this paper, we present the analysis, modeling, and characterization of the debris disk around HD 131835. Our mid IR images are based on two epochs of observation as described in § 2.2. The data processing details, including image reduction, photometry, and PSF subtraction, are in § 2.3. In § 2.4, we analyze the stellar properties and show that a three-component model is required to describe the system. In § 2.5, we characterize the grain temperatures in the system and investigate the possible grain compositions. We also briefly discuss how the current generation of imaging instruments and telescopes can improve our understanding of debris disks in the near future. Finally, we summarize our modeling results in § 2.6.

## 2.2 OBSERVATIONS

We used the T-ReCS instrument on the Gemini South telescope to obtain mid-IR imaging of HD 131835 in two programs, GS-2008A-Q-40 and GS-2009A-Q-19. As part of these programs, the star HD 136422 was also observed as a photometric and point-spread function (PSF) calibration standard. The observations of the reference star were interleaved between the observations of the target. All the images are taken in the Si-5 ( $\lambda_c = 11.66 \mu\text{m}$ ,  $\Delta\lambda = 1.13 \mu\text{m}$ ) and Qa ( $\lambda_c = 18.30 \mu\text{m}$ ,  $\Delta\lambda = 1.51 \mu\text{m}$ ) filters. In these bands, the T-ReCS pixel size is  $0.08976'' \pm 0.00021''$  on the sky.<sup>1</sup> Due to the high sky background and instrumental thermal background, we used the standard mid-IR ABBA chop-and-nod observing technique with a  $15''$  throw between chop-nod positions.

---

<sup>1</sup><http://www.gemini.edu/sciops/instruments/t-recs/spectroscopy/detector>

Since the disk had not been resolved prior to the 2008 observations, the first epoch data were obtained with an arbitrary chop position angle. This turned out to be very close to the apparent position angle of the disk. To confirm that the feature was truly from the emission of the resolved disk and not from artifacts due to imperfect chopping and nodding, the second epoch of observation was obtained in 2009 with the chop position angle roughly perpendicular to the previous one. Observation conditions were generally very good, with diffraction rings visible in the calibration images. The sky was very transparent, with low water vapor ( $< 1$  mm) measured towards zenith for the most of the nights. The processed images of HD 136422 gave diffraction-limited resolution of  $\sim 0.39''$  and  $\sim 0.54''$  at  $11.7 \mu\text{m}$  and  $18.3 \mu\text{m}$  respectively. HD 131835 (and HD 136422) were observed in two nights in 2008 and four nights in 2009, with the total on source time of 6168 (2056) seconds at  $11.7 \mu\text{m}$  and 5734 (1303) seconds at  $18.3 \mu\text{m}$ . Details of the observations are summarized in Table 2.1.

## 2.3 DATA PROCESSING

### 2.3.1 Image Reduction

We reduced all the images following the standard mid-infrared data reduction procedures. We linearly combined the chop and nod frames within each image to remove the instrumental and sky background. We then subtracted the average row background and corrected for the column offset due to small bias variations among different channels. The cores of the PSF standard star HD 136422 are fairly circular (as shown in Fig. 2.1 c and d) with the FWHM of  $\sim 0.39''$  and  $\sim 0.54''$  at  $11.7 \mu\text{m}$  and  $18.3 \mu\text{m}$  respectively. The target images in both wavelengths show the extended and elongated emission compared to the PSFs. Before the PSF subtraction process, these mid-IR images already show prominent disk emission extending beyond  $1''$  along the semi-major axis in both bands.

Table 2.1. Observations with Gemini S / T-ReCS

Program ID (GS-20+)	PA (deg)	UT Date	Star	Filter	Integration Time (sec)
08A-Q-40	55	2008-05-08	HD 131835	Si-5	318.5
				Qa	1216.3
			HD 136422	Si-5	86.9
				Qa	144.8
09A-Q-19	148	2008-05-11	HD 131835	Si-5	637.1
				HD 136422	Si-5
		2009-04-18	HD 131835	Qa	3011.7
				HD 136422	Qa
2009-04-19	HD 131835	Si-5	3127.5		
		HD 136422	Si-5	1013.5	
2009-05-23		HD 131835	Si-5	1042.5	
			Qa	1505.8	
			HD 136422	Si-5	434.4
			Qa	434.4	
2009-07-12		HD 131835	Si-5	1042.5	
			HD 136422	Si-5	434.4
Total			HD 131835	Si-5	6168.2
				Qa	5733.8
			HD 136422	Si-5	2056.0
				Qa	1303.1

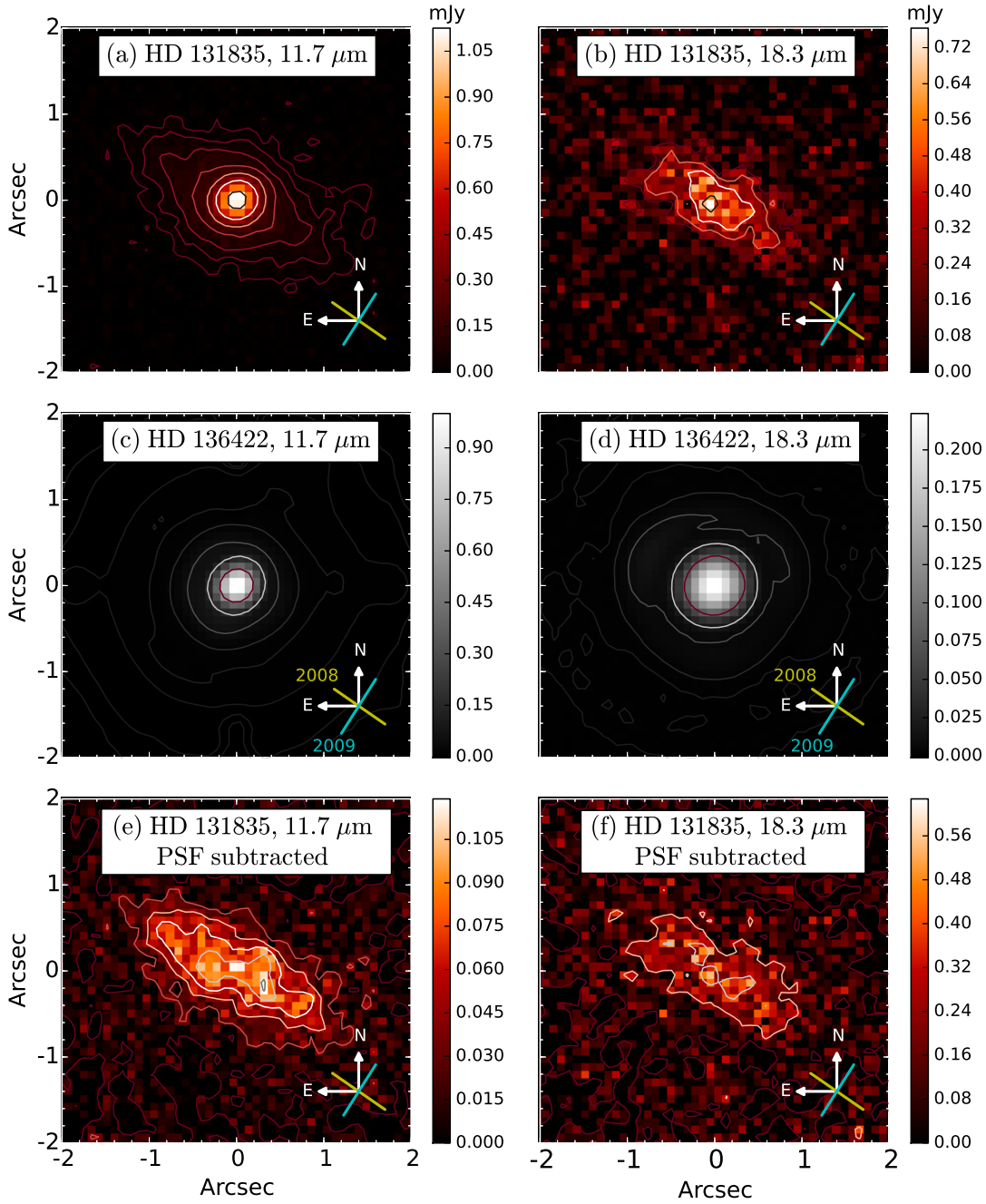


Figure 2.1 (a) and (b) are the images of HD 131835 from T-ReCS on Gemini South at 11.7  $\mu\text{m}$  and at 18.3  $\mu\text{m}$ . (c) and (d) are the corresponding images of the reference star HD 136422 scaled to the stellar flux of the target. Contours in (a)-(d) are spaced in logarithmic scales. (e) and (f) are the PSF subtracted images of HD 131835, and contours are spaced by the 1- $\sigma$  background noise level. In both wavelengths, the disk is resolved out to approximately 200 au. The lines on the lower right-hand corners indicate the chop position angles for observations in 2008 and 2009 epochs.

### 2.3.2 Photometry

We performed aperture photometry on HD 131835 using HD 136422 as the photometric reference. The flux of HD 136422 was taken from Cohen et al. (1999). We applied aperture correction to our photometry measurement on HD 131835. Based on the observations of HD 136422, the PSF structure was fairly stable over the course of each night; the enclosed flux in an aperture radius of  $1''$  usually varied only from 1 to 3 %. Thus, we adopted one relationship of aperture radius versus enclosed flux fraction for each night. Due to the nonuniform residual background, the enclosed flux fluctuated at large aperture radii. We characterized these fluctuations as the uncertainties of the radius-enclosed flux relationships.

Next, we applied atmospheric extinction correction and color correction. The atmospheric extinction varied from 0.09 to 0.19 magnitude per airmass among different nights in both bands. These values are consistent with the extinction observed on Mauna Kea (Krisciunas et al., 1987), where the conditions are similar to Cerro Pachón. For color correction, since the  $11.7 \mu\text{m}$  and  $18.3 \mu\text{m}$  fell within the wavelength coverage of the IRS spectrum, we used its shape to compute the correction factors. Detailed information about the IRS data is provided in § 2.4. The final flux of HD 131835 is  $49.3 \pm 7.6$  mJy for  $11.7 \mu\text{m}$  and  $84 \pm 45$  mJy for  $18.3 \mu\text{m}$ .

We have considered uncertainties from the process of measuring the target’s flux, the standard star’s flux, the aperture correction, and the extinction correction. However, by comparing the photometry measurement from each image (33 images at  $11.7 \mu\text{m}$  and 14 images at  $18.3 \mu\text{m}$ ), we noticed the systematic errors dominated over the random errors. Thus, being conservative, we quoted the sample standard deviations of photometry measurements from the ensemble of images as the uncertainties of our mean fluxes. Our measured fluxes are consistent with the values from the IRS spectrum. Table 2.2 lists the flux measurements of HD 131835 from this work and from other published literature, and the SED is shown in Fig. 2.2.

Table 2.2. Summary of the Measured Fluxes of HD 131835

Wavelength ( $\mu\text{m}$ )	Source	Flux (mJy)	Flux <sub>cc</sub> <sup>e</sup> (mJy)	References
0.43	<i>Hipparcos</i>	$2571 \pm 48$		(1)
0.55	<i>Hipparcos</i>	$2728 \pm 26$		(1)
1.24	2MASS	$1448 \pm 29$		(2)
1.66	2MASS	$965 \pm 35$		(2)
2.16	2MASS	$652 \pm 11$		(2)
3.4	WISE	$237.2 \pm 5.8$ <sup>a,b</sup>		(3)
4.6	WISE	$166.8 \pm 4.7$ <sup>a</sup>	$165.3 \pm 4.7$	(3,4)
11.7	Gemini S/T-ReCS	$49.7 \pm 7.7$	$49.3 \pm 7.6$	(5)
12	WISE	$49.1 \pm 2.2$ <sup>a</sup>	$49.4 \pm 2.2$	(3,4)
18.3	Gemini S/T-ReCS	$83 \pm 44$	$84 \pm 45$	(5)
22	WISE	$160.5 \pm 9.4$ <sup>a,c</sup>		(3)
24	<i>Spitzer</i> /MIPS	$153.1 \pm 3.1$	$161.7 \pm 3.3$	(6,7,8)
25	IRAS	$186 \pm 34$	$224 \pm 40$	(9)
60	IRAS	$684 \pm 62$	$681 \pm 61$	(9)
70	<i>Spitzer</i> /MIPS	$659.2 \pm 44.7$ <sup>d</sup>	$710.0 \pm 48.1$	(7,8,10)
90	AKARI/FIS	$560 \pm 39$	$583 \pm 41$	(11,12)
870	APEX/LABOCA	$8.5 \pm 4.4$		(13)
5.2 – 37.9	<i>Spitzer</i> /IRS Spectrum	...		(6)

<sup>a</sup>The quoted WISE data are based on aperture photometry. The error has included the uncertainty from the RMS scatter in the standard calibration stars.

<sup>b</sup>This is a lower limit due to saturation.

<sup>c</sup>This is an upper limit due to source confusion.

<sup>d</sup>The error is calculated by considering the source photon counting uncertainty, the detector repeatability uncertainty, and the absolute calibration uncertainty

<sup>e</sup>Color Corrected Flux

References. — (1) Høg et al. 2000; (2) Cutri et al. 2003a; (3) Cutri & et al. 2012; (4) Wright et al. 2010; (5) this paper; (6) Chen et al. 2014; (7) MIPS Instrument Handbook (Version 3.0, March 2011) by MIPS Instrument and MIPS Instrument Support Teams; (8) Rieke et al. 2004; (9) Moór et al. 2006a; (10) Chen et al. 2012a; (11) Yamamura et al. 2010; (12) Liu et al. 2014; (13) Nilsson et al. 2010

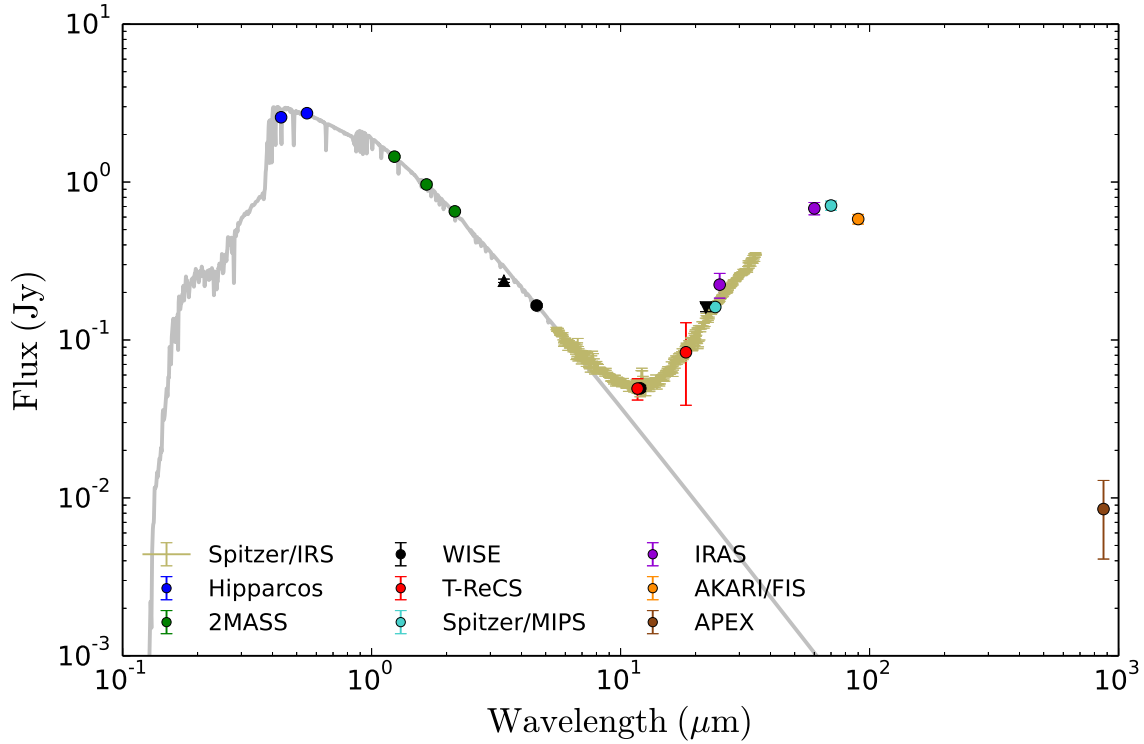


Figure 2.2 SED of the HD 131835 system. There are 15 well characterized photometry points and an IRS spectrum. The 11.7  $\mu\text{m}$  and 18.3  $\mu\text{m}$  T-ReCS photometry points are measured in this paper. Reference of other points are listed in Table 2.2. Note that the two triangle WISE points in 3.4  $\mu\text{m}$  and 22  $\mu\text{m}$  are the lower and upper limits. Well characterized photometry points between 3 and 100  $\mu\text{m}$  are color corrected. Only the points with wavelength < 5.8  $\mu\text{m}$  are used to fit for the stellar atmosphere. The model is described in § 2.4.1, and the gray line shows the best fit.

### 2.3.3 PSF Subtraction

After linearly combined the ABBA frames within each fits image, we weighted combined all these individual image files to produce one final high signal-to-noise ratio (SNR) image in each band. The uncertainty for each pixel in the final images was calculated by propagating the errors through the combination process. The PSF was constructed by a similar process except for the weight used for stacking the target images.

The target, PSF, and PSF-subtracted final images are shown in Fig. 2.1. The diagonal lines in the figure represent the chop position angles. The chop position angle was rotated roughly  $90^\circ$  from 2008 to 2009 due to the resolved disk structure as described in § 2.2. We scale the PSF to the target star flux, then subtract the stellar flux out from the target images. § 2.4.1 describes the stellar flux characterization in detail. By processing the 2008 and 2009 data separately, we see that 2009 observation alone confirms the detection of the structure and shows the position angle of the disk that is consistent with the observations made in 2008. Thus, we are confident that the elongated structure detected in 2008 is real, rather than an artifact arising due to imperfect chop-nod motion.

In both bands, the central region of the disk is generally brighter than the outskirt. The detected SNR is greater than 6 and 2 at  $11.7 \mu\text{m}$  and  $18.3 \mu\text{m}$  respectively. At  $11.7 \mu\text{m}$  the extended structure is detected at  $1 \sigma$  out to  $\sim 1.5''$  and  $0.7''$  in the major and minor axes, corresponding to  $\sim 180$  au and  $\sim 85$  au from the star in projection. The  $18.3 \mu\text{m}$  emission is resolved out to  $\sim 130$  au. Such extended disk structure in the mid-IR suggests the presence of warm dust far away from the star.

## 2.4 MODELING AND ANALYSIS

The infrared excess of HD 131835 has been measured in multiple wavelengths. Table 2.2 shows the summary of the measurements taken from the published literature. HD 131835 was detected in all four *WISE* bands (Cutri & et al., 2012). However, the *WISE* w1 measurement represents a lower limit due to saturation, and w4 measurement is an upper limit due to

source confusion, as flagged in the *WISE* catalog by Cutri & et al. (2012). The *IRAS* photometry measurements are taken from Moór et al. (2006a). The *Spitzer*/*MIPS* 24  $\mu\text{m}$  and 70  $\mu\text{m}$  measurements are taken from Chen et al. (2014) and Chen et al. (2012a). The object 1456545-354138 in the *AKARI* catalog (Yamamura et al., 2010) was identified as HD 131835 by Liu et al. (2014). Among the four *AKARI*/*FIS* bands, only the source measured in 90  $\mu\text{m}$  is confirmed and reliable (Yamamura et al., 2010). Finally, the longest wavelength point on the SED was measured in 870  $\mu\text{m}$  by Nilsson et al. (2010).

We apply color correction to good photometry measurements between 3  $\mu\text{m}$  and 100  $\mu\text{m}$ . Moór et al. (2006a) had computed the color corrected fluxes for the *IRAS* points. For other points that fall within the wavelength coverage of the IRS spectrum, we use the shape of the IRS spectrum to determine the correction factors. The other photometry points are corrected based on the best estimated local SED shape. Color-corrected fluxes and references used to compute the correction factors are listed in Table 2.2. We do not consider correcting the 870  $\mu\text{m}$  point since it is on the Rayleigh-Jeans tail so the correction factor should be close to unity. If a point is color-corrected, the corrected flux is used in the following modeling and analysis. Fig. 2.2 shows the SED (with the color-corrected fluxes). The SED shows a single hump infrared excess with the flux peaking around 70  $\mu\text{m}$ . The system has  $L_{\text{IR}}/L_* \sim 2 \times 10^{-3}$ .

The *Spitzer* IRS data were obtained and analyzed by Chen et al. (2014). It is generally presumed that the *MIPS* fluxes will have a lower absolute calibration uncertainty. Therefore, Chen et al. (2014) calibrated the IRS spectrum by tabulating the synthetic *MIPS* flux and comparing it to the measured *MIPS* flux. They presumed that the source did not vary with time and then scaled the IRS spectrum to match the *MIPS* 24  $\mu\text{m}$  flux. More details of the spectral extraction and calibration can be found in Chen et al. (2014). The calibrated IRS spectra do not show any obvious solid state emission or absorption features, suggesting HD 131835 is not a system rich in small silicate grains and polycyclic aromatic hydrocarbons. For the following analysis, we treat each point of the spectra as a single measurement that is directly comparable to photometry measurements. When including images in the fit, each pixel is considered as a data point and is treated equally as a point on the SED. For each image, only the central 68 by 68 pixels ( $\sim 6''$  by  $6''$ ) are considered in the fit. There are total

of 9595 data points in which 10 points come from broadband photometry, 337 points come from the IRS spectrum, and 9248 points from the images.

### 2.4.1 Stellar Properties

The measured flux of the system includes the contribution from the star and from the disk. The star has  $T_{eff} = 8770$  K,  $\log g = 4.0$  and solar metallicity with  $A(V) = 0.187$  mag (Chen et al., 2012a). We use the IDL Astrolib routine `ccm_unred.pro`, which is based on Cardelli et al. (1989a), to apply reddening to the Kurucz (1993a) stellar atmosphere model. Since the disk emission is prominent in longer wavelengths, only the measurements with wavelength shorter than  $5.8 \mu\text{m}$  are used to fit for the stellar flux to characterize the stellar contribution. We compare the *Hipparcos* and 2MASS photometry to the synthetic fluxes of the model during the fitting process. The best fit is shown in Fig. 2.2. The stellar fluxes at  $11.7 \mu\text{m}$  and  $18.3 \mu\text{m}$  of this best-fit model were used to scale the PSFs during the PSF subtraction process described in § 2.3.3.

We parameterize a scaling factor as  $\xi \equiv (R_*/d)^2$  so that we can write

$$L_* = 4\pi d^2 \xi \sigma T^4 = 4\pi d^2 \int_0^\infty I_\nu d\nu. \quad (2.1)$$

By integrating the unreddened stellar component of the best-fit SED model and solving the equation, we obtain  $\xi = 6.68 \times 10^{-20}$ . When estimating the luminosity, the largest uncertainty comes from the distance measurement. Taking the distance to be  $122.7 \pm_{12.8}^{16.2}$  pc (van Leeuwen, 2007a), we find  $R_* = 1.41 \pm_{0.15}^{0.19} R_\odot$  and  $L_* = 10.5 \pm_{2.2}^{2.8} L_\odot$ .

### 2.4.2 Model

Our goal is to find a disk model that can reproduce the observed SED and the images simultaneously. The SED sets strong constraints on the grain temperature distribution, where as the images inform the spatial distribution of the grains. We aim to recover the extended mid-IR emission, with the disk flux peaking close to the center of the system,

while simultaneously reproducing the broad IR excess hump on the SED. With the space and temperature distributions of the grains so constrained, we hope to further characterize the grain properties such as its size and composition. In our model, we assume the disk to be optically thin since its  $L_{\text{IR}}/L_* \sim 2 \times 10^{-3}$ . To search for a model that accounts for the extended emission, we start with a simple two-dimensional continuous disk composed of only a single population of grains, then consider more complicated distributions.

#### 2.4.2.1 A Continuous Power-law Disk Model

In contrast to perfect blackbodies, dust grains do not couple efficiently to radiation when the wavelength is much larger than the grain size. We consider a simple parameterization of the emissivity with a modified blackbody function, whereby the emissivity varies with the frequency as a power-law with a positive index  $\beta$ . The grain temperature  $T_g$  at a distance  $r$  away from the star is found by balancing the energy intake and the energy output:

$$\frac{d^2}{r^2} \int F_{\nu,*} \nu^\beta d\nu = 4\pi \int B_\nu[T_g(r)] \nu^\beta d\nu \quad (2.2)$$

$B_\nu(T)$  here is the blackbody function. The grains are distributed with the surface density of  $n_0 (r/1\text{au})^\Gamma$ , with  $n_0$  being the two dimensional number density of the grains at 1 au. The density law applies to the region between the inner disk radius  $r_i$  and the outer radius  $r_o$ ; it is zero elsewhere. The total disk flux  $F_{\nu,\text{disk}}$  is

$$F_{\nu,\text{disk}} = C \int_{r_i}^{r_o} B_\nu[T_g(r)] \left(\frac{\nu}{1 \text{ Hz}}\right)^\beta \left(\frac{r}{1 \text{ au}}\right)^{\Gamma+1} dr \quad (2.3)$$

$C$  is the scaling factor such that  $C = 2\pi^2 n_0 a_0^2 (1\text{au}) d^{-2}$ . The characteristic grain radius is denoted as  $a_0$ .

There are seven free parameters total in this model. Five of which are needed to calculate the total disk flux:  $\beta$ ,  $\Gamma$ ,  $C$ ,  $r_i$ , and  $r_o$ . Two additional parameters, inclination  $i$  and position angle  $\phi$ , are needed to generate model images. We took several steps to initialize the starting parameters for the fit. First, we set  $\beta$  to zero as if the emission came from perfect blackbodies.

Then, we set  $r_i$  and  $r_o$  to a range of a few pixels to several hundred au. Afterwards, values for  $\Gamma$  and  $C$  were obtained by fitting the model to the SED data only. Finally,  $i$  and  $\phi$  were initialized to the best-fit inclination and position angle when fitting a ring to the images only. Once the parameters are initialized, we used a Levenberg-Marquardt least-squares fitter. The fitting process tends to drive  $r_o$  to unbounded values. The reason that  $r_o$  tends to drift to unbounded values is due to the model's under-prediction of the flux beyond  $35 \mu\text{m}$ . During the fitting process, after the model settles with the parameters that fit the majority of the data, the model will try to extend  $r_o$  to an arbitrary large value so that it will contain slightly more cold dust. The contribution from this cold dust does make the SED fit better but the amount is negligible. Thus, we fix  $r_o$  to 400 au where beyond which the image fit does not get better. The best-fit parameters along with the total chi-square ( $\chi^2$ ) and the reduced chi-square ( $\chi_\nu^2$ ) are listed in Table 2.3. The contributions to the total chi-square from the broad band photometry, IRS spectrum, and images are 3%, 31%, and 66%.

This one-component model does not produce a good fit. The modeled flux is too concentrated in the central region of the disk as the residual images show strongly negative values in center due to over subtraction. As a result, the best-fit  $i$  and  $\phi$  are not trustworthy. In addition, modeled SED under predicts the flux shorter than  $16 \mu\text{m}$  and beyond  $33 \mu\text{m}$ . The drive to better fit the short-wavelength part of the SED is inconsistent with the spatial location of flux in the images. This suggests that the power-law spatial distribution is inconsistent with the resolved outer disk flux and the contribution to the warm SED flux. Since this model clearly does not fit the data, we did not investigate further for estimating the uncertainties of the best-fit parameters. This inconsistency could be potentially resolved by considering a multi-component model. We therefore move on to a more sophisticated disk model by adding a second component.

Table 2.3. One-, Two-, and Three-population Model Fits

	Parameter	Model I	Model II	Model III	Unit
	$\chi^2$	9920	6255	5958	
	$\chi^2_\nu$	1.03	0.65	0.62	
Continuous Component	$\beta$	0.76	$1.53^{+0.02}_{-0.01}$	$1.64 \pm 0.02$	
	$C$	$3.7 \times 10^{-31}$	$(5 \pm 1) \times 10^{-42}$	$(9 \pm 2) \times 10^{-44}$	[au <sup>-1</sup> ]
	$\Gamma$	1.0	$0.48 \pm 0.05$	$0.53^{+0.06}_{-0.07}$	
	$i$	49	$73.8 \pm 1.0$	$74.5^{+0.9}_{-1.0}$	[deg]
	$\phi$	74	$62.0^{+1.0}_{-1.1}$	$61.2^{+1.0}_{-0.9}$	[deg]
	$r_i$	0.24	$37 \pm 3$	$35 \pm 3$	[au]
	$r_o$	400	400	$310^{+30}_{-20}$	[au]
Ring Component 1	$\beta$		$0.27^{+0.05}_{-0.04}$	$0.59 \pm 0.02$	
	$C_r$		$(7.4 \pm 1.5) \times 10^{-15}$	$(5.9^{+0.8}_{-0.7}) \times 10^{-16}$	
	$r$		$61^{+8}_{-6}$	$105 \pm 5$	[au]
Ring Component 2	$\beta$			$0.32 \pm 0.06$	
	$C_r$			$(4 \pm 1) \times 10^{-14}$	
	$r$			$220 \pm 40$	[au]

Note. — Model I is composed of a single continuous disk. Model II is composed of a continuous disk plus a ring. Model III is composed of a continuous disk plus two rings. The chi-square ( $\chi^2$ ) and the reduced chi-square ( $\chi^2_\nu$ ) are the minimum values estimated by least squares fitting. The one-component parameters are from the least squares fitting; uncertainties are not estimated since the model does not describe this system well at all. The two- and three-component model parameters and uncertainties are quoted from the marginal distributions of MCMC results. For the two-component model, the parameters (from top to bottom) correspond to the quoted least squares are ( $\beta, C, \Gamma, i, \phi, r_i, r_o, \beta, C_r, r$ ) = (1.53,  $5.0 \times 10^{-42}$ , 0.47, 74.0, 61.8, 37.5, 400, 0.27,  $7.2 \times 10^{-15}$ , 62) For the three-component model, the parameters correspond (from top to bottom) to the quoted least squares are ( $\beta, C, \Gamma, i, \phi, r_i, r_o, \beta, C_r, r, \beta, C_r, r$ ) = (1.64,  $1.1 \times 10^{-43}$ , 0.48, 74.3, 61.1, 36, 316, 0.59,  $6.2 \times 10^{-16}$ , 105, 0.33,  $4.3 \times 10^{-14}$ , 232).

### 2.4.2.2 A Continuous Power-law Disk + A Ring

This two grain populations model is composed of a continuous disk and a thin ring. The first component is as described in the section above. The second component assumes a single population of grains located in a narrow ring at a single radius  $r$  away from the star. We adopt the same emissivity law in the form of  $\nu^\beta$  for the ring component. However, this  $\beta$  parameter could have a different value than in the continuous component since the optical properties might be different for different grain populations. The flux from a ring model is:

$$F_{\nu,ring}(r) = C_r B_\nu[T_g(r)] \left( \frac{\nu}{1 \text{ Hz}} \right)^\beta \quad (2.4)$$

The grain temperature  $T_g$  is found by solving the Equation 2.2, and  $C_r$  is a scaling factor for the ring model. There are five parameters in the ring component:  $\beta$ ,  $C_r$ ,  $i$ ,  $\phi$ , and  $r$ . Limited by the image resolution, we make the continuous disk and the ring sharing the same  $i$  and  $\phi$ . Here, we again fix  $r_o$  to 400 au where beyond which the image fit does not get better and the SED fit does not show any significant improvement. We first use least squares fitting to find the best-fit model parameters. This model is a much better fit comparing to the previous single continuous disk model. The total  $\chi^2$  decreases by more than 3000. The contributions to the total chi-square from the broad band photometry, IRS spectrum, and images are 3%, 14%, and 83%. The image fit improves significantly. The residual images do not suffer from the severe over subtraction in the central regions anymore. Therefore, it is worth exploring the uncertainties of the fitting parameters for this model. However, the covariance matrix from the least squares fitting does not always provide reasonable error estimations, especially for parameters that are degenerate. Degeneracies are prominent between  $\beta$ ,  $\Gamma$ ,  $C$ , and  $r_i$  for the continuous disk model and between  $\beta$ ,  $C_r$ , and  $r$  for the ring model. For example, effects of temperature depression from increasing  $r$  can be compensated by having a larger value of  $\beta$ . To better quantify the uncertainties on the parameters, we use the ensemble MCMC method of Goodman & Weare (2010a), as implemented in the `emcee` python package (Foreman-Mackey et al., 2013a).

The `emcee` package is based on the Markov chain Monte-Carlo (MCMC) method de-

veloped by Goodman & Weare (2010a) where they utilize multiple "walkers" to propagate multiple chains simultaneously. We set the initial positions of the walkers by drawing random numbers based on Gaussian distributions with means equal to the best-fit parameters and the variances equal to 10% of the means. This MCMC algorithm adjusts the candidate step proposal distribution based on the walkers' current positions in the parameter space. We use 100 walkers and run for few thousand steps after the burn-in period seems to be over. All of the marginalized probability density functions (PDFs) look fairly symmetric. We calculate the uncertainty on each parameter by measuring the  $1\sigma$  interval on the marginalized PDFs, with the upper and lower bounds measured separately. The parameter values and their uncertainties are listed in Table 2.3.

The best fit shows that the continuous component contains hotter grains and is mainly contributing to the  $11.7 \mu\text{m}$  emission while the ring component contains cooler grains and dominates the  $18.3 \mu\text{m}$  emission. The hot continuous disk extends from a few tens of au to hundreds of au and contains grains as hot as 300 K. The cool ring locates around 60 au, spatially overlapping with the continuous component. By comparing to the single-disk model, this two grain populations model significantly improved the fit to the images and to the short wavelength part of the SED. However, this model is still under predicting the flux longer than  $35 \mu\text{m}$  on the SED. The main reason for causing this underprediction is the outnumbered IRS spectral data points. The fit is driven by closely matching the spectrum in order to effectively lower the  $\chi^2$ . As a result, the model completely misses the photometry points at wavelengths longer than  $35 \mu\text{m}$ . As a test, we considered excluding long wavelength IRS points. We find that in order to produce a reasonably good fit with this two-component model, we have to cut out IRS points longer than  $\sim 15 \mu\text{m}$ . Since we do not have a physical explanation to place such cut, we include all IRS points in our analysis. To account for the long wavelength emissions, we add another ring component in the following section.

### 2.4.2.3 A Continuous Power-law Disk + Two Rings

This three grain populations model is composed of a continuous disk and two thin rings. The structures of these model components are described in the previous two sections. Although the inclination and the disk position angle are free parameters in the model, we constrain the three components to share the same values. As before, we use the least squares fitting to find the best-fit model parameters and MCMC to quantify their uncertainties. The model parameters are listed in Table 2.3. The contributions to the total chi-square from the broad band photometry, IRS spectrum, and images are 2%, 12%, and 86%. Fig. 2.3 and Fig. 2.4 show the best-fit SED model and the image models respectively.

This best-fit model is composed of a hot continuous power-law disk extended from  $35 \pm 3$  au to  $310_{-20}^{+30}$  au with temperature ranging from 330 K to 150 K, a warm ring with temperature of 97 K located at  $105 \pm 5$  au and the cold ring with temperature of 52 K located at  $220 \pm 40$  au. The middle panel of Fig. 2.4 shows the PSF convolved model disk in the two imaging wavelengths. Approximately 90% of the flux in the  $11.7 \mu\text{m}$  model comes from the hot continuous component while 10% comes from the warm ring. At  $18.3 \mu\text{m}$ , about 2/3 of the flux comes from the warm ring and 1/3 of the flux comes from the hot disk. This model provides a reasonable fit to the images, despite there are some small patches of over-subtraction and under-subtraction as seen from the image residuals (the bottom panel in Fig. 2.4). We characterize the variations in the resolution-element scales by dividing the sum of the smoothed residual flux values in a resolution-element-sized area by the sum of the corresponding smoothed noise. The variations in the resolution-element scales are within  $1 \sigma$ , suggesting the model fits the images reasonably well. The cold ring component is too faint to affect either imaging channel. However, this cold ring is essential for contributing to the long wavelength part of the SED and is a key reason why we can constrain  $r_o$ , unlike the previous two models. We found that this three-component model is able to provide a sensible fit to the SED and the images simultaneously.

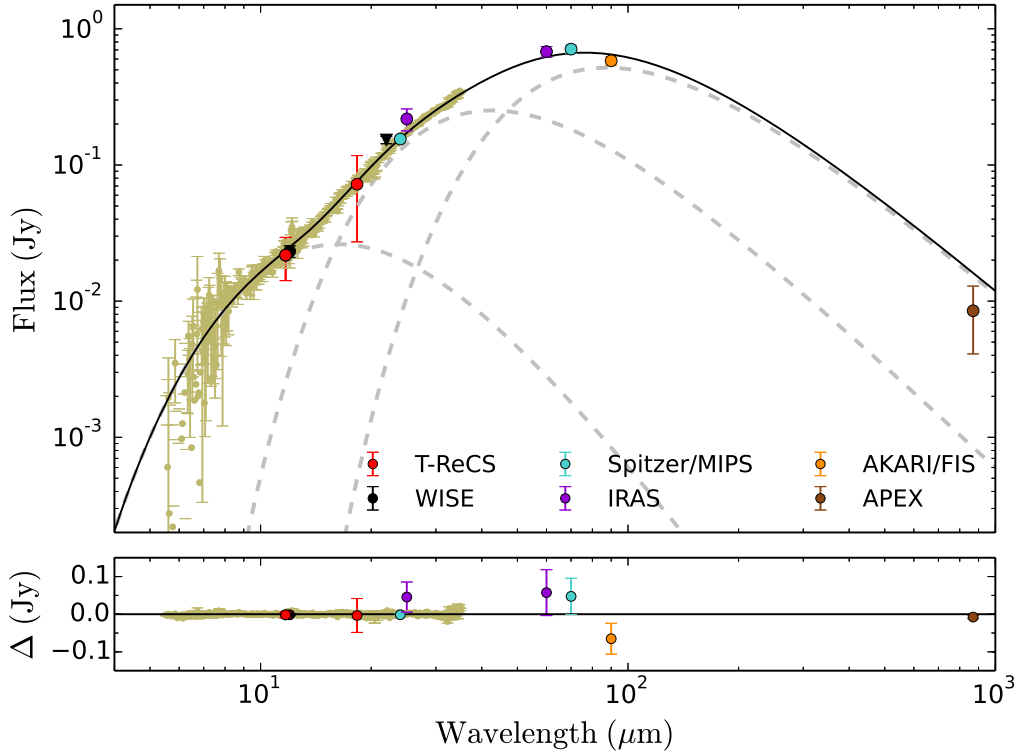


Figure 2.3 SED of the debris disk around HD 131835 with the best-fit three-population model (solid line) and its components (dashed lines). The residuals are plotted in the bottom panel. This model is composed of a hot continuous power-law disk, a warm ring, and a cold ring. The grains are assumed to emit like modified blackbodies such that the emissivity is proportional to  $\nu^\beta$ . The best-fit parameters are listed in Table 2.3. Given this grain emissivity law, this three-component model is the simplest model that provides a reasonable fit to the SED while fitting the images simultaneously.

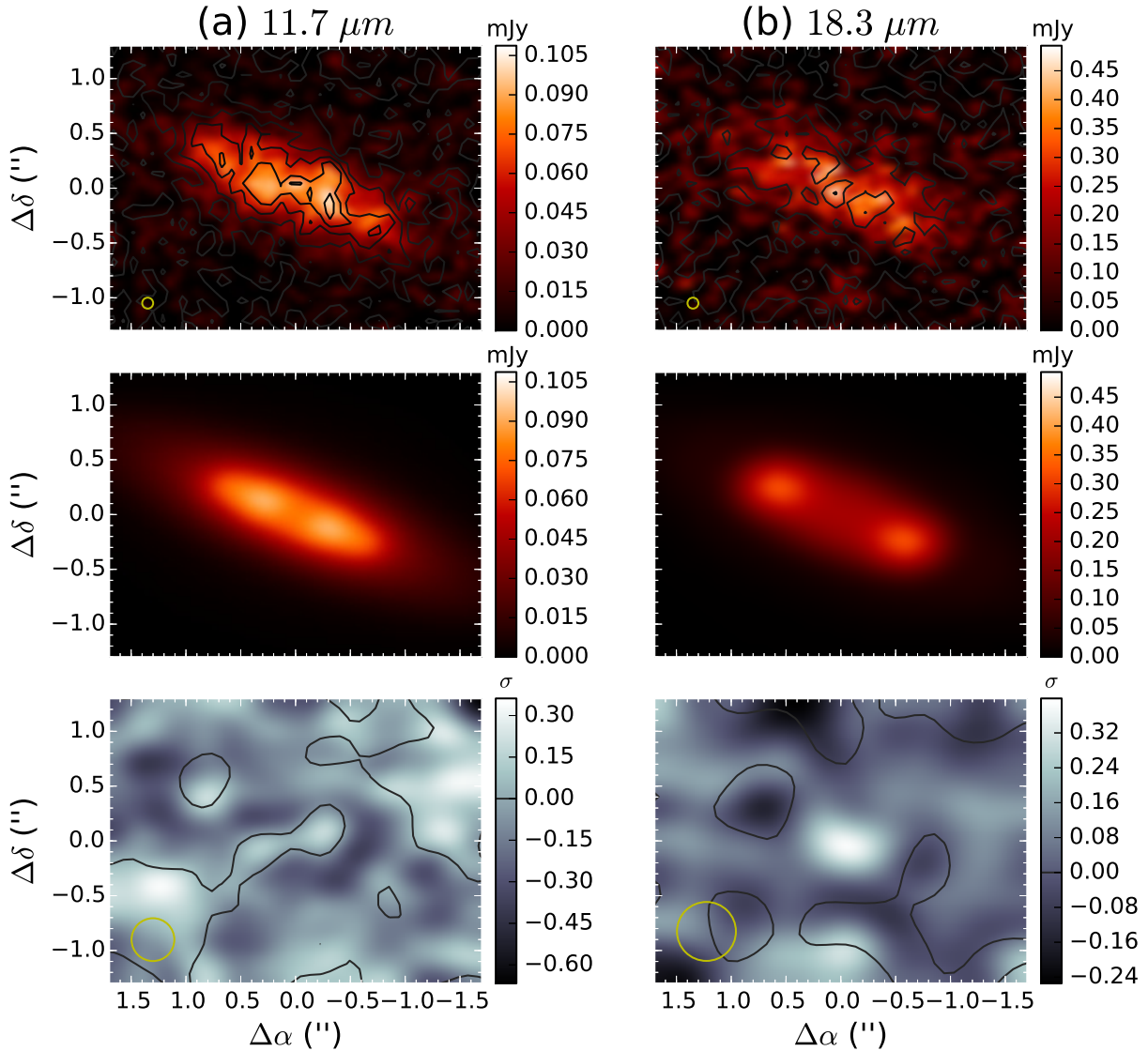


Figure 2.4 Images showing the best fit of the three-component model (a continuous power-law disk + two rings). Top panel: the PSF subtracted images, smoothed to suppress high-spatial-frequency noise for the displaying purpose. We smoothed the images with a gaussian with its FWHM (yellow circle) equals to  $0.1''$ . Contours are spaced by the  $1\text{-}\sigma$  background noise level derived from the smoothed variance map. Middle panel: the best-fit model convolved with the stellar PSF. Bottom panel: the smoothed residual flux divided by the uncertainty derived from the smoothed variance map. Images are smoothed with gaussians with FWHM equal to their PSF sizes only for the displaying purpose. Comparing large spatial structures in the residual images, this model seems to slightly under predict the central flux. Nonetheless, the variations in the resolution-element scale are within  $1\sigma$ , suggesting the model fits the images reasonably well. The best-fit parameters are listed in Table 2.3.

#### 2.4.2.4 Other Disk Models

We also tried fitting the data with a broken-power-law disk model. This model is composed of one continuous-disk described by two power-law grain distributions: one between the inner radius and the intermediate radius and the other between the intermediate radius and the outer radius. The entire disk shares a single value of emissivity power index  $\beta$ , in which we assume the grain composition is the same across the disk. The best-fit result improves slightly compared to the one from a single continuous disk model described by only one power-law grain distribution (§ 2.4.2.1). However, this best-fit broken-power-law model suffers from the similar inconsistency as the single-power-law model where the model flux is too concentrated in the center of the disk in both bands. The reason lies under the assumption of a single grain population. Since the temperature of the entire disk is governed by a single emissivity power index, grains further away will have lower temperatures. Thus, although a steeply rising density power-law can make the model disk flux more extended, it will also drive the corresponding SED model too bright at longer wavelengths since the flux is originated from low-temperature grains. In order to have warm dust grains be responsible for the extended emission instead, we must introduce a second emissivity power index to our model (as used in § 2.4.2.2).

Another model we tried is composed of two continuous disks. We found that the two components can share the same values for  $\Gamma$ ,  $r_i$ ,  $r_o$ ,  $i$ , and  $\phi$  while still producing a good fit compared to having two independent sets of parameters. However, this model is very sensitive to the  $\beta$  values. A small adjustment in  $\beta$  will introduce a significant deviation in the resulting model. Thus, we must keep the two  $\beta$  parameters independent in order to maintain a good fit. This result again indicates there are more than one population of grains in the system. We notice that one of the continuous components can be simplified into a ring without changing the best-fit result significantly ( $\chi^2_\nu$  changes from 0.65 to 0.64). Therefore, we performed the detailed analysis of a continuous power-law disk plus a ring model (§ 2.4.2.2) instead of the two-continuous component model.

## 2.5 DISCUSSION

Our models support the inference of multi-spatial components from a multi-temperature SED. Recently, Kennedy & Wyatt (2014) argued that if the SED of a debris disk around an A-type star shows multiple temperature components, it is an indication that the system hosts multiple populations of grains in different locations. Our SED modeling of the disk around HD 131835 indicates there are multiple temperatures. From modeling with the resolved images in mid-infrared, we confirm the system indeed have grains at multiple spatial locations: a hot continuous component extends from  $35 \pm 3$  to  $310_{-20}^{+30}$  au, a warm ring located at  $105 \pm 5$  au, and a cold ring located at  $220 \pm 40$  au. Our model indicates the two separated narrow rings are embedded in an extended disk component. Although not all the model components are completely spatially separated, we are confident that the dust is not concentrated in a single belt. Our modeling result agrees with the argument made by Kennedy & Wyatt (2014), adding to the small poll of high resolution observations confirmed cases.

Grains with effective temperatures hotter than blackbodies are responsible for the observed disk emission, since perfect blackbody grains at these spatial locations would not have the appropriate color temperatures. In our models, the grains are assumed to emit according to a modified blackbody function where the emissivity is proportional to  $\nu^\beta$ . In the case of the three-population model, the grains in the  $\beta$  values for the continuous component, the warm ring, and the cold ring are  $1.64 \pm 0.02$ ,  $0.59 \pm 0.02$ , and  $0.32 \pm 0.06$  respectively.  $\beta = 0$  corresponds to blackbody grains. The positive  $\beta$  values indicate the grains are small since they are inefficient in absorbing and emitting at long wavelengths, and  $\beta = 1$  corresponds to small grains in the limit  $2\pi a \ll \lambda$ , where  $a$  is the grain size and  $\lambda$  is the observed wavelength. For  $\beta > 1$ , real materials with complicated emissivities are required to explain the observations. Observational evidence points that it is common for debris disks around A-stars to have  $\beta$  values approximately within 2 (Booth et al., 2013), and our results fall within this region.

We searched for the potential grain compositions by first examining the equilibrium grain

temperatures with our modified blackbody models and then compare them to the equilibrium temperatures of specific grain compositions. Using the model parameter  $r$  and  $\beta$ , we plotted the corresponding equilibrium temperatures at different stellar locations in Fig. 2.5. Our goal is to use these temperature curves to identify the possible grain compositions. We consider some common compositions such as graphite, astro-silicate, and ice. We use the optical constants of graphite and silicate from Draine & Lee (1984a) and Laor & Draine (1993). The optical property of ice is a function of its temperature due to varying crystal structures. Warren (1984) provided the index of refraction of pure ice at  $-1^\circ\text{C}$ ,  $-5^\circ\text{C}$ ,  $-20^\circ\text{C}$ , and  $-60^\circ\text{C}$ . Although the optical properties are different at different crystal temperatures, the variation is quite small. Thus, to first order, we adopt the optical constants of ice assuming the ice preserves the similar crystal structure as when it is at  $T = -60^\circ\text{C}$ . We calculated their equilibrium temperatures using the Mie theory (Bohren & Huffman, 1983) with the assumption that grains are spherical. The grain size contours are overplotted on the temperature-stellocentric distance map on Fig. 2.5.

Grains composed solely of graphite, astro-silicate, or ice in the equilibrium temperature can not be used to explain all the observed disk properties. Among the three compositions, graphite grains have the highest temperature, and ice grains are the coolest. We have also considered using the other types of silicates such as olivine and pyroxene. However, their optical properties are similar to the astro-silicate, and thus, the grain temperatures are on the same order of magnitude as the astro-silicate grains. The warm and cold rings could be made up by graphite and silicate grains closer to micron size. On the other hand, the hot continuous disk component would require the emitters to be really small. Since small grains become inefficient emitters at long wavelengths, these grains will sustain much higher temperatures than a blackbody. However, even though nanometer-sized graphite grains are significantly hotter than blackbodies, they still could not match the temperature of the hot continuous disk. In addition, grains this small are not likely to be present in the system as discussed below.

We have qualitatively considered having porous grains and using a broken emissivity power-law in attempt to address the abnormally warm dust. However, neither considera-

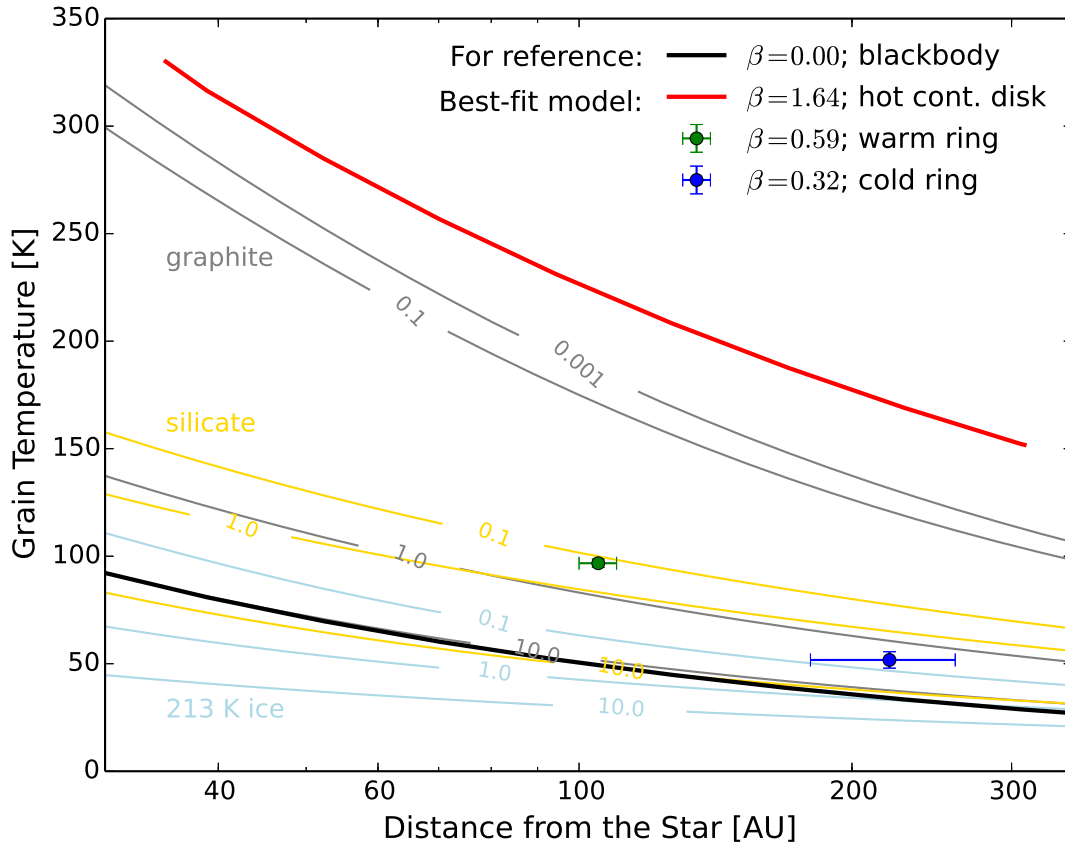


Figure 2.5 Equilibrium temperatures of the disk model components in comparison to various grain types. The temperatures and radii for the three-component model are shown here. The red curve represents the hot continuous disk component. The green and blue dots represent the warm and cold ring components respectively. The black line is the temperature curve assuming grains are perfect blackbodies. Note that all three populations of grains have equilibrium temperatures higher than the temperature of a hypothetical blackbody that would generate the same flux. This grain property is commonly observed since small grains are inefficient in emitting at long wavelengths. The grain size (grain radii in  $\mu\text{m}$ ) contours for graphite, silicate, and ice are overplotted here for comparison. Although the optical property of ice changes with temperature, we do not take it into account since the variation is quite small; here we use the  $T = 213$  K ice crystal structure. Although small graphite grains, as expected, are significantly hotter than other grains, it still can not match the temperature gradient for the hot continuous disk component. Thus, grains composed solely of graphite, astro-silicate, or ice in the equilibrium temperature can not be used to explain all the observed disk properties.

tions are in our favor. Porous dust grains have lower temperatures than compact spheres (Kirchschlager & Wolf, 2013). Thus, introducing porosity will make the discrepancy worse for finding a physical grain composition for the observed dust temperatures. Similar qualitative result applies for using a broken emissivity power-law case. A broken emissivity power-law assumes that the emissivity is 1 when  $\nu > \nu_c$  and  $(\nu_c/\nu)^\beta$  when  $\nu < \nu_c$ , where  $\nu_c$  is a free parameter indicating the critical frequency at which the emissivity function changes. Compared to the smooth emissivity law we used, the grains with the broken emissivity power-law are less efficient in absorbing the stellar light. Therefore, grains with a broken emissivity power-law will sustain lower temperatures. In addition to making the grains cooler, a broken emissivity power-law introduces an additional model parameter,  $\nu_c$ , that makes the model more complex than a smooth emissivity power-law.

Although the high disk-temperature draws the connection to small grains, no features of small grains are detected in the system. Nanometer-sized grains are in the molecular region. For HD 131835, we do not observe any solid-state features in the 10 and 20 micron regions from the IRS spectrum, which indicates that the grains are probably larger and more likely to be in the micrometer size region (e.g., Draine & Lee 1984a). Stochastically heating small grains such as polycyclic aromatic hydrocarbons (PAHs) could be one way to make grains have much higher temperatures than in the equilibrium states (Draine & Li, 2001). However, the IRS spectrum does not show the spectral signatures of PAHs either.

Furthermore, small grains are unlikely to present in the system when considering the radiation pressure from the star. The blowout grain size is calculated by balancing the radiation pressure with the gravity. Taking the mass of the star to be  $1.9 M_\odot$  (Chen et al., 2012a) and using the grain density of  $\rho = 3.5 \text{ g/cm}^3$ , we get the blowout grain radius for HD 131835 to be:

$$a_{blowout} = 0.91 \mu\text{m} \left( \frac{L_*}{10.5 L_\odot} \right) \left( \frac{1.9 M_\odot}{M_*} \right) \left( \frac{3.5 \text{ g/cm}^3}{\rho} \right). \quad (2.5)$$

Grains smaller than this blowout size are unlikely to survive in the system. Although small grains can be trapped in resonance due to gas drag while migrating, the effect is unlikely to

be significant with the gas level present in this system. Since small grains are unlikely to be responsible for the hot continuous disk emission, the nature of these abnormally warm grains is not completely understood.

Identifying unique disk models around A stars can be challenging. For example, recently, with *Herschel* observations in 70, 100, and 160  $\mu\text{m}$ , Booth et al. (2013) shows that the disks around A stars have various morphologies, ranging from systems that can be fit with just a narrow ring to the ones that require wider or multiple rings. Although direct images can provide constraints on grain size distribution and dust properties, sometimes finding a proper model can be quite difficult. For example, a detailed modeling work on  $\beta$  Leo debris disc with multi-wavelength observations shows the degeneracy between one, two, and three components models (Churcher et al., 2011). For HD 131835, the three-component model gives a reasonable fit but more data are needed to set better constraints. We would like to better characterize the grain properties, understand the distribution of grains, and constrain the location of planetesimal belts in much greater detail.

Fortunately, with the new generations of high resolution, high sensitivity, and high contrast instruments, detailed disk characterization is foreseeable. HD 131835 is located in the Southern sky, making it a favorable target for GPI (Gemini Planet Imager), SPHERE (Spectro-Polarimetric High-contrast Exoplanet Research), and ALMA (Atacama Large Millimeter/submillimeter Array). GPI and SPHERE can potentially image the disk in scattered light in the near infrared, providing the currently uncharacterized scattering properties of the dust grains around HD 131835, in both total intensity and linearly polarized light. Designed specifically for high contrast imaging, these instruments have the potential to probe dust-scattered light at small inner working angles (e.g., Perrin et al. 2014b). With superior sensitivity and resolution, ALMA is capable for detailed mapping of the CO gas in this system. In addition, ALMA observations would trace the distribution of larger grains which are more tightly coupled to the locations of the large parent bodies. Future observations with these facilities hold great promise in further characterizing the dust distribution and dynamics.

## 2.6 SUMMARY

HD 131835 shows strong infrared excess, and here we present the discovery of the resolved debris disk in the mid-infrared. The debris disk's properties can be constrained using all the available observations on HD 131835, including 15 photometry points, the IRS spectrum, and resolved images at  $11.7 \mu\text{m}$  and  $18.3 \mu\text{m}$ . From our modeling result, the disk clearly can not be described by a single continuous population of modified blackbody grains. The images alone can be described by a two grain population model which is composed of a continuous power-law disk and a ring. The continuous component contains hotter grains and dominates the emission in the  $11.7 \mu\text{m}$  image whereas the ring component contains cooler grains and dominates the emission at  $18.3 \mu\text{m}$  image. However, in order to obtain a good fit to the SED simultaneously, an additional ring component is needed. This three-component model is composed of a hot continuous power-law disk, a warm ring, and a cold ring. In this model, the disk fluxes in the imaged wavelengths are contributed primarily from the hot continuous disk and the warm ring. Since the cold ring peaks at a longer wavelength, this third component does not show up in the mid-infrared images so its spatial location is relatively unconstrained. The excess emission in far infrared and submillimeter, however, can be well described by this third component. Starting with the simplest model, we found that a model with three components and therefore three grain populations can well describe the images and the SED simultaneously.

## 2.7 ACKNOWLEDGEMENTS

Work by L.-W. Hung is supported by the National Science Foundation Graduate Research Fellowship number 2011116466 under Grant number DGE-1144087. P. G. Kalas and J. R. Graham thank support from NASA NNX11AD21G, NSF AST-0909188, and University of California LFRP-118057.

## CHAPTER 3

# First Scattered-light Image of the Debris Disk around HD 131835 with the Gemini Planet Imager

Reproduced by permission of American Astronomical Society journals  
(Hung, L.-W., Duchêne, G., Arriaga, P., et al. 2015, ApJL, 815, L14)

### 3.1 INTRODUCTION

Debris disks are the remnant products of planet formation processes; within them, planetesimals collisionally evolve to generate dust disks that are visible in thermal emission and scattered-light. The Gemini Planet Imager (GPI; Macintosh et al. 2014) is one of the first high-contrast instruments equipped with the extreme adaptive optics (AO) that is specially designed for direct imaging and spectroscopy of exoplanets and debris disks. By resolving a debris disk, we can characterize the spatial distribution of dust grains, infer its dynamical history, and deduce the presence of unseen planets (see Wyatt 2008 for a review). Unlike most debris disks which are gas-depleted, carbon monoxide is detected in the HD 131835 system (Moór et al., 2015). Being a rare resolved debris disk with detected gas, HD 131835 serves as a unique target for studying the relationship between gas-dust physics and planetary science.

HD 131835 is an A2IV star (Houk, 1982) in the Upper Centaurus Lupus (UCL) moving group (Rizzuto et al., 2011b), a subgroup of the Sco-Cen association. HD 131835 is  $\sim 15$  Myr old (Mamajek et al., 2002b; Pecaute et al., 2012b), at a distance of  $123^{+16}_{-13}$  pc (van Leeuwen, 2007b). Its IR emission was discovered by the *Infrared Astronomical Satellite* (Moór et al., 2006b). Chen et al. (2012b) presented MIPS observations and showed that it is one of only four UCL/Lower Centaurus Crux A-type stars with  $L_{IR}/L_* > 10^{-3}$ , comparable to  $\beta$  Pic.

Recently, Hung et al. (2015a) resolved the debris disk around HD 131835 at 11.7 and 18.3  $\mu\text{m}$  using Gemini/T-ReCS. A three-component dust disk model, composed of an unusually warm continuous disk and two rings, was able to simultaneously explain the spectral energy distribution (SED) and the mid-IR thermal images. Compared to recent disk studies with GPI, such as HD 115600 (Currie et al., 2015) and HD 106906 (Kalas et al., 2015), HD 131835 is less inclined and the disk flux is more radially extended ( $\sim 35$  to  $\sim 400$  au), allowing us to better study its morphological features. Here we report the first scattered-light detection of dust surrounding HD 131835 in polarized light with GPI.

## 3.2 OBSERVATIONS AND DATA REDUCTION

### 3.2.1 Observations

We observed HD 131835 as one of our GPI Exoplanet Survey (GS-2015A-Q-500) campaign targets with GPI at the Gemini South Observatory, Cerro Pachon, Chile. On 2015 May 1, we obtained thirty-two 60 s exposures in the  $H$ -band polarimetry mode (Hinkley et al., 2009; Perrin et al., 2015), with waveplate angles of  $0^\circ$ ,  $22^\circ.5$ ,  $45^\circ$ , and  $67^\circ.5$ . On 2015 May 4, we obtained forty-one 60 s exposures in the  $H$ -band spectroscopic mode. The observations in both modes were taken with the coronagraph and with the total field rotation  $> 80^\circ$  at airmass  $\leq 1.014$ .

The GPI's field of view (FOV) is  $2''.7$  square, with a scale of  $14.166 \pm 0.007$  mas pixel $^{-1}$  (updated from Konopacky et al., 2014). The radius of the  $H$ -band focal plane mask (FPM) is  $0''.123$ . Because the star is behind the occulter in the coronagraphic mode, astrometric and photometric calibrations use satellite spots, which are diffracted starlight formed by a square pupil-plane grating (e.g., Sivaramakrishnan & Oppenheimer, 2006; Sivaramakrishnan et al., 2010; Wang et al., 2014).

### 3.2.2 Data Reduction

The data were reduced using the GPI Data Reduction Pipeline (DRP; Perrin et al. 2014a). Polarimetry data were dark subtracted, corrected for flexure (Draper et al., 2014), cleaned for correlated noise (Ingraham et al., 2014), interpolated over bad pixels in the two-dimensional (2D) detector image, and assembled into data “cubes” with the third dimension comprising the two orthogonal polarization states. To get the Stokes cube, the images were divided by a low spatial frequency, polarized flat field (Millar-Blanchaer et al., 2015), interpolated over bad pixels in the three-dimensional (3D) datacubes, mitigated for systematics between the two orthogonal polarization channels via double differencing, subtracted for the instrumental polarization within each data cube (Wiktorowicz et al., 2014) using the average polarization fraction measured within the FPM, rotated to align the image orientations, and combined using singular value decomposition matrix inversion.

The spectroscopic data were dark subtracted, flexure corrected, and wavelength calibrated (Wolff et al., 2014) with an  $H$ -band Ar arc lamp taken right before the science sequence, interpolated over bad pixels in 2D, assembled into a spectral data cube, interpolated over bad pixels in 3D, and corrected for distortion.

### 3.2.3 Photometric Calibration

We perform photometric calibration on the polarimetry data by considering the satellite spot to star flux ratio  $R$ , the stellar flux  $F_\star$  in physical units, and the average satellite spot flux  $S$  in analog-to-digital unit (ADU) per coadd. The calibrated image data  $D_f$  can be found using

$$D_f = D_i \frac{R F_\star}{S}, \quad (3.1)$$

where  $D_i$  is the image data in ADU coadd<sup>-1</sup>. In the GPI  $H$ -band,  $R \sim 2 \times 10^{-4}$  (Wang et al., 2014). We adopt  $F_\star = 965 \pm 35$  mJy as the  $H$ -band flux of HD 131835 from 2MASS (Cutri et al., 2003b). We use an elongated aperture, similar to the shape of a running track, to perform aperture photometry on the satellite spots in polarimetry mode. We obtain a conversion factor of  $1 \text{ ADU coadd}^{-1} \text{ s}^{-1} = (7.8 \pm 1.3) \times 10^{-4} \text{ mJy}$ , with the uncertainty

mostly stemming from measurement of  $S$ .

The photometric calibration in the spectral mode (Maire et al., 2014) is done using the Calibrated Datacube Extraction recipe<sup>1</sup> via the GPI DRP based on the same principle. However, instead of using the broadband  $F_\star$  and  $S$  fluxes in the above equation, we replace them with the host star spectrum and the average satellite spot spectrum. For the stellar spectrum, we use the IDL Astrolib routine `ccm_unred.pro` (based on Cardelli et al. 1989b) to apply  $A(V) = 0.187$  mag. reddening (Chen et al., 2012b) to the Kurucz (1993b) stellar atmosphere model with  $T_{eff} = 8770$  K,  $\log g = 4.0$ , and solar metallicity.

### 3.3 MORPHOLOGY OF THE SCATTERED-LIGHT DISK

We resolve the debris disk around HD 131835 through polarimetric differential imaging. Figure 3.1 shows the calibrated GPI  $H$ -band polarized intensity of HD 131835 in radial Stokes  $Q_r$  (Schmid et al., 2006). In the sign convention adopted here, positive  $Q_r$  shows the tangentially polarized intensity, while negative  $Q_r$  represents radially polarized intensity. The disk appears to be inclined, with scattered-light extending from  $\sim 75$ – $120$  au. By fitting the location of the flux peak along the major axis on each wing, we find no significant offset that is larger than 300 mas. If we assume an axisymmetric and radially smooth density structure, the projected eccentricity,  $e$ , along the major axis is consistent with zero, and  $e > 0.2$  is rejected at  $1\sigma$ . Due to the non-detection on the southeast (SE) quadrant, the eccentricity along the minor axis is left unconstrained. The data are limited by instrumental polarization within the central  $\sim 0''.3$  and by photon noise at larger radii.

Figure 3.1 shows brightness asymmetries along both the minor and major axes. The northwest (NW) side of the disk is significantly brighter than the SE side, which is undetected. This brightness asymmetry is likely due to light scattered in a preferential direction, as seen in the case of HR 4796A (Perrin et al., 2015). In addition, a weaker brightness asymmetry is present along the major axis. To quantify this brightness asymmetry, we use the best-fit geometric parameters found in §3.6 (except for setting the outer radius to be

---

<sup>1</sup>[http://docs.planetimager.org/pipeline/usage/tutorial\\_spectrophotometry.html](http://docs.planetimager.org/pipeline/usage/tutorial_spectrophotometry.html)

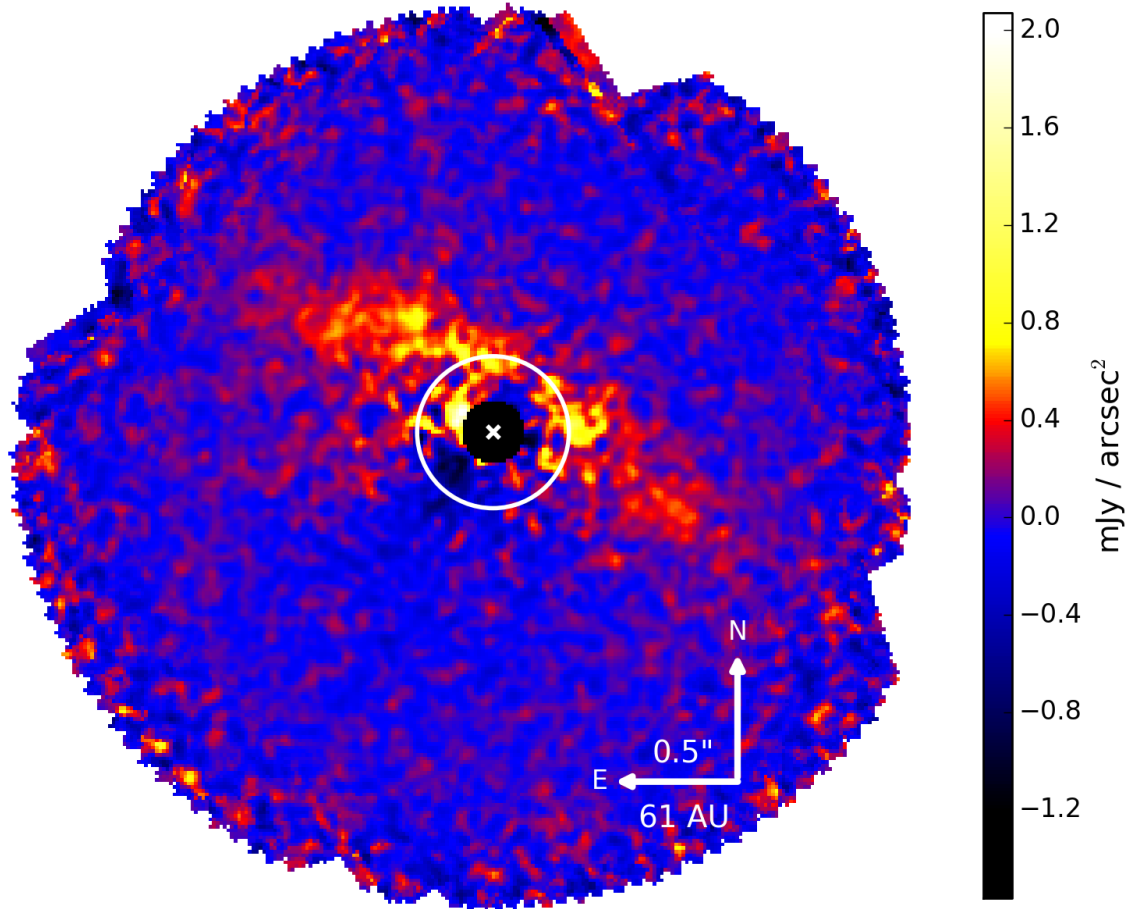


Figure 3.1 GPI detection of dust-scattered starlight around HD 131835 in the  $H$ -band tangentially polarized intensity. The image is smoothed by a three-pixel FWHM Gaussian ( $\sim$  the PSF size at  $1.6 \mu\text{m}$ ). The location of the star (white  $\times$ ) and the FPM (black circle) are marked. Residual instrumental polarization likely affects the region within the white circle. The stronger forward scattering makes the front (NW) side of the disk more apparent. A weaker brightness asymmetry is detected along the major axis, with the northeast side being 1.3 times brighter than the southwest side.

180 au due to the limited FOV) and consider the region exterior to  $0''.3$  on the NW side of the major axis. Since single scattering by circumstellar dust is expected to produce linearly polarized light only in the  $Q_r$  polarization states, we measure the noise using Stokes  $U_r$ , which corresponds to the linear polarization  $45^\circ$  from  $Q_r$ . The error at each angular separation in the  $Q_r$  image was estimated by measuring the standard deviation of the three-pixel wide annulus at the same separation in the Stokes  $U_r$  image. We find that the northeast (NE) side of the disk is  $1.30 \pm 0.09$  times brighter than the southwest (SW) side. In contrast, the thermal imaging shows that the sides are equally bright, with a 30% brightness asymmetry excluded at  $> 3\sigma$  (Hung et al., 2015a).

### 3.4 LIMITS ON DISK TOTAL INTENSITY

To subtract the stellar point-spread function PSF from the total intensity polarimetry and spectroscopic images, we used a Python implementation of the Karhunen–Loève Image Projection (KLIP) algorithm (Soummer et al., 2012; Pueyo et al., 2015), pyKLIP (Wang et al., 2015), to perform PSF subtraction using angular differential imaging (ADI; Marois et al., 2006). We divided the images into three annuli and four azimuthal subsections and ran KLIP over each zone, using an angular exclusion criterion of  $5^\circ$  to select reference images. We used the first five KL basis vectors to estimate the PSF for each subsection. These parameters were selected by optimizing the throughput of an injected model disk.

The disk is undetected in both Stokes  $I$  and spectral data. The non-detection could be a result of the faintness of the disk as well as severe ADI self-subtraction. Even with the total field rotation being  $> 80^\circ$ , the radially extended geometry of the moderately inclined disk makes it particularly susceptible to the latter effect. To get an upper limit on the total intensity, we inject increasingly brighter model disks (discussed in § 3.6) into the raw data and find when we can recover the disk after the PSF subtraction. The  $3\sigma$  upper limit on the peak total intensity in the polarimetry data is  $140 \text{ mJy arcsec}^{-2}$ , giving a lower limit of the peak polarization fraction of 1%. The spectral data give a less constraining upper limit. These upper limits are larger than the total intensity of the best-fit model discussed

in Section 3.6, thus demonstrating consistency between our empirical upper limits and our modeling.

### 3.5 LIMITS ON POINT SOURCES

We process our spectroscopic mode data to optimize planet detection. We first subtract the PSF for each wavelength channel using the TLOCI code (Marois et al., 2014), which assumes an input spectrum to optimize the subtraction while maximizing the signal-to-noise ratio (S/N) of an exoplanet of that specific spectral type. For our analysis, T8 and L8 spectra are chosen as the priors based on our experience in order to cover a wide range of DUSTY (Chabrier et al., 2000) and COND (Baraffe et al., 2003) exoplanets. The final data cube is then collapsed by a weighted mean, considering the input spectrum and the noise.

We searched for point sources with planet-like spectra but detected none. To estimate our upper limits, we derived the TLOCI contrast curves by measuring the standard deviation of the pixel noise in each annulus of  $\lambda/D$  width. These contrast curves are then transformed into exoplanet mass upper limits using the BT-settl models (Allard et al., 2012). In our polarimetry mode observation, we derive the point-source contrast curves by dividing the scatter (due to photon and read noise) at each annulus by the stellar flux, similar to how the contrast curves are derived in the spectroscopic mode. The contrast curves for the total and polarized intensities and mass limits derived from the spectral-mode observations are shown in Figure 3.2. We reject objects with  $M \gtrsim 3.5 M_J$  outside of  $0''.5$ .

### 3.6 MODELING THE SCATTERED-LIGHT DISK

We take a two-step approach to find a model that fits the SED and the GPI image. First, we use a geometric model to retrieve the structure of the scattered-light disk. Then, fixing the disk geometry, we search for a physical model that is built on the model proposed by Hung et al. (2015a) to get an estimate of the main dust properties associated with the polarized scattered-light detection. In both steps, we exclude the central region within  $0''.3$  due to

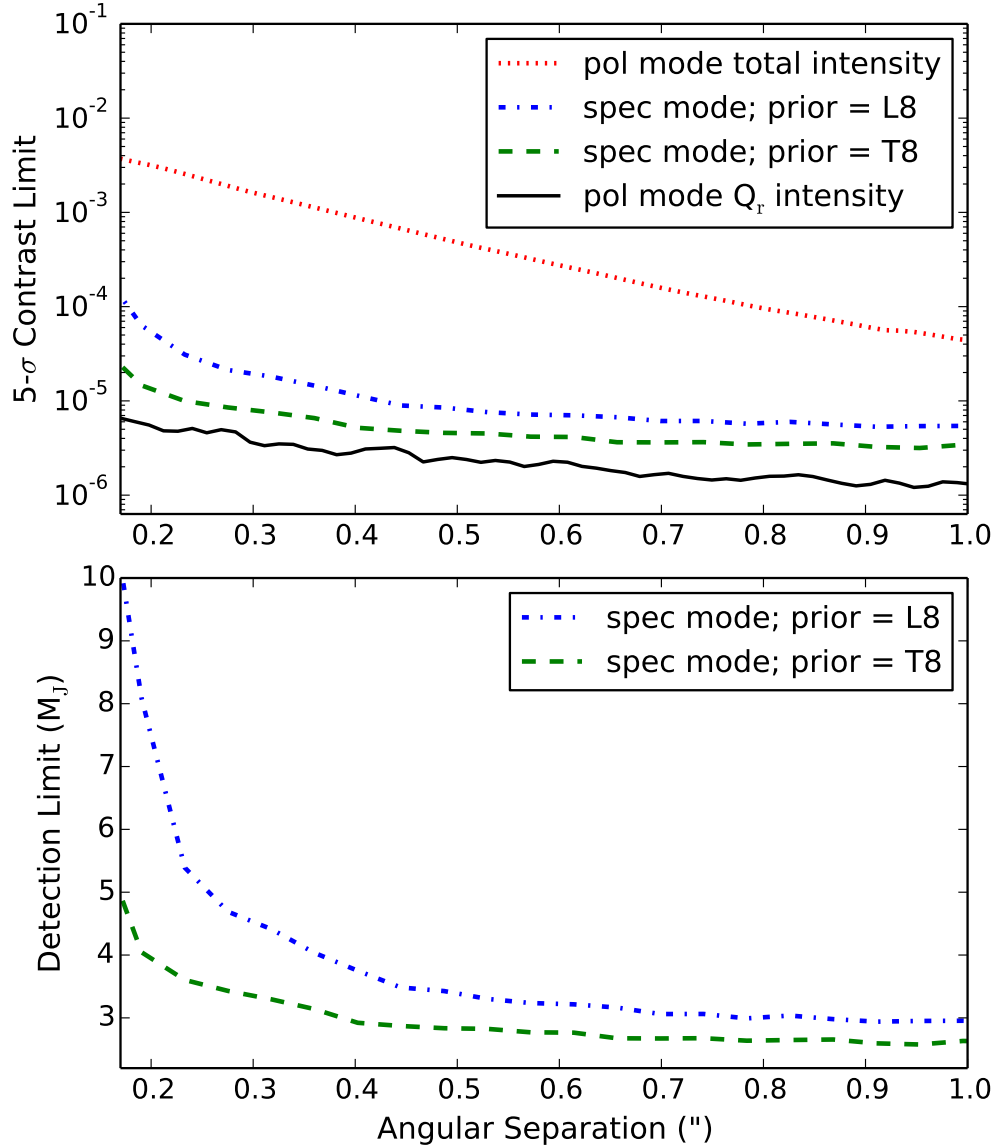


Figure 3.2 Limits on point-source detection from  $H$ -band polarimetry and spectroscopic observations. Top:  $5\sigma$  point-source contrast curves. Bottom: detection limit in terms of the mass of exoplanets. In the spectroscopic mode, prior spectra were used in the PSF subtraction, so both contrast and mass limits are spectrum dependent.

uncorrected systematic errors from the instrumental polarization and cut out the region beyond 260 au in the disk plane to reduce the number of pixels without a detected disk signal.

To measure the basic geometric properties of the disk, we adopt a simple two-dimensional continuous disk model. Since the disk is not detected at all azimuths, we cut off  $140^\circ$  symmetrically about the SE semiminor axis in our model (white dashed lines in Figure 3.3) to exclude the region with  $S/N \leq 1$ . The model extends from the inner radius  $r_{in}$  to the outer radius  $r_{out}$ , with the surface brightness varying only as  $r^\alpha$ . Along with the position angle PA of the major axis and the inclination  $i$ , we use these five parameters to describe the geometric properties of the disk. We fit the data using the `emcee` python package (Foreman-Mackey et al., 2013b) based on the ensemble MCMC method of Goodman & Weare (2010b). After a burn-in period, we let the 100 walkers run for 1200 steps. The best-fit parameters and uncertainties listed in Table 3.1 are found by taking the median of the marginalized probability density distributions and finding the  $1\sigma$  confidence intervals. The shapes of the posterior distributions are all single-peaked and approximately normal. Assuming that the disk is optically thin and the polarization fraction and the phase function do not depend on the stellocentric radius, the value of  $\alpha$  implies a nearly flat surface density profile of  $\Sigma(r) \propto r^{-0.3}$ .

Next, we use the radiative transfer code MCFOST (Pinte et al., 2006, 2009) to generate the polarized scattered-light image and the SED. Using Mie theory, MCFOST self-consistently computes the absorption and scattering cross-sections as well as the scattering angle-dependent Mueller matrix, producing model images for all Stokes parameters. We assume a geometrically flat disk and start by modifying the two-component model from Hung et al. (2015a) to match the GPI image and the SED. We set the hotter extended component to have amorphous carbon (Li & Greenberg, 1997), as its composition is based on the suggested high grain temperatures (Hung et al., 2015a). We keep all its parameters (PA,  $i$ , disk extent  $r$ , power-law index of the surface density  $r_{slope}$ , grain size  $a$ , grain size distribution power-law index  $a_{slope}$ , and mass of the dust  $M_{dust}$ ) fixed as listed in Table 3.1. The cooler ring component has its geometry fixed to be the values found in the previous paragraph

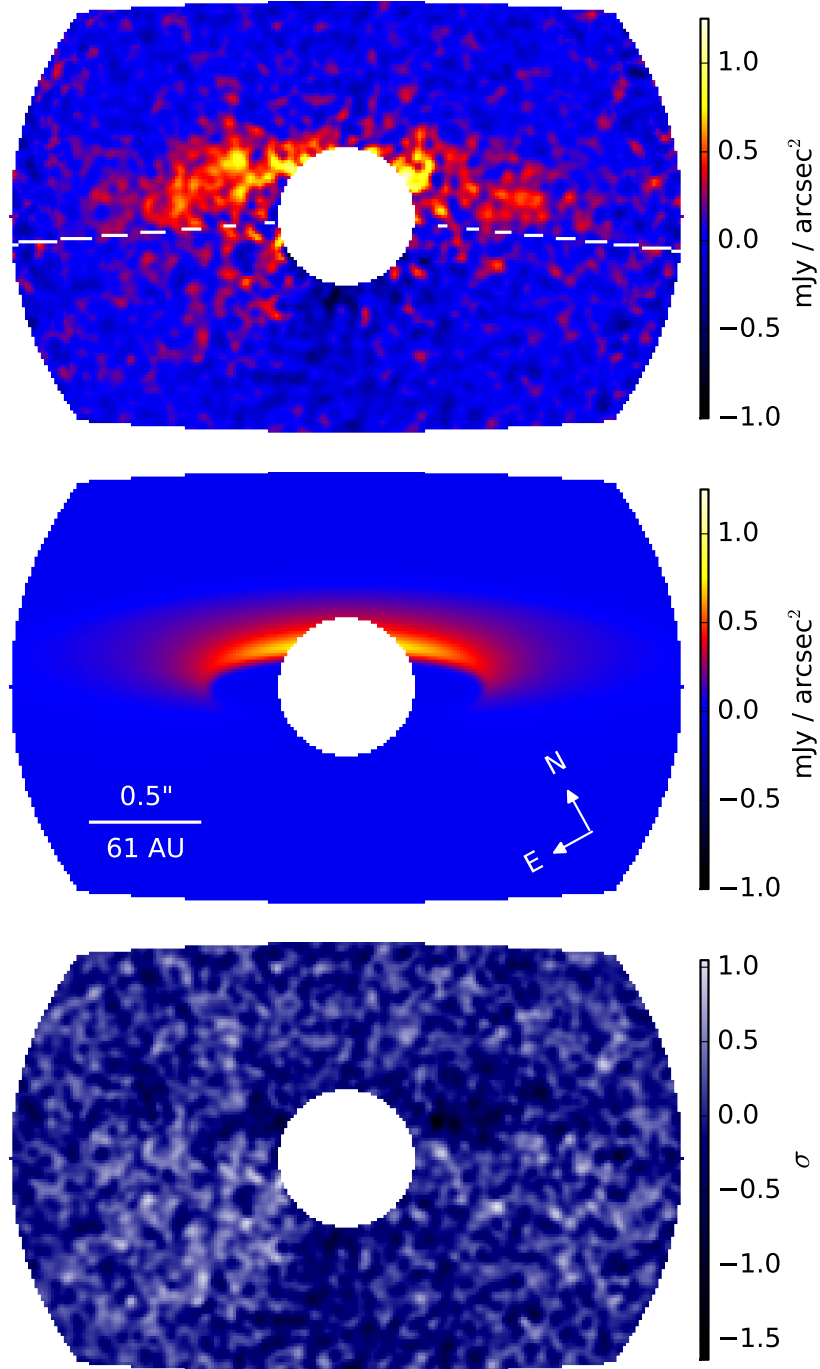


Figure 3.3 Comparison of the best-fit MCFOST image model to the observations. GPI polarized intensity data (Fig. 3.1), best-fit model, and residual images viewed through the fitting mask. All displayed images were smoothed with a Gaussian with an FWHM of three pixels. The geometric parameters of the MCFOST model were fixed to the values found by fitting the simple geometric model that only covers the azimuthal angles above the white dashed lines.

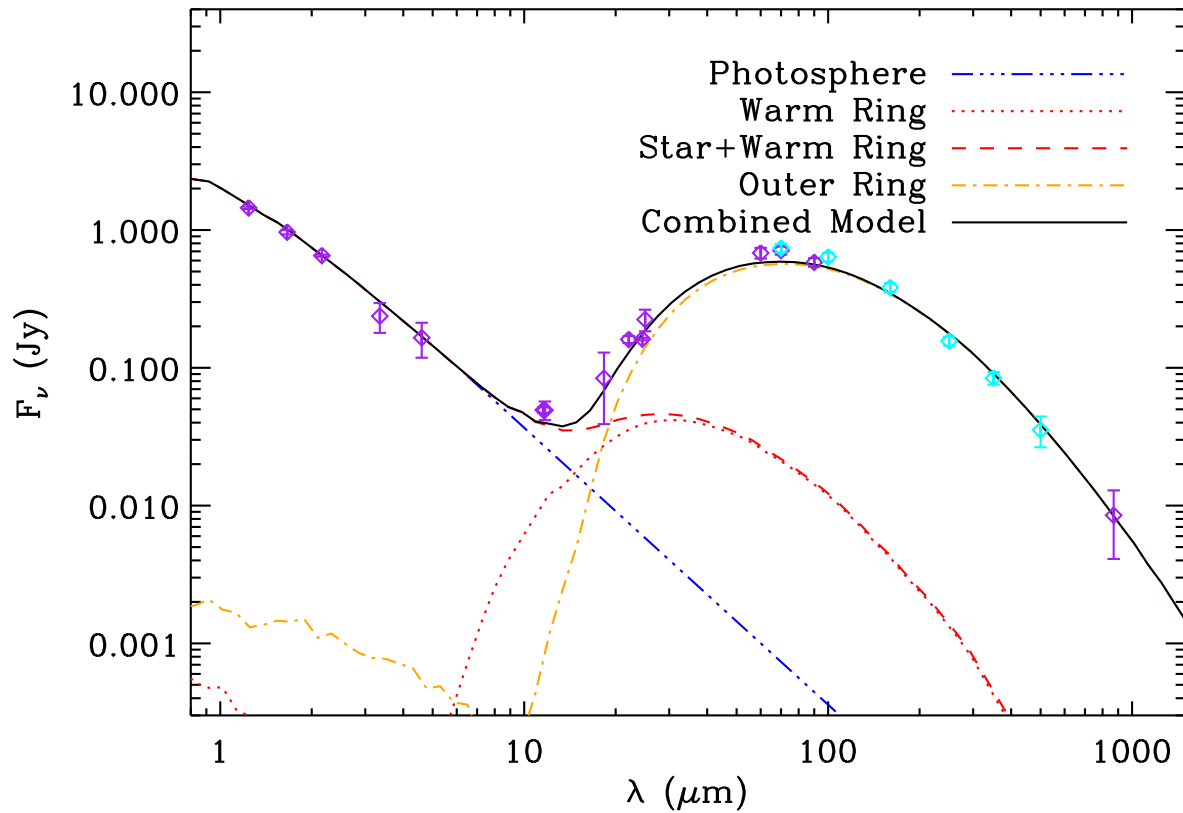


Figure 3.4 Comparison of the best-fit MCFOST SED model to the observations. The purple photometry values and references are summarized in Hung et al. (2015a). The additional *Herschel* points (cyan) are from Moór et al. (2015).

Table 3.1. Best-fit Model Parameters.

	Parameter	Value	Units
Geometric Parameters	PA	$61.4 \pm 0.4$	°
	$i$	$75.1^{+0.8}_{-0.9}$	°
	$r_{in}$	$75^{+2}_{-4}$	au
	$r_{out}$	$210 \pm 10$	au
	$\alpha$	$-2.3^{+0.2}_{-0.1}$	
Hotter MCFOST Model Component	PA*	61.4	°
	$i^*$	75.1	°
	$r^*$	35 – 400	au
	$r^*_{slope}$	0.5	
	$a^*$	0.03 – 5	$\mu\text{m}$
	$a^*_{slope}$	-3.5	
	$M^*_{dust}$	$6.66 \times 10^{-4}$	$M_{\oplus}$
	<i>composition*</i>	amorphous carbon	
Cooler MCFOST Model Component	PA*	61.4	°
	$i^*$	75.1	°
	$r^*$	75 – 210	au
	$r^*_{slope}$	-0.3	
	$a_{min}$	1.56	$\mu\text{m}$
	$a^*_{max}$	1.0	mm
	$a_{slope}$	-3.46	
	$M_{dust}$	$2.66 \times 10^{-1}$	$M_{\oplus}$
<i>composition*</i>	50% carbon + 50% silicate		

Note. — \*kept fixed

and its composition set to be 50% amorphous carbon and 50% astro-silicate (Draine & Lee, 1984b). We have considered arguably simpler compositions (pure silicates and pure amorphous carbon) but they produce worse model fits. Adding water ice to the composition or porosity to the grains also leads to poorer model fits.

We simultaneously fit our MCFOST model to the SED and the scattered-light disk at all azimuthal angles. In the fit, we weight the residuals from each pixel and broadband photometry point equally. In addition to fitting photometry points longward of  $10 \mu\text{m}$  (summarized in Hung et al. 2015a), we include six new *Herschel* points from Moór et al. (2015). With the disk geometry and dust composition fixed, the only free parameters are the size distribution and  $M_{dust}$ . The SED can only place a lower limit on the maximum grain size so we adopt  $a_{max} = 1 \text{ mm}$ . This only leaves the minimum grain size  $a_{min}$ ,  $a_{slope}$ , and  $M_{disk}$  of the cooler component to vary. To explore the parameter space, we use the genetic algorithm (Mathews et al., 2013), which ensures a fast convergence.

The best-fit MCFOST model reproduces the SED and the observed scattered-light disk with the reduced  $\chi^2$  of 0.97. The fit is shown in Figure 3.3 and 3.4, and the parameters are listed in Table 3.1. The best-fit model image fits the disk ansae well. The slight over-subtraction near the inner edge is not significant given the noise in these regions. Although the hotter component does not contribute significantly to the scattered-light image, this component is an important source for thermal emission. Our best-fit MCFOST model also roughly reproduces the extended thermal emission. We can further improve our model with detailed analysis, such as more complex dust composition and grain size distribution, but those are beyond the scope of this letter. Nonetheless, we set strong constraints on the disk properties, reproducing the surface brightness of the scattered-light disk with a model that was initially devised exclusively on thermal emission. We find a minimum grain size that is in reasonable agreement with the expected blowout size of  $0.91 \mu\text{m}$  and the grain size power-law index is only slightly steeper than the canonical  $a_{slope} = -3.5$ . Overall, the grains detected with GPI seem to follow the intuitive expectations of common disk properties.

### 3.7 DISCUSSION AND SUMMARY

The mid-IR (Hung et al., 2015a) and scattered-light images show different morphology. Unlike the continuous and extended thermal emission, the disk in scattered light has a cleared region inward of  $\sim 75$  au. In other words, the scattered-light disk starts at a radius that is twice as far away from the star compared to the disk in thermal emission. In polarized scattered light, we detect brightness asymmetries strongly along the minor axis and weakly along the major axis. The brightness asymmetry along the minor axis is likely due to asymmetry in the scattering phase function and is present in our best-fit model. The brightness asymmetry along the major axis could be the result of a dust density enhancement, azimuthal variation of grain compositions, or a projection effect of an eccentric disk if this  $3\sigma$  feature is real. Since the mid-IR data do not show the asymmetry along the major axis, it suggests that the large grain population is more symmetrically arranged than the small grain population. The simulation done by Wyatt (2006) shows that dust that originates in the break-up of planetesimals trapped in resonance with a planet can have moderate-sized grains (a few  $\mu\text{m}$  to a few mm) distributed axisymmetrically but small grains (less than a few  $\mu\text{m}$ ) exhibit trailing spiral structure that emanates from the resonant clumps. Therefore, the mismatched distributions of large and small grains can identify different forces acting on them and highlight potentially interesting dynamical interactions in the system.

HD 131835 is distinctive compared with the other Sco-Cen debris disks that have recently been imaged in scattered light: HIP 79977, HD 115600, HD 106906, and HD 110058 (Thalmann et al., 2013; Currie et al., 2015; Kalas et al., 2015; Kasper et al., 2015). Among those, HD 131835 has the largest inner radius in the scattered-light-detected component and the most radially extended and nearly flat surface density profile (from 75 to 210 au with  $\Delta r/r \sim 1$ ). The other disks either have relatively narrow belts (HD 115600, HD 106906, and HD 110058) or have relatively sharp declines in brightness (HIP 79977). The extended and approximately flat surface density profile suggests that the parent body belt of HD 131835 is likely to be extremely broad, much more so than any other debris disks imaged to date. This novel feature we found indicates that the silicate component is not distributed in the form of

one or two narrow rings as previously suggested by Hung et al. (2015a). In addition, among all the Sco-Cen disks, HD 131835 is the only resolved disk with detected CO gas (Moór et al., 2015), making it a unique and valuable target for studying gas-dust interactions. Besides the potential dynamical influence of undetected exoplanets, interactions between dust and gas could also play a significant role in clearing the dust in the inner disk and creating an eccentric ring (Lyra & Kuchner, 2012).

Follow-up observations and detailed modeling are required to characterize the disk in detail. Deeper polarimetry observations are needed to confirm the NE–SW asymmetry. Detection of the disk in total intensity can set a firm constraint on the grain shape and porosity by providing the information on the fractional polarization as a function of scattering angle. Multicolor observations can further constrain the grain composition. Since HD 131835 is located in the southern sky, GPI, SPHERE (Spectro-polarimetric High-contrast Exoplanet Research), and ALMA (Atacama Large Millimeter/submillimeter Array) are powerful enough instruments/facilities for conducting follow-up observations.

This research was supported in part by NASA cooperative agreements NNX15AD95G, NNX11AD21G, and NNX14AJ80G, NSF AST-113718, AST-0909188, AST-1411868, AST-1413718, and DE-AC52-07NA27344, and the U.S. Department of Energy by Lawrence Livermore National Laboratory under contract DE-AC52-07NA27344. Work by L.-W. Hung and A. Greenbaum is supported by the National Science Foundation Graduate Research Fellowships DGE-1144087 and DGE-1232825. We acknowledge the Service Commun de Calcul Intensif de l’Observatoire de Grenoble (SCCI) for computations on the supercomputer funded by ANR (contracts ANR-07-BLAN-0221, ANR-2010-JCJC-0504-01 and ANR-2010-JCJC-0501-01) and the European Commission’s 7th Framework Program (contract PERG06-GA-2009-256513). This work is based on observations obtained at the Gemini Observatory, which is operated by the Association of Universities for Research in Astronomy, Inc., under a cooperative agreement with the NSF on behalf of the Gemini partnership: the National Science Foundation (United States), the National Research Council (Canada), CONICYT (Chile), the Australian Research Council (Australia), Ministério da Ciência, Tecnologia e Inovação (Brazil), and Ministerio de Ciencia, Tecnología e Innovación Productiva (Argentina).

## CHAPTER 4

# Gemini Planet Imager Observational Calibration XII: Photometric Calibration in the Polarimetry Mode

Reproduced by permission of SPIE

(Hung, L.-W., Bruzzone, S., Millar-Blanchaer, M., et al. 2016, SPIE)

### 4.1 INTRODUCTION

In less than two years of its regular operations, the high-contrast instrument Gemini Planet Imager (GPI; Macintosh et al. 2014) has discovered a new exoplanet (Macintosh et al., 2015) and numerous resolved debris disks (Currie et al., 2015; Kalas et al., 2015; Hung et al., 2015a). GPI, specially designed for direct imaging and spectroscopy of exoplanets and debris disks, can also operate as a dual-channel integral field polarimeter. The instrument primarily operates with a coronagraph in place, enabling high-contrast observations at inner working angles as low as  $0''.15$ . Traditional coronagraphy, however, poses an obstacle for photometric calibrations since the majority of the on-axis starlight is blocked. To photometrically calibrate images in the polarimetry mode with a coronagraph in place, we present two methods that do not rely on directly measuring the stellar flux.

Satellite spots provide a means for accurate photometry and astrometry relative to the occulted central star. Satellite spots are a set of faint copies of the occulted star created by a diffractive grid superimposed on the apodizer in the pupil plane (Sivaramakrishnan & Oppenheimer, 2006; Sivaramakrishnan et al., 2010; Wang et al., 2014). These satellite spots have fixed relative intensities compared to the central star and fall at specified locations in the field of view. Photometric and astrometric calibration of coronagraphic observations in

spectroscopy mode have been developed using these fiducial satellite spots (Maire et al., 2014; Wang et al., 2014). This method is currently the predominant way to calibrate spectroscopic observations of GPI. A major difference is that in polarimetry mode, the satellite spots are not diffraction-limited PSFs but are smeared out radially into rod shapes due to their chromaticity. Therefore, although this calibration method is based on the same principle as what is currently being used in spectroscopy mode, a separate set of data processing procedures is needed for performing the photometric calibration on broadband polarimetric images instead of spectral cubes.

Here we present two methods we developed to perform the photometric calibration of coronagraphic observations in polarimetry mode. The first method relies on using the satellite spots directly, using a procedure analogous to what is done in spectroscopy mode. The second method relies on scaling the observations in polarimetry mode to the photometrically calibrated response in spectroscopy mode. Both of these methods directly or indirectly use the satellite spots. An advantage for using the first method is that it can be applied to the science images in polarimetry mode directly; this method does not rely on any additional images for calibration. The second method will be convenient for users who already have calibrated images of the same target in spectroscopic mode. When applicable, using both methods on the same data set can offer a consistency check on the photometric calibration processes and potentially get more precise calibrated products.

In this report, we first describe how we measure the flux of the satellite spots through aperture photometry in Sec. 4.2. Then, we present the method and characterize the uncertainty for performing the photometric calibration of coronagraphic observations in polarimetry mode directly using the satellite spots in Sec. 4.3. Next, we explore an alternative calibration method through characterizing the flux ratio between the polarimetry and spectroscopy observing modes in Sec. 4.4. Finally, we summarize our findings and propose how we might lower the calibration uncertainty with future observations in Sec. 4.5.

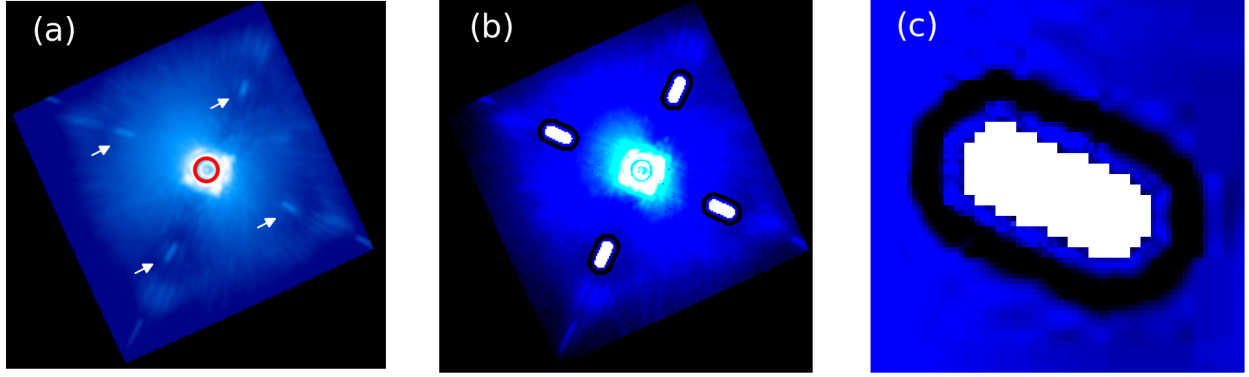


Figure 4.1 Reduced  $H$ -band images of HD 118666 observed with the coronagraph in polarimetry mode. (a) The red circle indicates the position and the size of the focal plane mask. The white arrows point to the satellite spots from the first-order diffraction. The satellite spots are smeared out radially into rod shapes due to their scaling with  $\lambda/D$  over the filter bandpass. (b) The white solid patches show the apertures used for measuring the flux of the satellite spots. The narrow black regions around the white apertures are used to estimate the background noise. (c) An enlarged view of the apertures used for the satellite spot (white) and for the background (black).

## 4.2 MEASURING SATELLITE SPOT FLUX IN POLARIMETRY MODE

To measure the fluxes of the satellite spots in images taken with the coronagraph in polarimetry mode, we first need to reduce the images. The raw polarimetry data were reduced using the GPI Data Reduction Pipeline (DRP; Perrin et al. 2014a). Polarimetry data were dark subtracted, cleaned for correlated noise (Ingraham et al., 2014), interpolated over bad pixels in the two-dimensional (2D) detector image, corrected for flexure (Draper et al., 2014), assembled into data cubes with the third dimension comprising the two orthogonal polarization states, and divided by a low spatial frequency polarized flat field. The default unit for the reduced data cubes is in analog-to-digital Unit (ADU) coadd<sup>-1</sup>. Fig. 4.1 (a) shows an example of a reduced polarimetry image. The satellite spots and the focal plane mask are marked by white arrows and a red circle. To extract the position and the flux of the satellite spots, we develop the primitive *Measure Satellite Spot Flux in Polarimetry* in the GPI DRP, and we describe the methodology below and the application in Sec. 4.3.3.

We determine the location of the satellite spots in the field of view according to the known diffraction properties of the pupil plane grating. The star’s position is measured through the DRP primitive *Measure Star Position for Polarimetry* using a Radon transform-based technique (Wang et al., 2014) which makes use of the satellite spots but does not directly output their positions. With the star’s position known, the radial position of the satellite spots at a particular wavelength  $\lambda$  will fall at an angular distance of  $\lambda/d$  relative to the occulted star, where  $d$  is the distance between the grid lines imprinted on the apodizer. In polarimetry mode, the satellite spots are not diffraction-limited PSFs but are smeared out radially into rod shapes due to their wavelength dependence and the broadband nature of the polarimetry mode. We determine the radial extent of the satellite spots by considering the band pass of the filter in use. The azimuthal position of the satellite spots is determined by measuring the mean angular position of satellite spots from a collection of the observed targets in spectral mode.

Next, we use aperture photometry with background subtraction to measure the flux of the satellite spots. Fig. 4.1 (b) shows the apertures used for measuring the source flux (white patches) and for measuring the background (narrow black regions around the white apertures). The satellite-spot aperture consists of a rectangle capped with semi-circles on each end of the long axis. The length of the rectangle is defined by the satellite spot positions at the minimum and maximum wavelengths of the observed band. The radius of the semicircle (half the width of the rectangle) is chosen to be slightly greater than the FWHM of the satellite spots in spectral mode. In the example *H*-band image, the length of the rectangle corresponds to 12 pixels, and the radius of the semicircle is chosen to be 4 pixels. To measure the background, we use a region that resembles a racetrack constructed using the annulus formed by two concentric but larger versions of the source aperture. For both the inner bound and outer bound of the racetrack, the length of the rectangle is still 12 pixels, but the radii of the end caps are 6 and 9 pixels for the inner and outer bounds of the annulus respectively. This aperture setting is referred as the [4,6,9] default setting later in the paper. We then apply the background correction to our measured flux of satellite spots.

## 4.3 CALIBRATION USING SATELLITE SPOTS DIRECTLY

### 4.3.1 Calibration Method

We take advantage of the well characterized satellite spot-to-star flux ratios to perform photometric calibration on the polarimetry data. This method is first described briefly in Ref. 41, and here we provide a more detailed description. We can convert a reduced image  $D_i$  from the default unit in ADU coadd<sup>-1</sup> into an image  $D_f$  with a physical unit (i.e., Jy) using

$$D_f = D_i \frac{R F_\star}{S}, \quad (4.1)$$

where  $R$ ,  $F_\star$ , and  $S$  are the satellite spot-to-star flux ratio, the stellar flux in physical units (i.e., Jy), and the average flux of satellite spots in ADU coadd<sup>-1</sup> respectively.

The satellite spot-to-star flux ratio depends on the specification of the apodizer used. The  $H$ -band measurements of the ratio and the corresponding magnitude difference are made with a combination of lab tests and the on-sky observations taken from the commission runs (Wang et al., 2014). When using the apodizers designed for  $Y$ ,  $J$ ,  $H$ ,  $K1$ , and  $K2$ , a star will be  $\sim 5000$  times brighter than the average brightness of its four satellite spots. The current best-estimated values for all apodizers are stored in the `apodizer_spec.txt` file which is included in the GPI DRP package for users to download.

The stellar flux,  $F_\star$ , is the flux, in a physical unit, of the central star observed through the filter. In the following study, we adopt the  $F_\star$  values from Two Micron All-Sky Survey (2MASS) observations. Corrections between 2MASS and GPI magnitudes in  $J$  and  $H$  filters were found to be negligible (Macintosh et al., 2015). The average satellite spot flux  $S$  can be found by taking the mean of the four satellite spot fluxes measured using the method described in Sec. 4.2.

### 4.3.2 Calibration Uncertainty

Here we characterize the uncertainty associated with this calibration method. High-contrast imaging in scattered light often suffers from speckle noise. These speckles can affect the

accuracy of photometric measurements and therefore introduce some systematic errors during the calibration process. It is well known that AO photometry is challenging and subjects to systematic biases due to the time-variable atmosphere (Lu et al., 2010). The variability in AO performance (Poyneer et al., 2014) can also affect the photometric calibration accuracy. To estimate the calibration uncertainty, we analyze the following data sets where a primary star and a companion are imaged in the same exposure with the primary star placed behind the occulter.

We estimate the GPI photometric calibration uncertainty in polarimetry mode by measuring the scatter of the flux ratio of the companion to the satellite spot. This scatter contains the uncertainty  $\sigma_R$  associated with the satellite spot-to-star flux ratio  $R$  described in Equation (4.1). This uncertainty should also captures the intrinsic variability of the satellite spots from them being coherent with the speckle noise. In spectroscopy mode, this intrinsic variability is estimated to be  $\sim 7\%$  (Wang et al., 2014). Ideally, to measure  $\sigma_R$  with the on-sky data, we would measure the scatter of  $R$  over a series of exposures. However, since the observed star is placed behind the mask, it prevents us from measuring the stellar flux and satellite spot flux simultaneously. To get around this problem, we measure the companion’s flux and the average satellite spot flux in each image instead. We then compute the scatter of the companion-to-satellite spot flux ratio over a series of images. This approximation approach also provides us the advantage for capturing the uncertainty caused by speckle noise. GPI uses the angular differential imaging technique so the sky will appear to rotate in the field of view as a function of time. The speckles, on the other hand, do not rotate with respect to the field of view. Therefore, over a period of time, the companion could rotate in and out of the static speckles and provide a more complete characterization by capturing the uncertainties caused by speckle noise.

We use the existing data set on HD 19467 system to estimate the GPI photometric calibration uncertainty. The system hosts a T5.5 brown dwarf companion, HD 19467 B, at the separation of  $\sim 1''.65$  from the primary G3V star (Crepp et al., 2014). On February 1, 2015, we obtained twenty-seven 60 seconds images of HD 19467 with GPI in the  $H$ -band polarimetry mode with the primary purpose of studying the polarization signal from the

companion (Jensen-Clem et al., 2016). The coronagraph was placed to block the primary star. Polarized signal was not detected from that study, suggesting it is possible that the T-dwarf is cloudless or has the clouds distributed symmetrically with respect to the viewing angles. Since most of the variability in brown dwarfs is thought to be caused by the time variation of the cloud distribution, the null detection in polarized signal implies that the source is likely to be not highly variable. Here we use the same data set to study the photometric calibration uncertainty assuming the source is not variable.

Using the HD 19467 data set, we estimate the GPI photometric calibration uncertainty in polarimetry mode to be  $< 13\%$ , with the limitation coming from the variation in the photometry of the companion. We measure the average flux of the satellite spots in each image as described in Sec. 4.2. To measure the flux of the companion, we use a circular aperture with a radius of 4 pixels. We then subtract the background estimated through the surrounding circular region between the inner and outer radii of 6 and 9 pixels. These aperture parameters are chosen to match the ones used for doing the photometry on the satellite spots. Fig. 4.2 shows the flux ratio measured in each image. Based on the scatter of the flux ratio of the companion to the average satellite spot for each image, we estimate the GPI photometric calibration uncertainty in polarimetry mode to be  $< 13\%$ . The current dominant source of error for estimating the calibration uncertainty comes from the photometry of the companion. Compared to the satellite spots, the companion is dimmer and suffers from the lower S/N. Although the photon noise for each measurement of the companion is only  $\sim 1.3\%$ , the flux measurements have variations of  $\sim 12\%$  due to speckle noise. The effect of correlations can be clearly seen in Fig. 4.2. This uncertainty of the companion flux measurement is similar to the one estimated based on a ring of apertures around the parent star at the same separation as the companion in the Stokes I frame (Jensen-Clem et al., 2016). Compared to the  $\sim 2\%$  variation of the average flux of the satellite spots, the flux variation of the companion is much higher. This large variation of the companion flux significantly affects the precision of measuring the companion-to-satellite spot flux ratio.

We examine another data set, HIP 70931, in hope to better constrain the calibration uncertainty. HIP 70931 is an A1V star with a companion at  $\sim 0''.60$  (De Rosa et al., 2014).

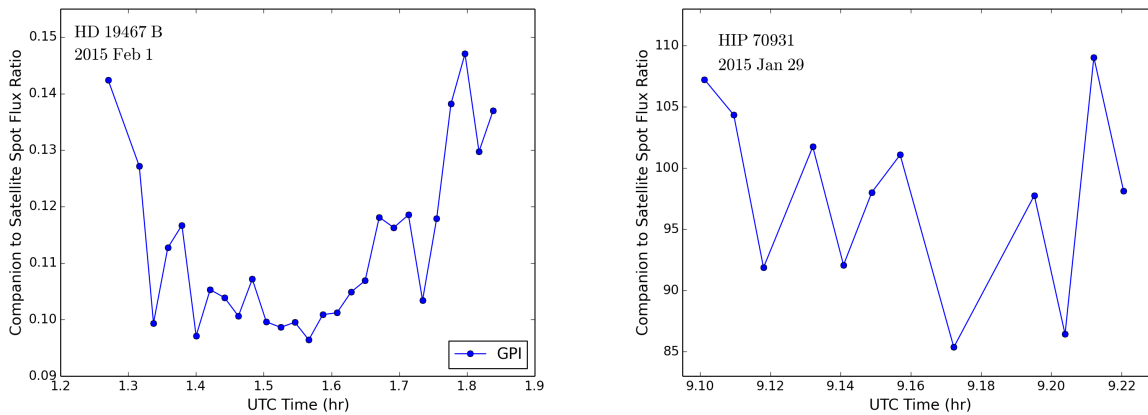


Figure 4.2 Left: Companion-to-satellite spot flux ratio of HD 19467. The blue dots are the GPI  $H$ -band measurements in polarimetry mode from this study. The flux ratio of the companion (HD 19467 B) to the average satellite spot is plotted for each image for the entire sequence. We estimate the GPI photometric calibration uncertainty in polarimetry mode to be 13% according to the scatter of this ratio. Right: Companion-to-satellite spot flux ratio of HIP 70931. The scatter of this ratio indicates the GPI photometric calibration uncertainty in polarimetry mode could be  $< 7.5\%$ . However, we note that this measurement might be corrupted since the companion in this data set is too bright that it falls on the nonlinear regime of the detector response.

On January 1, 2015, we obtained twelve 15 seconds  $H$ -band images of HIP 70931 with the coronagraph in polarimetry mode using GPI. The companion in this system is much brighter and provides higher S/N. However, although not saturated, the companion is so bright that it falls on the nonlinear regime ( $> 16,000$  ADU; Ingraham et al. 2014) of the detector response. Nonetheless, we still process the data set the same way as described above and plot the companion-to-satellite spot flux ratio in Fig. 4.2. This data set indicates the calibration uncertainty is  $< 7.5\%$ . Due to the concern of the nonlinear response of the detector, we note that we conservatively adopt the  $13\%$  measured from the HD 19467 data set as the photometric calibration uncertainty in the GPI polarimetry mode.

### 4.3.3 GPI Data Reduction Pipeline Implementations

We developed the primitives in the GPI DRP to perform photometric calibration in polarimetry mode. Users should first reduce the raw images into polarimetric data cubes with the star position measured, which can be done using the recipe *Simple Polarization Datacube Extraction*. Then, users can apply the *Measure Satellite Spot Flux in Polarimetry* primitive to extract the flux of the satellite spots. These measured values will then be stored in the header extension 1. Next, users can use the *Calibrate Photometric Flux in Pol Mode* primitive to convert the raw units in the reduced images to physical units. This primitive can be applied to the individual reduced files or the final Stoke’s cube. These primitives are available for users with the DRP version of 1.4.0 or newer (Perrin et al., 2016). A tutorial with examples is created on the GPI Data Pipeline Documentation website<sup>1</sup> to guide the users through a typical reduction.

### 4.3.4 Photometry of HD 19467 B

We examine the accuracy of our photometric calibration by comparing our photometrically calibrated brightness of HD 19467 B to the published value from an independent study. We first calibrate our data and perform aperture photometry with background subtraction as

---

<sup>1</sup><http://docs.planetimager.org/pipeline/>

described in Sec. 4.3.2. No aperture correction is needed since the aperture setting used for the companion matches the one used for the satellite spots. Our GPI photometry measurements for each individual frames are plotted in Fig. 4.3. Using these simple aperture photometry values, we measure the  $H$ -band brightness of HD 19467 B to be  $0.078 \pm 0.011$  mJy, which is consistent with the published NIRC2 measurement of  $0.0708 \pm 0.0086$  mJy (Crepp et al., 2014). The uncertainty  $\sigma_C$  of the companion flux  $C$  is calculated using the following equation:

$$\sigma_C = C \sqrt{\left(\frac{\sigma_I}{I}\right)^2 + \left(\frac{\sigma_R}{R}\right)^2 + \left(\frac{\sigma_{F\star}}{F\star}\right)^2 + \left(\frac{\sigma_S}{S}\right)^2}, \quad (4.2)$$

where  $I$  is the average of the measured brightness of the companion.  $\sigma_I$  can be characterized by dividing the scatter of  $I$  by  $\sqrt{n}$ , where  $n$  is the number of frames. The fractional uncertainty of  $I$  in this case is 2.3%. The dominant source of error comes from the term  $\sigma_R/R$ , where it represents the 13% calibration uncertainty as found in Sec. 4.3.2. We calculate  $\sigma_{F\star}/F\star$  using the 2MASS  $H$ -band stellar magnitude of  $5.447 \pm 0.036$  (Cutri et al., 2003b). The term  $\sigma_S$  is calculated by dividing the scatter of  $S$  by  $\sqrt{n}$ , and the term gives less than 1% of fractional uncertainty. Here we assume all sources of errors are independent but we note that this could cause us to overestimate the overall uncertainty  $\sigma_C$ , since currently both  $\sigma_I$  and  $\sigma_R$  are affected by the precision of the companion photometry. In Sec. 4.5 we discuss some future improvements that can be made to disentangle the uncertainties.

### 4.3.5 Photometry of Beta Pictoris b

We observed  $\beta$  Pictoris b in polarimetry mode with the coronagraph in  $H$  band using GPI. The observations were taken on 2013 December 12 for the AO performance and optimization tests. We obtained forty-nine 60 seconds frames with waveplate angles rotating between  $0^\circ$ ,  $22.5^\circ$ ,  $45^\circ$ , and  $67.5^\circ$ . The total accumulated field rotation is  $91^\circ$ . The morphology of the debris disk and orbit of the planet has been studied in a great detail from these observations (Millar-Blanchaer et al., 2015). Here we reduce raw data and then use the photometric calibration primitives with the default [4,6,9] aperture setting to convert each image from

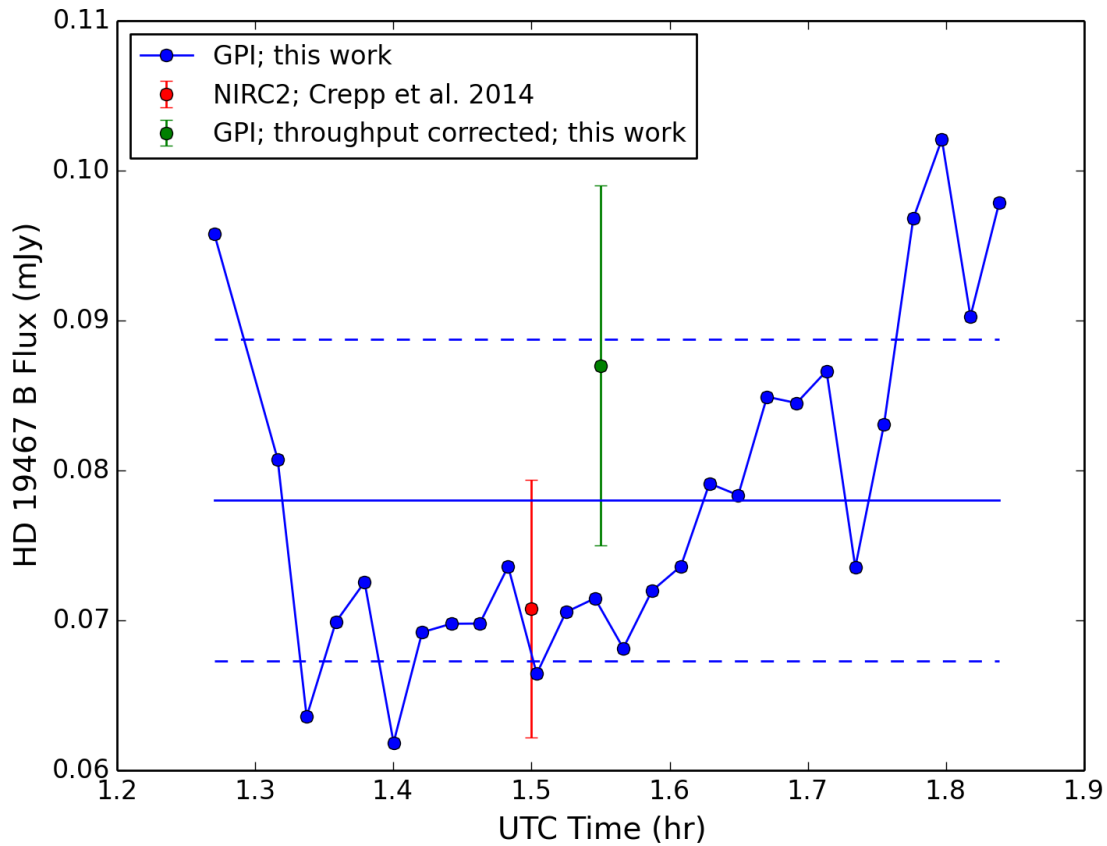


Figure 4.3 Photometrically calibrated measurements of HD 19467 B observations. The blue dots are the GPI  $H$ -band measurements in polarimetry mode from this study. The mean and the  $1\text{-}\sigma$  of the GPI measurements are presented as a solid and dash lines. The green point represents the detection throughput-corrected value. The throughput correction is not necessary for this data (see Sec. 4.3.6 for a detailed discussion). Our GPI measurements are consistent with the photometric measurement from NIRC2 at the Keck observatory (Crepp et al., 2014).

the raw unit to a physical unit following the steps described in Sec. 4.3.3.

We perform the simple aperture photometry with background subtraction to measure the brightness of  $\beta$  Pic b using the same procedures as described in Sec. 4.3.4. Our GPI photometry measurements for each individual frames are plotted in Fig. 4.4. Using these simple aperture photometry values, we measure the  $H$ -band brightness of  $\beta$  Pic b to be  $3.17 \pm 0.63$  mJy, which is represented as the horizontal lines in Fig. 4.4. The uncertainty of our measurement is calculated using Equation (4.2). The fractional uncertainty of  $I$  in this case is 15%, and the term  $\sigma_R/R$  is set to be 13%. These first two terms are the dominant sources of error here. Since these two terms are not completely independent (as discussed in Sec. 4.3.4), the actual combined uncertainty could be smaller than what we estimate here. We calculate  $\sigma_{F\star}/F\star$  using the  $H$ -band stellar magnitude of  $3.499 \pm 0.007$  (Morzinski et al., 2015). Each of the last two terms in the equation has less than 1% of fractional uncertainty.

The simple GPI photometry measurements seem to underestimate the flux of  $\beta$  Pic b when compared to the values found in the literature. The VLT/NaCo (red point in Fig. 4.4) and Gemini/NICI (yellow point)  $H$ -band measurements show that  $\beta$  Pic b has  $\Delta m$  of  $9.83 \pm 0.14$  and  $9.76 \pm 0.18$  (Currie et al., 2013; Morzinski et al., 2015), corresponding to the flux of  $\sim 4.77 \pm 0.66$  and  $5.09 \pm 0.49$  mJy. Our GPI measurement of  $3.17 \pm 0.63$  mJy is inconsistent with these published values. We suspect that our measurements are suffering from the over estimated background values. The planet’s PSF is bright and extended, and the first airy ring can be seen in each image. A significant portion of the first airy ring overlaps with the background aperture, causing the over-estimated background value. To overcome this problem, we perform the following analysis to correct the detection throughput.

### 4.3.6 Detection Throughput Correction

Our throughput corrected GPI flux measurement of  $\beta$  Pic b in  $H$  band is  $4.87 \pm 0.73$  mJy, which agrees with other measurements found in the literature. As mentioned above, our simple photometry measurements seem to overestimate the background flux due to the overlap between the background aperture and the bright airy ring. Accurately measuring the

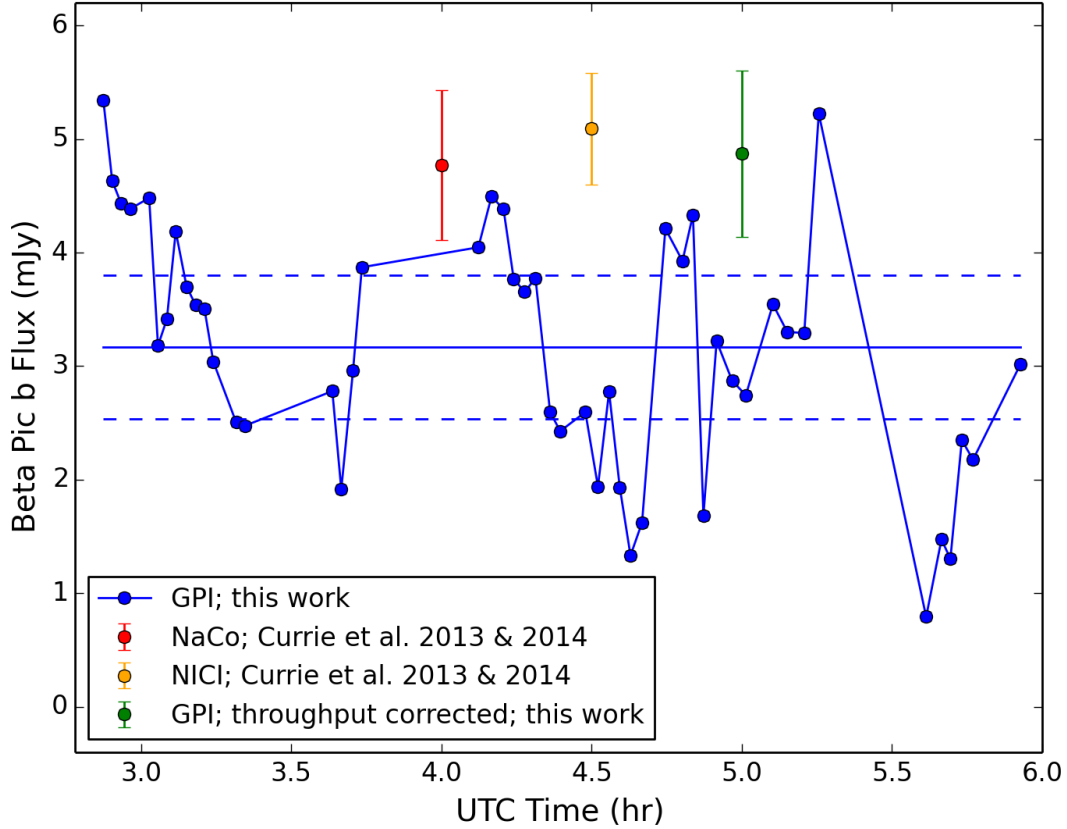


Figure 4.4  $H$ -band photometry of  $\beta$  Pictoris b. The GPI data were taken on 2013 December 12. The blue points are the photometry measurement of the individual frames using the default aperture setting of [4,6,9] pixels in the GPI DRP. The horizontal lines represent the mean and  $1\sigma$  values of the blue points. The simple GPI photometry measurements are not consistent with other published measurements (red and yellow points) (Currie et al., 2013; Morzinski et al., 2015). The inconsistency is likely due to overestimated background levels in the GPI measurements since the PSF of the planet is extended. We compute the detection throughput by comparing the detected brightness of the injected point sources to their given brightness. The throughput-corrected GPI photometry measurement (green point) is consistent with other literature values.

background using the nearby region is difficult since the stellar halo light and speckles make the stellar PSF to have high spatial variations at this separation. Therefore, instead of trying to accurately characterize the background, we inject and then recover artificial point sources in the nearby regions to correct for the detection throughput. We extract the point source PSF from one of the stars in Theta Ori B using the data set taken in  $H$  band on January 31, 2015. We inject point-source PSFs with the same planet-star separation but at the position angles of  $\pm 35^\circ$  from  $\beta$  Pic b in each frame. This position angle offset is selected to allow the PSF to be injected closest to the real planet but still have the non-overlapping apertures between to real and injected sources. We then use the aperture photometry to measure the brightness of the injected sources using the same aperture setting as what is used on  $\beta$  Pic b. We find that in order to have our averaged detected flux of the injected source to match that of the  $\beta$  Pic b, the injected source has to be  $4.87 \pm 0.73$  mJy. We estimate the error by determining the range of the injected flux need to match the error range of the uncorrected flux. This detection throughput corrected value agrees with other measurements from the literature, and this photometric calibration study showcases the performance of the method developed in this paper.

The detection throughput correction is not necessary for the photometry measurement of HD 19467 B. We perform the same correction process for this system except for injecting the artificial source at  $90^\circ$  (instead of  $\pm 35^\circ$ ) away from the companion to keep it inside the field of view. The throughput-corrected value is  $0.087 \pm 0.012$  mJy (green point in Fig. 4.3), which is consistent with the original value from the simple aperture photometry. With its diffraction rings buried in the background, we show that the detection throughput correction for our HD 19467 data set is not necessary.

We note that this detection throughput correction might be needed only when performing aperture photometry; it is not a problem of the flux calibration itself. This detection throughput analysis is mainly correcting for the errors from the background subtraction process when doing aperture photometry. As demonstrated above, not all photometry cases will need it; it is only necessary for the cases where getting the accurate background estimate is difficult while doing aperture photometry. For data sets with disks instead of planets,

there is no need for a throughput correction for the disk surface brightness since no aperture photometry is involved. In addition, since disks are usually much more extended than a point source PSF, the surface brightness of a disk is less sensitive to the smearing effect of the PSF comparing to the point sources.

## 4.4 CALIBRATION USING SPECTROSCOPY MODE OBSERVATIONS

Here we present an alternative approach to perform the photometric calibration. This method can be used on polarimetric data sets for targets which also have spectroscopic observations with GPI. This method works under the assumption that the data quality from the two modes is similar. Instead of calibrating using the satellite spots directly, this calibration method works through scaling the polarimetric observations to the calibrated observations in spectroscopy mode.

### 4.4.1 Calibration Method

This method depends on two things: the photometric calibration in spectroscopy mode and the flux ratio between the reduced images in polarimetry and spectroscopy modes. The principle of this calibration method can be explained using the following equation:

$$D_f = D_i \times \frac{R F_{\star,spec}}{S_{spec}} \times \frac{1}{P}, \quad (4.3)$$

where  $F_{\star,spec}$  is the host star spectrum,  $S_{spec}$  is the average satellite spot spectrum, and  $P$  is the polarimetry-to-spectroscopy flux ratio.

The photometric calibration in spectroscopy mode (Maire et al., 2014) has been developed for determining the first fraction in Equation (4.3). This process uses the satellite spots and is based on the same principle as in Sec. 4.3. For calibrating the spectral data cubes, the spectra  $F_{\star,spec}$  and  $S_{spec}$  are used instead of the broadband  $F_{\star}$  and  $S$  fluxes. The corresponding

reduction primitives and recipes are available in the GPI DRP<sup>2</sup>. The photometric calibration process in spectroscopy mode will provide the conversion factor necessary for transforming the images in raw units to physical units.

Characterizing the second component, the polarimetry-to-spectroscopy flux ratio  $P$ , enables the meaningful comparison between the reduced images taken in these two modes. This characterization is necessary due to the potential difference stemming from different throughput and reduction processes between these two modes. Ideally, with the same integration time on the same target, we expect the total raw counts to be the same in spectroscopy and polarimetry modes. However, the light path in polarimetry mode is slightly different from the one in spectroscopy mode. For example, the polarimetry mode uses the half-wave plate and the Wollaston prism instead of the spectral prism. The difference in the light path can introduce some small differences in throughput. In addition, different pipeline primitives are used to reduce the raw data due to the nature of the actions needed to extract the information from the raw images. This post processing process can also introduce some variations in the reduced images between the two modes. We provide a detailed discussion about estimating the value of  $P$  in the following section.

#### 4.4.2 Scaling Factor

There are two extraction methods, *BOX* and *PSF*, available to assemble polarimetric data cubes in the GPI DRP (Millar-Blanchaer et al., 2016). The *BOX* method implements a  $5 \times 5$  box centered at each polarimetry spot while the *PSF* method uses the empirically calibrated subpixel lenslet PSF model. Given the same input raw file, these two methods produce the data cubes with similar signal-to-noise ratio. However, the *BOX* method seems to produce polarimetric data cubes that are unexpectedly brighter than spectroscopic observations, making using this method less favorable. The extraction algorithm used for reducing the polarimetric data is therefore set to be the *PSF* option in this study. The *PSF* algorithm is also the default standard mode for reducing data in all pipeline recipe templates.

---

<sup>2</sup>[http://docs.planetimager.org/pipeline/usage/tutorial\\_spectrophotometry.html](http://docs.planetimager.org/pipeline/usage/tutorial_spectrophotometry.html)

Table 4.1 Satellite spot flux ratio of polarimetry to spectroscopy modes among eleven science targets observed in both modes with GPI. The uncertainty  $\sigma$  represents the standard deviation of the measurements.

Name	Ratio	$\sigma$
49 Cet	1.11	0.09
$\epsilon$ Eri	1.09	0.09
V435 Car	0.99	0.05
HD 31392	1.10	0.13
$\gamma$ Dor	1.11	0.26
$\gamma$ Ophi	1.09	0.07
HD 74576	1.05	0.09
HR 826	0.97	0.11
HR 6948	1.05	0.10
HD 19467	0.98	0.05
HIP 70931 (Mar 2014)	1.07	0.08
HIP 70931 (Jan 2015)	1.02	0.06

We examine this scaling factor between the reduced polarimetric and the spectroscopic images by comparing the flux of their satellite spots. The reduced polarimetric and spectroscopic cubes were collapsed to form the 2D broadband total intensity images. In the collapsed images, the satellite spots in the spectroscopic images become smeared, having the same rod-like appearance as the satellite spots in polarimetry mode. We then use the process described in Sec. 4.2 to perform the photometry of the satellite spots with the default aperture size setting of [4, 6, 9] in  $H$  band. Next, we compute the total flux of satellite spots for each image and then average over the sequence of images. These two mean values are then compared to measure the brightness ratio in polarimetry to spectroscopy mode. These calculations are all done in units of ADU. Table 4.1 lists the ratios we measured for eleven different targets. The weighted average of this ratio indicates the satellite spots in polarimetry mode are  $1.02 \pm 0.02$  times brighter than the ones in spectroscopy mode.

Applying the same technique to the flux of the companion, HIP 70931 B, also provides the consistent result that the polarimetric images are slightly brighter than the spectroscopic

Table 4.2 Ratio of the companion fluxes in polarimetry to spectroscopy modes. The uncertainty  $\sigma$  represents the standard deviation of the measurements.

Name	Ratio	$\sigma$
HD 19467 B	1.07	0.43
HIP 70931 B (Mar 2014)	1.06	0.02
HIP 70931 B (Jan 2015)	1.02	0.01

images. In the data sets we examined earlier, HD 19467 and HIP 70931 each has a companion. Unlike the satellite spots, the companions in the collapsed 2D images still retain their point-source-like PSFs. We perform the aperture photometry on the companions and compare their brightness ratios in polarimetry to spectroscopy mode. The result is summarized in Table 4.2. The weighted average of this flux ratio is  $1.03 \pm 0.01$ . This ratio, derived from comparing the flux of the companions, is consistent with the one derived using the satellite spots. We note that this result indicates the effect is either due to the difference in throughput or in datacube extraction, not due to the way we measure the satellite spot flux.

## 4.5 SUMMARY AND FUTURE WORK

In this paper, we present the newly developed methods for performing photometric calibration of GPI coronagraphic data taken in polarimetry mode. Photometrically calibrating these images relies on using the satellite spots. We develop a new primitive in the GPI DRP (version 1.4.0 or newer (Perrin et al., 2016)) for measuring the flux of the satellite spots in polarimetry mode with aperture photometry. The first calibration method we present here uses the satellite spots directly. The principle of this method is based on computing the unit converting factor from the known satellite spot-to-star flux ratio, the known stellar flux in a physical unit, and the measured average flux of the satellite spots. With the current available data, we can constrain the associate photometric calibration uncertainty to be  $< 13\%$ . We use this method to photometrically calibrate the  $H$ -band polarimetric observations of HD 19467 B and  $\beta$  Pic b. Then we measure the calibrated flux of HD 19467 B and  $\beta$  Pic b to

be  $0.078 \pm 0.011$  and  $4.87 \pm 0.73$  mJy respectively. Both of these measurements agree with other values found in the literature, showing that the photometric calibration method we develop here can produce consistent results with other observations. Finally, we present an alternative photometric calibration method. This calibration method works through scaling the polarimetric observations to the calibrated observations in spectroscopy mode. By comparing the observations in polarimetry to spectroscopy mode, we find that this scaling factor is  $1.03 \pm 0.01$ , with the observations in polarimetry mode being brighter.

To lower the calibration uncertainty, higher S/N observations of a star-companion system are needed. The current upper limit for the photometric calibration uncertainty is 13% when using the satellite spots to photometrically calibrate the GPI coronagraphic observations in polarimetry mode. The current dominant source of error for estimating this calibration uncertainty comes from the photometry of the companion. Observing HD 8049 in polarimetry mode might provide a better constraint to lower this calibration uncertainty. HD 8049 is a K2V star with a white dwarf companion (Zurlo et al., 2013). The flux ratio of this star-companion is ideal since we can expect to get good S/N ratio of the companion in a reasonable exposure time ( $\sim 60$ s) and not worry about saturating either the companion or the satellite spots. The separation of  $1''.566 \pm 0''.006$  between the two bodies also conveniently locates the secondary near the edge of the field of view, far away from the halo light of the primary star.

Future work on characterizing the photometric calibration uncertainty in polarimetry mode can be expended in other wavelengths. Our study here focuses on the data in  $H$  band since there are existing data we can use right away for this characterization work and  $H$  is the most commonly used filter in the our GPI Exoplanet Survey. If new observations need to be taken for the calibration purpose, HD 8049 would again serve as an ideal system.

## ACKNOWLEDGMENTS

This research was supported in part by NASA cooperative agreements NNX15AD95G, NNX11AD21G, and NNX14AJ80G, NSF AST-113718, AST-0909188, AST-1411868, AST-

1413718, and DE-AC52-07NA27344, and the U.S. Department of Energy by Lawrence Livermore National Laboratory under DE-AC52-07NA27344. Work by L.-W. Hung is supported by the National Science Foundation Graduate Research Fellowship number 2011116466 under Grant number DGE-1144087. This work is based on observations obtained at the Gemini Observatory, which is operated by the Association of Universities for Research in Astronomy, Inc., under a cooperative agreement with the NSF on behalf of the Gemini partnership: the National Science Foundation (United States), the National Research Council (Canada), CONICYT (Chile), the Australian Research Council (Australia), Ministério da Ciência, Tecnologia e Inovação (Brazil), and Ministerio de Ciencia, Tecnología e Innovación Productiva (Argentina).

# CHAPTER 5

## Conclusions

Discovered exoplanets, ranging from hot Jupiters to solar system analogs for example, have a diverse range of characteristics. One approach to understand giant planet formation and evolution is to image the associated debris disks at high contrast. Debris disks are composed of dust which originated from planetesimals orbiting stars and are an integral part of planetary systems. By resolving a debris disk, we can characterize the spatial distribution and properties of dust grains and infer the dynamical history of the system. My thesis focuses on studying the debris disk around HD 131835, which is a  $\sim 15$  Myr old (Mamajek et al., 2002a; Pecaute et al., 2012a) A2IV star (Houk, 1982) at a distance of  $123^{+16}_{-13}$  pc (van Leeuwen, 2007a) in the Upper Centaurus Lupus (UCL) moving group (Rizzuto et al., 2011a), a subgroup of the Sco-Cen association. Its IR emission was discovered by *Infrared Astronomical Satellite* (Moór et al., 2006a). MIPS observations showed that it is one of only four UCL/Lower Centaurus Crux A-type stars with  $L_{\text{IR}}/L_{*} > 10^{-3}$  (Chen et al., 2012a). Unlike most debris disks which are gas depleted, CO is detected in HD 131835 (Moór et al., 2015). For this system, the potential dynamical influence from both undetected exoplanets and gas should be considered. My thesis reports the first resolved images (Fig. 5.1), detailed analysis, and physical models of the debris disk in multiple wavelengths. Being a rare resolved debris disk with detected gas, HD 131835 serves as a laboratory for studying the relationship between gas-dust physics and planetary science.

Chapter 2 (Hung et al., 2015a) reports the discovery of the resolved disk around HD 131835 and presents the analysis and modeling of its thermal emission. The extended disk has been detected to  $\sim 1''.5$  (200 au) at  $11.7 \mu\text{m}$  and  $18.3 \mu\text{m}$  with T-ReCS on Gemini South. The disk is inclined at an angle of  $\sim 75^{\circ}$  with the position angle of  $\sim 61^{\circ}$ . The

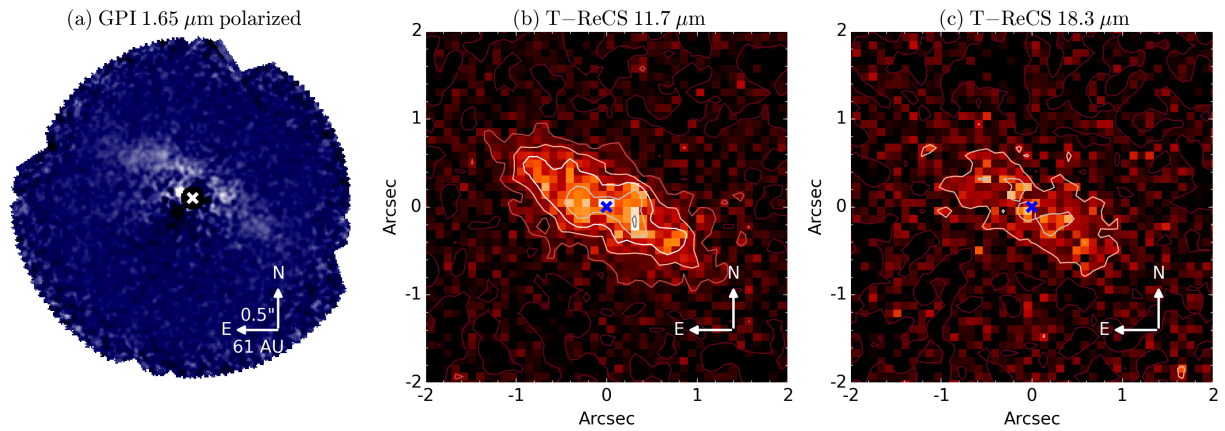


Figure 5.1 Debris disk around HD 131835. The star is marked in the center with the  $x$  symbol. (a)  $H$ -band linearly polarized intensity from GPI shows the cleared region within  $\sim 75$  au in the disk plane. The focal plane mask is marked as a filled black circle. The stronger forward scattering makes the front (NW) side of the disk more apparent. A weaker brightness asymmetry is detected along the major axis with the NE side being 1.3 times brighter than the SW side. Determining the nature of this weak brightness asymmetry is a goal of this program. (b) and (c) PSF subtracted Mid-IR images from T-ReCS show thermal emission from a continuous disk. Contours are spaced by the  $1\text{-}\sigma$  background noise level. The scattered-light disk shows similar orientation but different morphology compared to the mid-IR thermal emission.

flux of HD 131835 system is  $49.3 \pm 7.6$  mJy and  $84 \pm 45$  mJy at  $11.7 \mu\text{m}$  and  $18.3 \mu\text{m}$  respectively. A model with three grain populations gives a satisfactory fit to both the spectral energy distribution and the images simultaneously. This best-fit model is composed of a hot continuous power-law disk and two rings. We characterized the grain temperature profile and found that the grains in all three populations are emitting at temperatures higher than blackbodies. In particular, the grains in the continuous disk are unusually warm; even when considering small graphite particles as the composition.

Chapter 3 (Hung et al., 2015b) presents the first scattered-light image of the debris disk around HD 131835 in the  $H$  band using the Gemini Planet Imager (GPI). We detect the disk only in polarized light and place an upper limit on the peak total intensity. No point sources resembling exoplanets were identified. Compared to its mid-infrared thermal emission, the disk in scattered light shows similar orientation but different morphology. The scattered-light disk extends from  $\sim 75$  to  $\sim 210$  au in the disk plane with roughly flat surface density. Our Monte Carlo radiative transfer model can well describe the observations with a model disk composed of a mixture of silicates and amorphous carbon. In addition to the obvious brightness asymmetry due to stronger forward scattering, we discover a weak brightness asymmetry along the major axis, with the northeast side being 1.3 times brighter than the southwest side at a  $3\sigma$  level.

Chapter 4 (Hung et al., 2016) presents two newly developed photometric calibration methods for the coronagraphic images taken with GPI in polarimetry mode. The GPI is a high-contrast instrument specially designed for direct imaging and spectroscopy of exoplanets and debris disks. GPI can also operate as a dual-channel integral field polarimeter. The instrument primarily operates in a coronagraphic mode which poses an obstacle for traditional photometric calibrations since the majority of on-axis starlight is blocked. To enable accurate photometry relative to the occulted central star, a diffractive grid in a pupil plane is used to create a set of faint copies, named satellite spots, of the occulted star at specified locations and relative intensities in the field of view. We describe the method we developed to perform the photometric calibration of coronagraphic observations in polarimetry mode using these fiducial satellite spots. With the currently available data, we constrain the cali-

bration uncertainty to be  $< 13\%$ . We develop the associated calibration scripts in the GPI Data Reduction Pipeline, which is available to the public. For testing, we use it to photometrically calibrate the HD 19467 B and  $\beta$  Pic b data sets taken in the  $H$ -band polarimetry mode. We measure the calibrated flux of HD 19467 B and  $\beta$  Pic b to be  $0.078 \pm 0.011$  mJy and  $4.87 \pm 0.73$  mJy, both agreeing with other measurements found in the literature. Finally, we explore an alternative method which performs the calibration by scaling the photometry in polarimetry mode to the photometrically calibrated response in spectroscopy mode. By comparing the reduced observations in raw units, we find that observations in polarimetry mode are  $1.03 \pm 0.01$  brighter than those in spectroscopy mode.

## CHAPTER 6

### Appendix: GPI FPM Alignment Pipeline Work

#### 6.1 INTRODUCTION

The Gemini Planet Imager (GPI) is specially designed for direct imaging of exoplanets and debris disks. The instrument primarily operates with a coronagraph in place to enable high-contrast observations. The coronagraph consists of an apodizer, a focal plane mask (FPM), and a Lyot mask. An apodizer shapes the incoming beam of starlight and creates the satellite spots using the microdot printing (Sivaramakrishnan et al., 2009, 2010). Then the light reaches a FPM where the starlight in the PSF core gets removed. Finally, a Lyot mask is placed in a second pupil plane to reject the remaining diffracted starlight.

Determining where the position of the FPM falls on an image is important for aligning the star center to the FPM center and characterizing the instrumental polarization. If the star center is misaligned with the FPM center, the contrast in the surrounding area can become lower and therefore decreasing the probability of detecting exoplanets and disks. In addition, in polarimetry mode, we rely on using the starlight diffracted to fall at the same location as the FPM as the calibrator for the instrumental polarization. In the following section, I provide some characterization on the GPI instrumental polarization and the importance for removing it from the science observations.

#### 6.2 GPI INSTRUMENTAL POLARIZATION

We observed three unpolarized standard stars, HD 82386, HD 99171, and HD 210918, in the direct mode as the polarimetric calibrators during the commissioning runs in 2014.

The observations are summarized in Tab. 6.1. In the direct mode, observations were taken without a focal plane mask. To avoid saturating the detector within the minimum exposure time, the AO loop was set to open. The tip/tilt loop was open as well except for the last eight images of HD 210918 where the tip/tile loop was closed. The images were taken in sequences of different waveplate (WP) angles. Each sequence consisted of 4 images where the WP was rotated by  $22.5^\circ$  in between each exposure, with the total rotation of  $90^\circ$  over an entire sequence. We reduced the data using the GPI Data Reduction Pipeline (DRP; Perrin et al. 2014a) where the data were dark subtracted, corrected for flexure (Draper et al., 2014), cleaned for correlated noise (Ingraham et al., 2014), interpolated over bad pixels in the two-dimensional (2D) detector image, assembled into polarization data cubes (podc) with the third dimension comprising the two orthogonal polarization states, and interpolated over bad pixels in the cube. Since the AO loop was open, the star position and the PSF shape varied from exposure to exposure. To compute the mean polarization fraction as a whole and to avoid comparing the pixels with greatly different signal to noise ratio between images, we centralized all the flux in each podc slice into a single pixel. To get the Stokes cube, the four podc cubes (8 single-value pixels) from a WP sequence were combined using the Combine Polarization Sequence primitive in the DRP with the default setting which used the the lab measured values of the Mueller matrix elements.

We compute the polarization fractions and find that the instrumental polarization appears to be color-independent. Each Stokes cube here contains 4 single-pixel values:  $I$ ,  $Q$ ,  $U$ , and  $V$ . We compute the polarization fraction  $P$  as following:

$$P = \frac{\sqrt{Q^2 + U^2}}{I}. \quad (6.1)$$

for each Stokes cube. The result is plotted in Fig. 6.1, with the order of the WP sequence number following the description order in Tab. 6.1. Among all these observations, there is only one WP sequence taken in  $K2$  (the magenta point). The reduced podc images of this  $K2$  data set show a morié pattern, which is a signature of an artifact from the data pipeline systematics caused by the misaligned polarization spot calibration solution. Unfortunately,

Table 6.1 Unpolarized standard stars observed in the direct mode as the polarimetric calibrators. Filters are listed in the chronological order as when they were being used in the observations. N is the number of waveplate (WP) sequences associated with each filter. Each sequence consists of 4 images where the WP was rotated by  $22.5^\circ$  in between each exposure. iTime denotes the total integration time for each exposure.

Unpolarized Standard	UT Date	Filter Sequence	N	iTime (s)
HD 82386	2014-03-21	<i>H, J, Y, K1</i>	2	12
HD 82386	2014-03-25	<i>K1, H, J, Y</i>	2	12
HD 99171	2014-05-12	<i>H, J, Y, K1, K2, H</i>	1	30
HD 210918	2014-09-10	<i>H</i>	4	15

simply offsetting the calibration solution or correcting for flexure could not mitigate this problem. We therefore argue that this *K2* measurement is likely to be spoiled. For the rest of the bands, we compute the mean polarization fractions to characterize the instrumental polarization. Since all of our samples here are unpolarized standard stars, we assume all the detected polarization signals are from the instrumental polarization. The percentage (%) mean polarization fractions for *Y*, *J*, *H*, and *K1* are  $0.40 \pm 0.27$ ,  $0.62 \pm 0.37$ ,  $0.56 \pm 0.17$ , and  $0.76 \pm 0.59$  respectively. The uncertainties represent the sample standard deviations. The instrumental polarization appears to be color-independent based on our result here.

We note that the scatter in the measurements of *Q* and *U* can introduce some biases when calculating the mean polarization fraction. These biases come from the squared terms in Equation (6.1). Even when both *Q* and *U* measurements have zero means, the means of  $Q^2$  and  $U^2$  will not be zero as long as the sample standard deviations of *Q* and *U* are not zero. This effect will introduce a positive bias in the mean of *P*, with the magnitude of the bias dependent on the sample standard deviations of *Q* and *U*. We take a numerical approach to calculate this bias. For each band, we draw two large random samples: one from a normalized Gaussian with the mean of zero and  $\sigma$  of the sample standard deviation of  $Q/I$ , and the other with the same Gaussian except for having the  $\sigma$  being the sample standard deviation of  $U/I$ . We then use those values to calculate *P*. By taking the average of *P*, we find the bias in the polarization fraction in percentage (%) for *Y*, *J*, *H*, and *K1* to be 0.29,

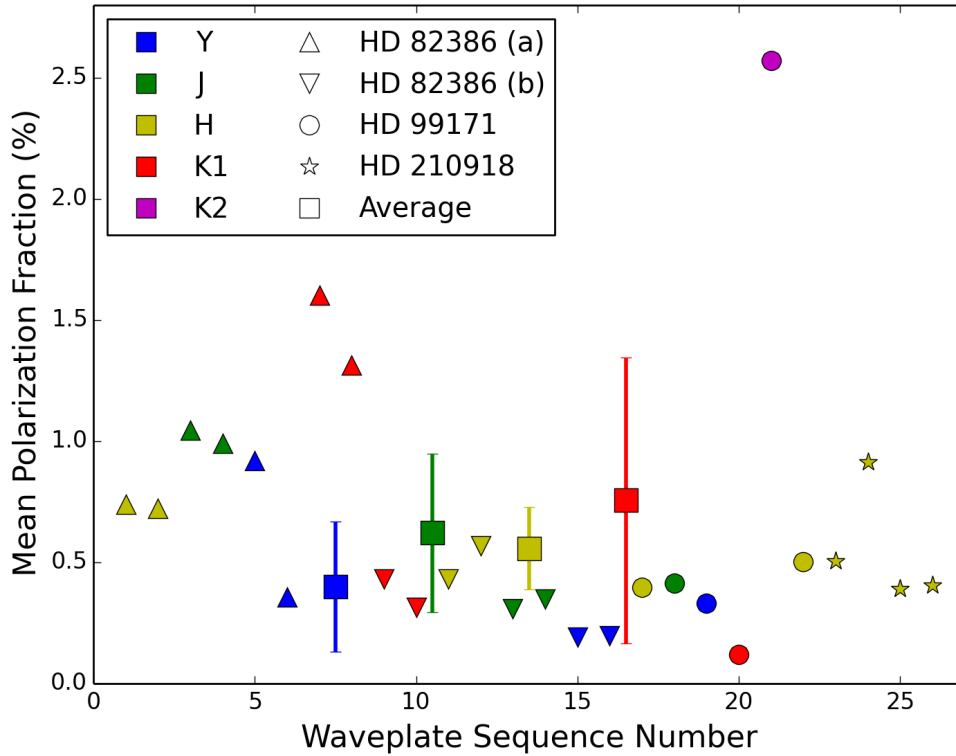


Figure 6.1 Instrumental polarization of GPI estimated with unpolarized standard stars. The observed bandpass is color-coded, and the different observations are denoted with different shapes. The WP sequence number follows the order of the data set description in Tab. 6.1. HD 82386 (a) and (b) data sets were taken 4 days apart. The only *K2* measurement is likely to be corrupted due to the misaligned polarization calibration solution. The percentage mean polarization fractions for *Y*, *J*, *H*, and *K1* are shown as squares, with error bars representing the sample standard deviations. The instrumental polarization appears to be color-independent with the average of  $\sim 0.6\%$  based on our result here.

0.30, 0.37, and 0.56. Although not all significantly, all of these biases are lower than the  $P$  measurements of the unpolarized standard stars found in the previous paragraph, showing the presence of the instrumental polarization.

Correcting for instrumental polarization is very important for science observations since it can completely obstruct faint signals. For example, the disk around HD 131835 (presented in Chapter 3) would not be detected if the instrumental polarization was left uncorrected. Fig. 6.2 shows detected (instrumental) polarized intensity of an unpolarized standard star HD 118666 in  $H$  band with the coronagraph. Tangentially polarized light shows up in  $+Q_r$ ; radially polarized light shows up in  $-Q_r$ . The  $U_r$  image shows the polarization with  $\pm 45^\circ$  offset from  $Q_r$ . The linearly polarized light from the instrument shows up like butterfly wings in these images. In most of the science observations, the FPM is used. We expect the polarized residual starlight diffracted to fall at the same location as the FPM to come from instrumental polarization since the starlight should be intrinsically unpolarized. By knowing the center of the FPM, we can select an optimal region to capture this polarized residual starlight in order to calibrate the science observations.

### 6.3 MEASURING THE FPM POSITION

FPM positions can be found by fitting models to the arc lamp images. Measuring the position of the FPM on an science image directly is challenging since the stellar halo makes the background non-uniform. This non-uniform background can affect the accuracy of the best-fit values of the FPM position. Instead of measuring the position of the FPM on science images, an alternative approach is to measure the FPM position on the arc lamp image that is taken before each science sequence for the spectral observations. The internal optical alignment between taking the arc lamp image and the science sequence does not change so the FPM position stays the same in the image. Without the highly non-uniform stellar halo in the background, fitting the FPM center in arc images can therefore provide more accurate position measurements.

I develop a primitive in the GPI DRP to measure the FPM position in an arc or a flat

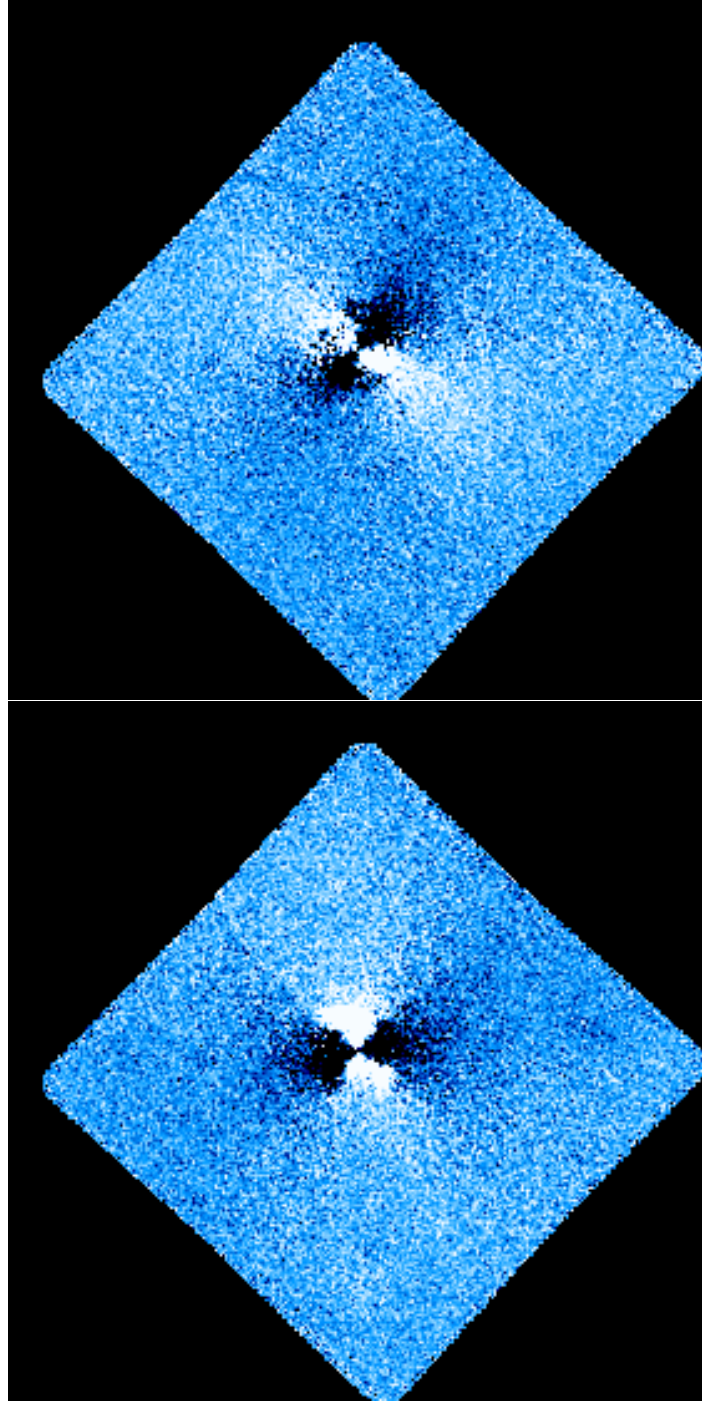


Figure 6.2 Detected (instrumental) polarized intensity of the unpolarized standard star HD 118666 in  $H$  band with the coronagraph. Top: image in the radial Stokes  $Q$ . Tangentially polarized light shows up in  $+Q_r$  (white); radially polarized light shows up in  $-Q_r$  (black). Bottom: image in the radial Stokes  $U$ . The  $U_r$  image shows the polarization with  $\pm 45^\circ$  offset from  $Q_r$ . The linearly polarized light from the instrument shows up like butterfly wings in these images.

image. Given an image with the FPM in place, the algorithm first estimates the rough position of the FPM by averaging the position of the pixels that have the values below a certain cutoff point. Then, the algorithm uses this rough estimation as the initial value for fitting the center of the FPM. I develop two models for fitting. Both models are 3D and are composed of a depressed circular region below a flat background. The difference is one model has a hard edge for the circular region and the other one has a soft edge instead. When using this primitive, users can specify the initial values of some fitting parameters, select the model function to be used, and adjust the fitting area. This primitive is available for users with the DRP version of 1.4.0 or newer.

I worked with other GPIES members in developing the displaying window for showing the calculated misalignment between the FPM and the star. Once the FPM position is measured from an arc image, the following science images will then compare the star center to this FPM center. Fig. 6.3 shows an example image viewed using the GPI-tv. The FPM position is marked by a yellow-black dash circle. The satellite spots are circled by green solid circles. The star position, determined by the position of the satellite spots, is marked by a cross sign. The star and the FPM in this example image is clearly misaligned. In the little pop-out window, it displays the suggested change in tip and tilt offset for aligning the star to the FPM. This offset calculation has been fully developed, and we are currently testing its accuracy and robustness.

Our goal is to use this misalignment calculation to automatically adjust the tip-tilt offset on the fly during observing runs and also later on provide the information about the center of the FPM for calibrating the instrumental polarization. Currently, adjusting the fine alignment between the star and the FPM is done manually, and the magnitude of the adjustment is estimated by eye. Once we have finished testing the robustness of the star-FPM misalignment calculation, we are aiming to implement it as a part of the auto-alignment feedback loop to keep the star always centered behind the FPM while observing. In addition, once this process is mature, we can take a flat image either before or after each sequence of polarimetry observation and use the flat image to measure the position of FPM. This method can provide accurate FPM positions for correcting the instrumental polarization.

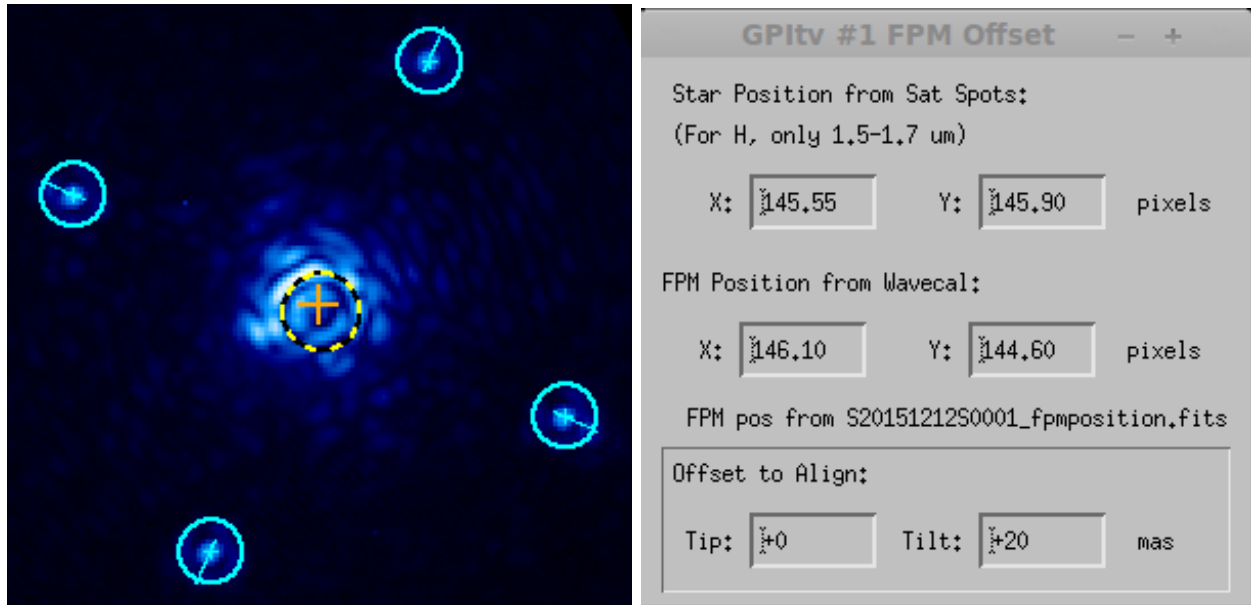


Figure 6.3 An example image viewed using the GPI-tv, showing the misalignment of the star and the FPM. Left: The FPM position is marked by a yellow-black dash circle. The satellite spots are circled by green solid circles. The star position, determined by the position of the satellite spots, is marked by a cross sign. The star and the FPM in this example image is clearly misaligned. Right: In the little pop-out window, it displays the suggested change in tip and tilt offset for aligning the star to the FPM.

## BIBLIOGRAPHY

- Allard, F., Homeier, D., & Freytag, B. 2012, Royal Society of London Philosophical Transactions Series A, 370, 2765
- Backman, D. E., & Paresce, F. 1993, in Protostars and Planets III, ed. E. H. Levy & J. I. Lunine, 1253–1304
- Baraffe, I., Chabrier, G., Barman, T. S., Allard, F., & Hauschildt, P. H. 2003, A&A, 402, 701
- Bohren, C. F., & Huffman, D. R. 1983, Absorption and scattering of light by small particles
- Booth, M., Kennedy, G., Sibthorpe, B., et al. 2013, MNRAS, 428, 1263
- Boss, A. P. 1997, Science, 276, 1836
- Cardelli, J. A., Clayton, G. C., & Mathis, J. S. 1989a, ApJ, 345, 245
- . 1989b, ApJ, 345, 245
- Chabrier, G., Baraffe, I., Allard, F., & Hauschildt, P. 2000, ApJ, 542, 464
- Chauvin, G., Lagrange, A.-M., Dumas, C., et al. 2004, A&A, 425, L29
- Chen, C. H., Mittal, T., Kuchner, M., et al. 2014, ApJS, 211, 25
- Chen, C. H., Pecaute, M., Mamajek, E. E., Su, K. Y. L., & Bitner, M. 2012a, ApJ, 756, 133
- . 2012b, ApJ, 756, 133
- Churcher, L. J., Wyatt, M. C., Duchêne, G., et al. 2011, MNRAS, 417, 1715
- Cohen, M., Walker, R. G., Carter, B., et al. 1999, AJ, 117, 1864
- Crepp, J. R., Johnson, J. A., Howard, A. W., et al. 2014, ApJ, 781, 29
- Currie, T., Lisse, C. M., Kuchner, M., et al. 2015, ApJ, 807, L7

- Currie, T., Burrows, A., Madhusudhan, N., et al. 2013, *ApJ*, 776, 15
- Cutri, R. M., & et al. 2012, *VizieR Online Data Catalog*, 2311, 0
- Cutri, R. M., Skrutskie, M. F., van Dyk, S., et al. 2003a, *VizieR Online Data Catalog*, 2246, 0
- . 2003b, *VizieR Online Data Catalog*, 2246, 0
- De Rosa, R. J., Patience, J., Wilson, P. A., et al. 2014, *MNRAS*, 437, 1216
- de Zeeuw, P. T., Hoogerwerf, R., de Bruijne, J. H. J., Brown, A. G. A., & Blaauw, A. 1999, *AJ*, 117, 354
- Dent, W. R. F., Wyatt, M. C., Roberge, A., et al. 2014, *Science*, 343, 1490
- Dohnanyi, J. S. 1969, *J. Geophys. Res.*, 74, 2531
- Draine, B. T., & Lee, H. M. 1984a, *ApJ*, 285, 89
- . 1984b, *ApJ*, 285, 89
- Draine, B. T., & Li, A. 2001, *ApJ*, 551, 807
- Draper, Z. H., Marois, C., Wolff, S., et al. 2014, in *Society of Photo-Optical Instrumentation Engineers (SPIE) Conference Series*, Vol. 9147, *Society of Photo-Optical Instrumentation Engineers (SPIE) Conference Series*, 4
- Edgar, R., & Artymowicz, P. 2004, *MNRAS*, 354, 769
- Foreman-Mackey, D., Hogg, D. W., Lang, D., & Goodman, J. 2013a, *PASP*, 125, 306
- . 2013b, *PASP*, 125, 306
- Goodman, J., & Weare, J. 2010a, *Comm. App. Math. Comp. Sci*, 5, 65
- . 2010b, *Comm. App. Math. Comp. Sci*, 5, 65
- Haisch, Jr., K. E., Lada, E. A., & Lada, C. J. 2001, *ApJ*, 553, L153

- Harper, D. A., Loewenstein, R. F., & Davidson, J. A. 1984, *ApJ*, 285, 808
- Hinkley, S., Oppenheimer, B. R., Soummer, R., et al. 2009, *ApJ*, 701, 804
- Høg, E., Fabricius, C., Makarov, V. V., et al. 2000, *A&A*, 355, L27
- Houk, N. 1982, Michigan Catalogue of Two-dimensional Spectral Types for the HD stars. Volume 3. Declinations -40.0 to -26.0.
- Hung, L.-W., Fitzgerald, M. P., Chen, C. H., et al. 2015a, *ApJ*, 802, 138
- Hung, L.-W., Duchêne, G., Arriaga, P., et al. 2015b, *ApJ*, 815, L14
- Hung, L.-W., Bruzzone, S., Millar-Blanchaer, M. A., et al. 2016, in Society of Photo-Optical Instrumentation Engineers (SPIE) Conference Series, Society of Photo-Optical Instrumentation Engineers (SPIE) Conference Series, in prep
- Ingraham, P., Perrin, M. D., Sadakuni, N., et al. 2014, in Society of Photo-Optical Instrumentation Engineers (SPIE) Conference Series, Vol. 9147, Society of Photo-Optical Instrumentation Engineers (SPIE) Conference Series, 7
- Jensen-Clem, R., Millar-Blanchaer, M., Mawet, D., et al. 2016, *ApJ*, 820, 111
- Kalas, P. G., Rajan, A., Wang, J. J., et al. 2015, *ApJ*, 814, 32
- Kasper, M., Apai, D., Wagner, K., & Robberto, M. 2015, *ApJ*, 812, L33
- Kastner, J. H., Hily-Blant, P., Sacco, G. G., Forveille, T., & Zuckerman, B. 2010, *ApJ*, 723, L248
- Kennedy, G. M., & Wyatt, M. C. 2014, ArXiv e-prints, arXiv:1408.4116
- Kenyon, S. J., & Bromley, B. C. 2005, *AJ*, 130, 269
- Kirchschlager, F., & Wolf, S. 2013, *A&A*, 552, A54

- Konopacky, Q. M., Thomas, S. J., Macintosh, B. A., et al. 2014, in Society of Photo-Optical Instrumentation Engineers (SPIE) Conference Series, Vol. 9147, Society of Photo-Optical Instrumentation Engineers (SPIE) Conference Series, 84
- Kóspál, Á., Moór, A., Juhász, A., et al. 2013, *ApJ*, 776, 77
- Krisciunas, K., Sinton, W., Tholen, K., et al. 1987, *PASP*, 99, 887
- Kurucz, R. 1993a, ATLAS9 Stellar Atmosphere Programs and 2 km/s grid. Kurucz CD-ROM No. 13. Cambridge, Mass.: Smithsonian Astrophysical Observatory, 1993., 13
- . 1993b, ATLAS9 Stellar Atmosphere Programs and 2 km/s grid. Kurucz CD-ROM No. 13. Cambridge, Mass.: Smithsonian Astrophysical Observatory, 1993., 13
- Laor, A., & Draine, B. T. 1993, *ApJ*, 402, 441
- Li, A., & Greenberg, J. M. 1997, *A&A*, 323, 566
- Liu, Q., Wang, T., & Jiang, P. 2014, *AJ*, 148, 3
- Lu, J. R., Ghez, A. M., Yelda, S., et al. 2010, in Proc. SPIE, Vol. 7736, Adaptive Optics Systems II, 77361I
- Lyra, W., & Kuchner, M. J. 2012, ArXiv e-prints, arXiv:1204.6322
- Macintosh, B., Graham, J. R., Ingraham, P., et al. 2014, Proceedings of the National Academy of Science, 111, 12661
- Macintosh, B., Graham, J. R., Barman, T., et al. 2015, *Science*, 350, 64
- Macintosh, B. A., Graham, J. R., Palmer, D. W., et al. 2008, in Society of Photo-Optical Instrumentation Engineers (SPIE) Conference Series, Vol. 7015, Society of Photo-Optical Instrumentation Engineers (SPIE) Conference Series
- Maire, J., Ingraham, P. J., De Rosa, R. J., et al. 2014, in Society of Photo-Optical Instrumentation Engineers (SPIE) Conference Series, Vol. 9147, Society of Photo-Optical Instrumentation Engineers (SPIE) Conference Series, 85

- Mamajek, E. E., Meyer, M. R., & Liebert, J. 2002a, *AJ*, 124, 1670
- . 2002b, *AJ*, 124, 1670
- Marcy, G. W., Cochran, W. D., & Mayor, M. 2000, *Protostars and Planets IV*, 1285
- Marois, C., Correia, C., Galicher, R., et al. 2014, in *Society of Photo-Optical Instrumentation Engineers (SPIE) Conference Series*, Vol. 9148, Society of Photo-Optical Instrumentation Engineers (SPIE) Conference Series, 0
- Marois, C., Lafrenière, D., Doyon, R., Macintosh, B., & Nadeau, D. 2006, *ApJ*, 641, 556
- Marois, C., Macintosh, B., Barman, T., et al. 2008, *Science*, 322, 1348
- Marois, C., Zuckerman, B., Konopacky, Q. M., Macintosh, B., & Barman, T. 2010, *Nature*, 468, 1080
- Mathews, G. S., Pinte, C., Duchêne, G., Williams, J. P., & Ménard, F. 2013, *A&A*, 558, A66
- Millar-Blanchaer, M., Perrin, M. D., Bruzzone, S., et al. 2016, in *Society of Photo-Optical Instrumentation Engineers (SPIE) Conference Series*, Society of Photo-Optical Instrumentation Engineers (SPIE) Conference Series
- Millar-Blanchaer, M. A., Graham, J. R., Pueyo, L., et al. 2015, *ApJ*, 811, 18
- Moór, A., Ábrahám, P., Derekas, A., et al. 2006a, *ApJ*, 644, 525
- . 2006b, *ApJ*, 644, 525
- Moór, A., Ábrahám, P., Juhász, A., et al. 2011, *ApJ*, 740, L7
- Moór, A., Kóspál, Á., Ábrahám, P., et al. 2013, in *Protostars and Planets VI Posters*, 67
- Moór, A., Henning, T., Juhász, A., et al. 2015, *ApJ*, 814, 42
- Morzinski, K. M., Males, J. R., Skemer, A. J., et al. 2015, *ApJ*, 815, 108

- Nilsson, R., Liseau, R., Brandeker, A., et al. 2010, *A&A*, 518, A40
- Pecaut, M. J., Mamajek, E. E., & Bubar, E. J. 2012a, *ApJ*, 746, 154
- . 2012b, *ApJ*, 746, 154
- Perrin, M. D., Maire, J., Ingraham, P., et al. 2014a, in *Society of Photo-Optical Instrumentation Engineers (SPIE) Conference Series*, Vol. 9147, Society of Photo-Optical Instrumentation Engineers (SPIE) Conference Series, 3
- Perrin, M. D., Duchene, G., Millar-Blanchaer, M., et al. 2014b, *ArXiv e-prints*, arXiv:1407.2495
- . 2015, *ApJ*, 799, 182
- Perrin, M. D., Ingraham, P., Maire, J., et al. 2016, in *Society of Photo-Optical Instrumentation Engineers (SPIE) Conference Series*, Society of Photo-Optical Instrumentation Engineers (SPIE) Conference Series
- Pinte, C., Harries, T. J., Min, M., et al. 2009, *A&A*, 498, 967
- Pinte, C., Ménard, F., Duchêne, G., & Bastien, P. 2006, *A&A*, 459, 797
- Poyneer, L. A., De Rosa, R. J., Macintosh, B., et al. 2014, in *Proc. SPIE*, Vol. 9148, Adaptive Optics Systems IV, 91480K
- Pueyo, L., Soummer, R., Hoffmann, J., et al. 2015, *ApJ*, 803, 31
- Rieke, G. H., Young, E. T., Engelbracht, C. W., et al. 2004, *ApJS*, 154, 25
- Rizzuto, A. C., Ireland, M. J., & Robertson, J. G. 2011a, *MNRAS*, 416, 3108
- . 2011b, *MNRAS*, 416, 3108
- Schmid, H. M., Joos, F., & Tschan, D. 2006, *A&A*, 452, 657
- Sivaramakrishnan, A., & Oppenheimer, B. R. 2006, *ApJ*, 647, 620

- Sivaramakrishnan, A., Soummer, R., Carr, G. L., et al. 2009, in Proc. SPIE, Vol. 7440, Techniques and Instrumentation for Detection of Exoplanets IV, 74401C
- Sivaramakrishnan, A., Soummer, R., Oppenheimer, B. R., et al. 2010, in Society of Photo-Optical Instrumentation Engineers (SPIE) Conference Series, Vol. 7735, Society of Photo-Optical Instrumentation Engineers (SPIE) Conference Series, 86
- Soummer, R., Pueyo, L., & Larkin, J. 2012, ApJ, 755, L28
- Telesco, C. M., Fisher, R. S., Piña, R. K., et al. 2000, ApJ, 530, 329
- Thalmann, C., Janson, M., Buenzli, E., et al. 2013, ApJ, 763, L29
- Torres, C. A. O., Quast, G. R., Melo, C. H. F., & Sterzik, M. F. 2008, Young Nearby Loose Associations, ed. B. Reipurth, 757
- van Leeuwen, F. 2007a, A&A, 474, 653
- . 2007b, A&A, 474, 653
- Wang, J. J., Ruffio, J.-B., De Rosa, R. J., et al. 2015, pyKLIP: PSF Subtraction for Exoplanets and Disks, Astrophysics Source Code Library, ascl:1506.001
- Wang, J. J., Rajan, A., Graham, J. R., et al. 2014, in Society of Photo-Optical Instrumentation Engineers (SPIE) Conference Series, Vol. 9147, Society of Photo-Optical Instrumentation Engineers (SPIE) Conference Series, 55
- Warren, S. G. 1984, Applied Optics, 23, 1206
- Wiktorowicz, S. J., Millar-Blanchaer, M., Perrin, M. D., et al. 2014, in Society of Photo-Optical Instrumentation Engineers (SPIE) Conference Series, Vol. 9147, Society of Photo-Optical Instrumentation Engineers (SPIE) Conference Series, 83
- Wolff, S. G., Perrin, M. D., Maire, J., et al. 2014, in Society of Photo-Optical Instrumentation Engineers (SPIE) Conference Series, Vol. 9147, Society of Photo-Optical Instrumentation Engineers (SPIE) Conference Series, 7

- Wright, E. L., Eisenhardt, P. R. M., Mainzer, A. K., et al. 2010, *AJ*, 140, 1868
- Wyatt, M. C. 2006, *ApJ*, 639, 1153
- . 2008, *ARA&A*, 46, 339
- Wyatt, M. C., Clarke, C. J., & Booth, M. 2011, *Celestial Mechanics and Dynamical Astronomy*, 111, 1
- Wyatt, M. C., Dermott, S. F., Telesco, C. M., et al. 1999, *ApJ*, 527, 918
- Yamamura, I., Makiuti, S., Ikeda, N., et al. 2010, *VizieR Online Data Catalog*, 2298, 0
- Zuckerman, B., Forveille, T., & Kastner, J. H. 1995, *Nature*, 373, 494
- Zuckerman, B., & Song, I. 2012, *ApJ*, 758, 77
- Zurlo, A., Vigan, A., Hagelberg, J., et al. 2013, *A&A*, 554, A21